

# Relativistic Hydrodynamics under Rotation: Prospects and Limitations from a Holographic Perspective

Markus A. G. Amano<sup>a,b</sup>, Casey Cartwright<sup>c</sup>, Matthias Kaminski<sup>d</sup>, Jackson Wu<sup>d</sup>

<sup>a</sup>*Institute of Contemporary Mathematics, School of Mathematics and Statistics, Henan University, Kaifeng, 475004, Henan, P. R. China*

<sup>b</sup>*Department of Physics, Yamagata University, Kojirakawa-machi 1-4-12, Yamagata 990-8560, Yamagata, Japan*

<sup>c</sup>*Institute for Theoretical Physics, Utrecht University, Princetonplein 5, Utrecht, 3584 CC, Netherlands*

<sup>d</sup>*Department of Physics and Astronomy, University of Alabama, 514 University Boulevard, Tuscaloosa, 35487, AL, USA*

---

## Abstract

The AdS/CFT correspondence, or holography, has provided numerous important insights into the behavior of strongly-coupled many-body systems. Crucially, it has provided a testing ground for the construction of new effective field theories, especially those in the low frequency, long wavelength limit known as hydrodynamics. We review the study of strongly-coupled rotating fluids using holography, and we examine the hydrodynamics emerging from the study of rotating Myers-Perry black holes. We discuss three regimes in which holographic rotating fluids display either (1) hydrodynamic behavior of a boosted fluid, (2) hydrodynamic behavior distinct from a boosted fluid, or (3) no obvious hydrodynamic behavior. We describe techniques to obtain hydrodynamic and non-hydrodynamic modes, and we compute the radius of convergence for the hydrodynamic regimes. The limitations of hydrodynamics under rotation are discussed alongside our findings.

*Keywords:* AdS/CFT, Holography, Hydrodynamics, Strongly-coupled field theory

---

## Contents

<b>1</b>	<b>Introduction</b>	<b>3</b>
1.1	Roadmap of this review . . . . .	4
1.2	Preview of a key result . . . . .	6
<b>2</b>	<b>Rotation in heavy-ion collisions, hydrodynamics, and holography</b>	<b>6</b>
2.1	Rotation in heavy-ion collisions . . . . .	7
2.2	Rotation in hydrodynamics . . . . .	7
2.3	Rotation in holography . . . . .	8

---

\*This research was supported in part by the U.S. Department of Energy under Grant No. DE-SC0012447 and by the National Science Foundation under Grant No. NSF PHY-1748958. C.C. was supported in part, by the Netherlands Organisation for Scientific Research (NWO) under the VICI grant VI.C.202.104. M.K. thanks the Kavli Institute for Theoretical Physics, Santa Barbara for hospitality while part of this work was completed. M.A. was supported by Henan University's Postdoctoral Program in the creation of this work.

*Email addresses:* markus.a.amano@gmail.com (Markus A. G. Amano), c.c.cartwright@uu.nl (Casey Cartwright), mski@ua.edu (Matthias Kaminski), jmwu@ua.edu (Jackson Wu)

2.3.1	Lower-dimensional black holes . . . . .	8
2.3.2	Five-dimensional black holes . . . . .	10
<b>3</b>	<b>The five-dimensional holographic setup</b>	<b>10</b>
3.1	Rotating background metric and black hole thermodynamics . . . . .	11
3.2	Linearized metric fluctuation equations and separability . . . . .	14
3.2.1	Equal angular momenta Myers Perry black hole . . . . .	14
3.2.2	Symmetries and separable field equations . . . . .	17
3.2.3	General ansatz for spin-2 fields . . . . .	19
3.3	Rigidly rotating fluids and large Myers-Perry black holes . . . . .	20
3.3.1	Vacuum expectation value of the energy-momentum tensor . . . . .	20
3.3.2	Ashtekar-Magnon charges, the conformal fluid, and the large black hole limit . . . . .	23
3.3.3	Stereographic projection and the flat spacetime fluid velocity . . . . .	25
<b>4</b>	<b>Hydrodynamic and non-hydrodynamic modes of rotating plasma from quasinormal modes</b>	<b>30</b>
4.1	Basic facts about quasinormal modes . . . . .	30
4.2	Quasinormal modes dual to hydrodynamic and non-hydrodynamic modes	32
4.2.1	Previous quasinormal mode results for large black holes . . . . .	33
4.2.2	$\mathcal{K} = \mathcal{J} - \text{Tensor}$ fluctuations . . . . .	38
4.2.3	$\mathcal{K} = \mathcal{J} - 1 - \text{Vector}$ fluctuations . . . . .	40
4.2.4	$\mathcal{K} = \mathcal{J} - 2 - \text{Scalar}$ fluctuations . . . . .	40
4.2.5	Cross sector spectrum comparison . . . . .	42
4.2.6	Horizon radius dependence & the emergence of hydrodynamics . . . . .	42
4.2.7	Perturbative instabilities: superradiant and Gregory-Laflamme . . . . .	47
4.3	Critical points . . . . .	48
4.3.1	Implicit functions and their series expansions . . . . .	48
4.3.2	Determination of the critical point . . . . .	51
4.4	Pole-Skipping . . . . .	53
4.4.1	Gravitational shockwaves . . . . .	54
4.4.2	Near horizon metric fluctuations . . . . .	58
<b>5</b>	<b>Summaries, discussion, and outlook</b>	<b>63</b>
5.1	Summary of previously published results . . . . .	63
5.2	Summary of new results first presented in this review . . . . .	66
5.3	Discussion and implications . . . . .	68
5.4	Outlook . . . . .	69
<b>Appendix A</b>	<b>Energy-Momentum tensor</b>	<b>71</b>
<b>Appendix B</b>	<b>Quasinormal mode data</b>	<b>72</b>
Appendix B.1	Tensor sector . . . . .	72
Appendix B.2	Vector sector . . . . .	73
Appendix B.3	Scalar sector . . . . .	74
<b>Appendix C</b>	<b>Numerical methods</b>	<b>75</b>

<b>Appendix D</b>	<b>Null coordinates</b>	<b>76</b>
Appendix D.1	Infalling Eddington-Finkelstein coordinates . . . . .	76
Appendix D.2	Kruskal coordinates . . . . .	77
<b>Appendix E</b>	<b>Hydrodynamic dispersion relations and conventions</b>	<b>78</b>
<b>Appendix F</b>	<b>Limits of the Wigner D function</b>	<b>79</b>

## 1. Introduction

From eddies in rivers to rotating binary systems of merging black holes (BHs) or neutron stars, rotating fluids are found everywhere, with a vast variety in a huge range of scales. Having a universal and effective description of rotating systems (in an appropriate regime) that is independent of their microscopic details is thus of high interest, and hydrodynamics provides just such a universal effective description when discussing excitations around an equilibrium state at low energy and long wavelength.

Hydrodynamics has found important applications in describing relativistic fluids, providing guidance in creating, probing, simulating and analyzing such fluids. A prime example is the Quark-Gluon-Plasma (QGP) produced in the relativistic heavy-ion collisions at RHIC. The QGP has the characteristics of a strongly interacting quantum fluid, and it exhibits hydrodynamic behavior. It could also possess large vorticity, as the STAR measurement of the hyperon polarization in 2017 indicates [1]. This garnered much attention, and much effort has been focused on how to properly incorporate vorticity and (spin) angular momentum into relativistic hydrodynamics [2, 3, 4, 5, 6, 7, 8, 9, 10, 11, 12, 13, 14, 15, 16].

As the QGP is a strongly interacting system, understanding its nature theoretically in terms of a strongly-coupled quantum field theory is difficult, as few tools are available for finding analytical solutions to the governing dynamical equations. This difficulty is overcome in the Anti-de Sitter/Conformal Field Theory (AdS/CFT) correspondence, or *holography*, by translating the problem into a geometrical one in an appropriate higher-dimensional gravity dual (having one more spatial dimension than the CFT) for which there is computational tractability. In this way, holography has been able to offer fresh perspectives and valuable insights on strongly interacting quantum matter that cannot be obtained otherwise.

Rotating BHs have long been investigated in the context of gravity [17, 18]. This laid the foundation to construct holographic duals of strongly interacting rotating fluids, and to study their properties and dynamics using rotating BHs [19, 20, 21, 22, 23, 24, 25, 26, 27, 28, 29, 30, 31, 32, 33]. Rotation introduces nontrivial inertial effects into the dispersion relations of rotational eigenmodes (with respect to an inertial observer in the rest frame) compared to non-rotational ones. For fluids, these eigenmodes are typically hard to calculate using field theoretic methods. However, the same problem when mapped to the gravity side is a straightforward computation of *quasinormal modes* (QNMs), making it much easier to study how the eigenmodes behave and change under rotation using holography. In this way, holography can be applied, on the one hand, as a discovery tool to reveal unknown transport effects [34], and on the other, to test the validity of hydrodynamic descriptions [35]. In addition, holography can be used to construct novel solutions to hydrodynamics, such as an analytical vortical fluid flow [36] that plays a central role in this review.

In this article, we review recent results obtained on rotating holographic fluids. We also report findings newly obtained for this review by us. The holographic, dual gravity

systems we focus on are the large, five-dimensional AdS Myers-Perry (MP) BHs with two equal angular momenta <sup>1</sup>. These are solutions to type IIB supergravity, and they are dual to rotating fluids in the  $\mathcal{N} = 4$  supersymmetric Yang-Mills (SYM) theory, a strongly-coupled CFT. Below, we give a roadmap of the topics and results that we focus on in this review.

### 1.1. Roadmap of this review

When viewed as an expansion in gradients of hydrodynamic quantities (temperature, fluid velocities), what limits the power and applicability of hydrodynamics is the radius of convergence of this series expansion. While it is not possible in general to determine the radius of convergence of a hydrodynamic gradient expansion for every microscopic theory (particularly when it is strongly-coupled), it is possible for the SYM theory. Thanks to the AdS/CFT correspondence, the spectrum of QNMs characterizing perturbations of asymptotically AdS BHs is equivalent to that of the poles of retarded Green's functions in the dual CFT (SYM) [38], and this makes computing the radius of convergence of SYM hydrodynamics feasible through the dual AdS gravity [39, 40, 41].

Besides shedding light on the reliability of the hydrodynamic gradient expansion, the connection between the QNM spectrum, BH horizon dynamics, and Green's functions in the dual field theory has led to a wealth of striking discoveries. One surprising revelation is the connection between late time hydrodynamic evolution of conserved quantities and early time chaotic dynamics. First explored in [42], this relationship links the out-of-time-order-correlators (OTOCs) used to characterize chaos in quantum many-body systems <sup>2</sup> and the hydrodynamics of energy-energy correlations [48, 49]. Particularly interesting is the demonstration that the Lyapunov exponent and butterfly velocity—both measures of operator growth—associated with quantum chaos in the SYM theory are robustly related to the locations of a family of *pole-skipping points* in the energy response, which are captured by additional infalling solutions of the linearized Einstein equations near the event horizon [48, 49].

Novel ideas have sprung from the exploration of this remarkable correspondence between BH QNMs and the poles of retarded Green's functions in the dual CFT, and many of these facilitate a better understanding of strongly interacting rotating fluids. With the advances in the understanding of the MP BH geometry [23, 24, 25] and its dual fluid description [50, 36], the research community was able to pursue and implement these ideas which would have been very difficult (or even impossible) otherwise [29, 32, 33]. This article is dedicated to reviewing the recent progress in the highly interconnected study of strongly-coupled rotating plasma. We shall bring together results scattered throughout the literature, we shall discuss them in a unified context under the framework of holography, and we shall report findings obtained by us in the study of MP BHs that are completely new.

After a quick overview in Sec. 2 of the importance of rotation in heavy-ion collision experiments and modelling (hydrodynamics and holography), we discuss in detail in Sec. 3 the holographic framework used for studying strongly-coupled rotating plasma like the

---

<sup>1</sup>In  $D$  spatial dimensions, there are generically  $\lceil (D-1)/2 \rceil$  independent planes of rotation and thus a corresponding number of angular momenta [37]. For five-dimensional MP BHs,  $D = 4$ , and there are two angular momenta.

<sup>2</sup>The OTOCs are calculated using holography [43, 44] by considering gravitational shockwave collisions [45, 46, 47] in the bulk of the dual gravity.

QGP. We go into detail about the geometry of the MP BH (Secs. 3.1 and 3.2.1), we exhibit the separability of the associated linearized Einstein equations (Sec. 3.2.2), which, as we shall see, confers great computational power, and we clarify the general ansatz for metric fluctuations (spin-2 fields) used in the past (Sec. 3.2.3). We close the section with a discussion on the holographic interpretation of the MP BH geometry and the fluid behavior of the dual CFT (Sec. 3.3). In particular, we discuss how to obtain the vacuum expectation value of the energy-momentum tensor (Sec. 3.3.1), the relation between two methods to compute conserved charges of the asymptotic geometry (Sec. 3.3.2), and a sequence of coordinate transformations used to stereographically project the energy-momentum tensor obtained in Sec. 3.3.1 to flat spacetime (Sec. 3.3.3).

Equipped with these technical tools, we turn to discuss the results in Sec. 4. There are three major themes: QNMs displaying hydrodynamic and non-hydrodynamic behavior, critical points providing the convergence radius of the hydrodynamic expansion, and the pole-skipping phenomenon yielding information about the dynamics of many-body quantum chaos in rotating fluids. After a short introduction explaining what are the QNMs and their key features (Sec. 4.1), we begin by reviewing the hydrodynamic QNMs obtained in [29] (Sec. 4.2.1). We then report results we obtained on non-hydrodynamic modes from our study of the QNMs. We characterize these by their angular momentum quantum numbers, and we organize them into three sectors, the *tensor fluctuations* (Sec. 4.2.2), *vector fluctuations* (Sec. 4.2.3), and *scalar fluctuations* (Sec. 4.2.4). A combined view of all three sectors is given by a cross spectrum comparison (Sec. 4.2.5). We discuss the dependence on the horizon radius in our results, which provides a unique way to determine when a transition into the hydrodynamic regime has occurred in the dual fluids (Sec. 4.2.6). We discuss also how the QNMs can indicate BH instability. In the large BH limit given by Eqs. (112) and (113), the MP BH is perturbatively stable against all metric fluctuations [29]. But near extremality, they become unstable. This is the so-called superradiant instability previously documented in [24, 26, 51, 52]. We look into this instability for horizon radii on the order of the AdS radius (Sec. 4.2.7), and we demonstrate that the BH becomes unstable for small values of the angular quantum number of the fluctuation.

Having examined closely both previous and new results concerning the spectrum of QNMs of the MP BH, we focus next on a set of special QNMs, the so-called *critical points*, which determines the radius of convergence of the hydrodynamic expansion in the dual field theory [32] (Sec. 4.3). We review first the progress made in [39, 40, 41] concerning the interpretation of dispersion relations in terms of complex implicit functions and local series expansions of these functions (Sec. 4.3.1). We then discuss how to locate the critical points in the complex frequency plane as the dual fluid rotates (Sec. 4.3.2). This bears crucial consequences for the hydrodynamic description as it would break down if the critical points failed to remain at a finite distance from the origin in the complex plane.

Lastly, we turn our attention to another set of special QNMs, the so-called *pole skipping points*, which indicate the existence of additional infalling solutions to the linearized Einstein equations at the event horizon [33] (Sec. 4.4). Pole skipping points may signal a hydrodynamic origin for many-body quantum chaos, and we discuss how they can be obtained from a simple analytic expression of the OTOC when derived for operator configurations on interlocking Hopf circles (Sec. 4.4.1). In the large BH limit these expressions yield the Lyapunov exponent and butterfly velocity of the SYM rotating state dual to the MP BH. Furthermore, we demonstrate that the dispersion relations obtained from QNMs in this limit pass through exactly the pole-skipping points (Sec. 4.4.2).

We conclude in Sec. 5 with a summary of all the results, both old (Sec. 5.1) and new (Sec. 5.2), and a discussion of the implications of our results (Sec. 5.3). We end with an outlook on the still many open problems and interesting avenues left unexplored in this work (Sec. 5.4).

In the appendices we provide supplementary details on the expressions derived, the QNMs computed, and the methods employed. Appendix A contains the full form of the energy-momentum tensor of the MP BH in general. Appendix B contains the data of the six lowest QNMs in all three sectors of fluctuations for some reference values of rotational parameters. Appendix C contains technical details on the numerical methods used to compute QNMs. Appendix D contains details on the coordinate transformation to null coordinates, including both Eddington-Finkelstein coordinates and Kruskal coordinates. Appendix E contains conventions for dispersion relations and expected values of transport coefficients and power law scaling. Appendix F contains details about the Wigner D functions essential to our decomposition of metric fluctuations and their behavior in the large BH limit.

Key results are summarized and highlighted in boxed paragraphs at the end of several sections throughout this review.

### 1.2. Preview of a key result

A key result of our analysis here that we would like to emphasize from the outset is the following:

Even though in the large BH limit hydrodynamic fluctuations at large temperatures *perceive* the rotating holographic fluid (dual to the MP BH) as if it was a boosted fluid, the rotating holographic fluid is not a boosted fluid.

Indeed, if one probes the background metric of a large rotating BH with only metric fluctuations having *small frequency and momentum compared to the horizon radius*, then these fluctuations *effectively see* a boosted black brane metric.<sup>3</sup> This can be explicitly seen from the equations of motion obeyed by the metric fluctuations around the rotating BH background metric, as we explain in Sec. 4. But, as we emphasize above, this should not be taken to indicate that the hydrodynamic description of the rotating holographic fluid studied here is trivial. In this article, we analyze to what degree the hydrodynamic behavior of the holographic fluid persists to lower temperatures and, in particular, away from the large BH limit that was the focus of [29]. We show that although the behavior is hydrodynamic, transport coefficients deviate significantly from those of a boosted fluid, see Sec. 4.2.6.

## 2. Rotation in heavy-ion collisions, hydrodynamics, and holography

In this section, we first outline how vorticity has become important in heavy-ion collisions. We then briefly discuss how rotation is incorporated in hydrodynamics. Lastly, we review how the description of rotation developed in the context of holography.

---

<sup>3</sup>We stress, however, that the background metric itself is not that of a boosted black brane.

### 2.1. Rotation in heavy-ion collisions

The observation of *global hyperon polarization* in heavy-ion collisions at RHIC by the STAR collaboration [1, 53] brought rotation and vorticity into the sharp focus in heavy-ion research. In such non-central collisions between gold ions, the global angular momentum axis and the spin axis of individual emitted  $\Lambda$  (and  $\bar{\Lambda}$ ) hyperons are found to be aligned [1]. This indicates that the hyperons were aligned with the orbital angular momentum of the colliding nuclei through the coupling between spin and orbital angular momentum (spin-orbit coupling). This bears important implications for the fluid generated in these collisions [54, 55, 56, 57, 58], and the fluid is inferred to be highly vortical [2, 3, 10]. The global hyperon polarization appears to decrease with collision energy, as indicated by the RHIC data at  $\sqrt{s_{NN}} = 7.7 - 200$  GeV [59, 1]; it also increases in more peripheral collisions, and depends weakly on the hyperon's transverse momentum and pseudorapidity [59]. This energy dependence is confirmed at the higher energies of  $\sqrt{s_{NN}} = 2.76$  and 5.02 TeV at the LHC, where the global hyperon polarization is found to be consistent with zero [60].

There is another polarization observable, namely the *(local) longitudinal hyperon polarization*, which is the polarization of hyperons in the longitudinal direction (i.e. along the beam line), and it was first observed at  $\sqrt{s_{NN}} = 200$  GeV at RHIC [61]. The vorticity and the corresponding polarization exhibits a quadrupole structure in the transverse plane. This nonzero longitudinal polarization was later measured at higher energies in Pb-Pb collisions at the LHC by the ALICE Collaboration [60, 62], though the amplitude of the polarization is smaller than for Au-Au collisions at the lower RHIC energies.

Intuitively, a global vorticity (or rotation) that leads to a global polarization can come from having two ions, each carrying linear momentum, colliding at a nonzero impact parameter; the resulting nonzero angular momentum is then carried by the system along an axis through its center of mass. In this case, one can consider a globally rotating, thermodynamic equilibrium state around which collective thermodynamic excitations can be studied. Local longitudinal polarization and local vorticity are conceptually less intuitive. Having local vorticity implies that each fluid element carries information encoding the non-trivial vorticity at its own location. Because of the spin-orbit coupling, this then implies that each fluid element should also carry non-trivial information about the spin degrees of freedom at the location of the fluid cell. The possible presence of strong local and global vorticities in heavy-ion collisions thus provided a strong impetus to develop a proper fluid dynamic descriptions of rotating fluids interacting with particles carrying spin [4, 5, 6, 7, 8, 9, 11, 12, 63, 13, 14, 15, 16].

### 2.2. Rotation in hydrodynamics

Vorticity, rotation, and shear flow are interrelated in fluids, and they are all encoded in the fluid velocity. One way to sort out these rotational phenomena systematically is to consider the conserved angular momentum. One type of the angular momentum, which is implicit in the standard formulation of hydrodynamics [64], is the orbital angular momentum encoded in the energy-momentum tensor,  $T^{\mu\nu}$ ; the other is the spin angular momentum encoded by the spin current,  $S^{\mu\nu\rho}$ . In the presence of spin-orbit coupling, only the sum of both spin and orbital currents,  $J^{\mu\nu\rho}$ , is a Noether current associated with the conservation of the total angular momentum:

$$J^{\mu\nu\rho} = x^\nu T^{\mu\rho} - x^\rho T^{\mu\nu} - S^{\mu\nu\rho}, \quad (1)$$

where  $x^\mu$  is the spacetime coordinate. In the limit of negligible spin-orbit coupling, the spin angular momentum can be treated as a locally conserved  $U(1)$ -charge associated

with a chemical potential, similar to an electric or baryon charge. While convenient, this is however not possible in general. The interaction of spin-carrying particles with fluids had not been considered in depth in the standard formulations of relativistic hydrodynamics. It is only recently that significant effort has been put into establishing a proper fluid dynamic description of relativistic rotating fluids interacting with particles carrying spin [4, 5, 6, 7, 8, 9, 11, 12, 63, 13, 14, 15, 16].

A particularly simple case arises when we consider an element of a rigidly rotating fluid in three spatial dimensions. Suppose the fluid element is located at  $\vec{r}$  that is  $R$  away from the axis of rotation, has an angular velocity  $\vec{\omega}$ , and in the rotating frame has a velocity  $\vec{v}$ . At non-relativistic velocities, we expect from Newtonian mechanics inertial effects (fictitious forces) because the rest frame of this fluid element is an accelerated, non-inertial reference frame. There are in general three possible non-inertial forces: the centrifugal force  $F_{Cen} = -\vec{\omega} \times (\vec{\omega} \times \vec{r})$ , the Coriolis force  $F_{Cor} = -2\vec{\omega} \times \vec{v}$ , and the Euler force  $F_{Euler} = -\dot{\vec{\omega}} \times \vec{r}$ . Suppose the angular velocity is constant and that the fluid element is stationary in the rotating frame, then neither the Euler nor the Coriolis force contribute, and we are left with just the centrifugal force whose magnitude is given by  $|F_{Cen}| = \omega^2 R = v_{\perp}^2/R$ . Then for  $R$  large enough, if the tangential velocity  $v_{\perp}$  is held fixed ( $\omega = v_{\perp}/R$  is then small) the magnitude of the inertial effect can be made small ( $|F_{Cen}| \ll 1$ ) and thus neglected. The fluid element is then indistinguishable from a boosted fluid element if  $R$  ( $\omega$ ) is large (small) enough, and the hydrodynamic description of boosted fluids recently developed in [65] and [66] comes into play. Note that such boosted fluid description is in general valid only in a certain “large radius” limit (large  $R$  above). In this review, we shall consider mostly rotating fluids away from this limit, and we shall see that there are corrections to the boosted fluid behavior suppressed at large temperatures (large BH horizon radius).

### 2.3. Rotation in holography

In holography, angular momentum (and thus rotation) can be introduced through either the bulk geometry on the gravity side of the duality, or the boundary fluid on the field theory side [19, 20]. By using holography, large rotating BH solutions can be constructed from the rotating solutions of the dual fluids [67]. Applying the duality in the other direction, fluid flows seen in heavy-ion collisions can also be modelled by rotating BHs [36], and these are the MP BHs we focus on in this review. MP BHs have been the gravity dual of choice for modelling the rotational properties of the QGP. To see how this came about, it is useful to consider first their simpler counterparts in lower dimensions, which we outline below.

#### 2.3.1. Lower-dimensional black holes

The gravitational physics of rotating BHs offers unique challenges, not least the general form of their solution is often complicated. It is often desirable, then, to consider simple cases that retain the primary features of interest, and lower dimensional BH solutions to the Einstein field equations have long been sought after for their potential to simplify analysis.<sup>4</sup> One such solution that is of great interest to the holography commu-

---

<sup>4</sup>As pointed out by Witten [68], (2+1)-dimensional gravity with (or without) a cosmological constant is exactly soluble at both classical and quantum levels. This property is special to gravity in three spacetime dimensions where it is topological; indeed, the (2+1)-dimensional Einstein-Hilbert action is equivalent to a (topological) Chern-Simons gauge theory. Although this special character of the (2+1)-dimensional gravity can be useful, it leads to some dimension-specific complications [68, 69].



nity is the Bañados-Teitelboim-Zanelli (BTZ) BH in  $(2+1)$ -dimensions. It was originally obtained in [70], and its most general form, as characterized by a set of “hairs” (mass, charge and angular momentum), was extensively explored [71, 72, 73, 74, 75, 76, 77].

The BTZ BH is a solution to the field equations prescribed by the action <sup>5</sup>

$$S_{2+1} = \frac{1}{16\pi G_3} \int d^3x \sqrt{-g} (R - 2\Lambda) , \quad (2)$$

where  $G_3$  is the three-dimensional Newton’s constant, and  $\Lambda = -1/l^2$  is the cosmological constant with  $l$  the  $\text{AdS}_3$  radius. It is typically written in terms of the metric [71]

$$ds^2 = -(N^\perp)^2 dt^2 + (N^\perp)^{-2} dr^2 + r^2 (d\phi + N^\phi dt)^2 , \quad (3)$$

$$N^\perp = \left( -M + \frac{r^2}{l^2} + \frac{J^2}{4r^2} \right)^{1/2} , \quad N^\phi = -\frac{J}{2r^2} , \quad (|J| \leq Ml) . \quad (4)$$

This metric is an axially symmetric, stationary solution to the Einstein equations with Killing vectors  $\partial_t$  and  $\partial_\phi$ . It is characterized by the ADM mass ( $M$ ) and angular momentum ( $J$ ). The BTZ BH retains many of the salient features of its higher dimensional counterparts. For example, it has both an outer and inner event horizon

$$r_\pm^2 = \frac{Ml^2}{2} \left( 1 \pm \sqrt{1 - \left( \frac{J}{Ml} \right)^2} \right) , \quad (5)$$

it has an ergo sphere

$$r_{erg} = M^{1/2} l , \quad (6)$$

determined by the vanishing of  $g_{tt}$  and it has a Hawking temperature determined by the surface gravity of the Killing horizon at  $r_+$  (which agrees with the periodicity of the Euclidean time circle)

$$\kappa_{r_+} = \left( -\frac{1}{2} \nabla^a \chi^b \nabla_a \chi_b \right)^{1/2} = \frac{r_+^2 - r_-^2}{r_+ l^2} = 2\pi T . \quad (7)$$

These features make the BTZ BH an excellent proxy for investigating BH physics without having to deal with the extra computational complications associated with higher dimensional BHs.

The BTZ BH has also played a very important role in the development of the AdS/CFT correspondence. Examples of this include the identification of the asymptotic symmetry algebra [78] and matching of entropy [79], detailed calculation of two point functions of single trace scalar operators and various other probes of AdS/CFT [80, 81, 82], and conjectures on the operator growth and scrambling in quantum chaos [43, 83, 44]. We remark here that while widely used to understanding AdS/CFT in the  $(2+1)$ -dimensional setting, it is mostly the  $J = 0$  case of the general BTZ solution given in Eq. (3) that was discussed, though lately the  $J \neq 0$  case has received more attention from works such as [84, 85] examining the universal bound on quantum chaos in rotating systems.

So far, we have focused on the rotating BH solution in three-dimensional gravity, the BTZ BH. In four-dimensional gravity, the corresponding rotating BH solution is known

---

<sup>5</sup>Here only the uncharged BTZ solution is considered.

as the Kerr BH [19]. It is an object very much more complicated than the BTZ BH, and a detailed account of its idiosyncrasies and the large body of work analyzing it is a huge subject which we will not enter into here [86]. We shall remark only that the Kerr(-AdS) BH has played a key role in the development of the holographic correspondence between AdS BHs and rotating states as pioneered in [19, 20], and this laid the foundation for generalization to higher (five) dimensions more appropriate for the study of real-life, rotating and strongly interacting plasma.

### 2.3.2. Five-dimensional black holes

Although lower-dimensional BHs may share many characteristics with their higher-dimensional counterparts, certain features are present only at higher dimensions. For example, angular momentum is a pseudo-vector only in three spatial dimensions ( $D = 3$ ). Note that for  $D > 3$ , rotating AdS BHs with spherical horizon symmetry are allowed in general [37]<sup>6</sup>, while non-spherical topologies are allowed for axially symmetric BHs [87, 88, 89].

After the the first proposal of a dual gravity description of rotating states in a CFT was put forward in [19], an enormous body of literature has emerged devoted to the study of higher dimensional generalizations of the originally used Kerr BH solution [90]. What appears most interesting and relevant for the study of the QGP is the five-dimensional MP BH. As the QGP lives in (3+1)-dimensions, it is natural that the candidate gravity dual to model it holographically should have one more (spatial) dimension. It may be the case that in some simplifying regimes the QGP could be regarded as lower-dimensional and thereby be modelled by a simpler lower-dimensional gravity dual, but the ability to generalize back to the full system is by no means guaranteed. For instance, transport effects in lower dimensions may have no (3+1)-dimensional counterparts, such as the Hall viscosity (in the absence of external fields) [91, 92, 93, 35], or they could be altogether different, see for example [92, 35].

In five dimensions, rotating BHs with AdS asymptotics and spherical horizons are of the MP type. We require the former so that holography can work, and we want the latter because the gravity dual of the rotating state is then thermodynamically most favorable. There has been significant progress in our technical ability to work with MP BHs in the past fifteen years, and this has provided us with a great resource, in conjunction with holography, to gain new insights into relativistic rotating and strongly interacting fluids with MP BHs. As we shall see, the technical advancements of great importance are the demonstration of separability of linearized Einstein equations [23, 24, 25] (Sec. 3.2), the understanding of relativistic fluids on spheres in [50] and its interpretation as a model of vortical plasma [36]<sup>7</sup> (Sec. 3.3), and further development of solutions to linearized metric equations of motion [29] (Sec. 4.2.1).

## 3. The five-dimensional holographic setup

In this section we describe the holographic framework we work in, the background metric we focus on, and the separability of the equations of motion for the metric fluc-

---

<sup>6</sup>They are, however, susceptible to linear instabilities known as the superradiant instabilities [24].

<sup>7</sup>Note that rotating BHs have been suggested before to model aspects of rotation and vorticity in QGP. This was made in the rotation/magnetism analogy put forward in [94, 95, 96], and in modelling gluodynamics and the deconfinement phase transition in a boosted fluid approximation [97].

tuations around the background metric. Our discussion of the separability of the field equations follows closely the original work [23].

### 3.1. Rotating background metric and black hole thermodynamics

We are interested in the metric fluctuations around stationary (4+1)-dimensional, asymptotically AdS metrics <sup>8</sup>, which are solutions to the equations of motion obtained from the Einstein-Hilbert action

$$S_{EH} = \frac{1}{16\pi G_5} \int d^5x \sqrt{-g} (R - 2\Lambda) + S_{ct}. \quad (9)$$

Here,  $\Lambda = -6/\ell^2$  denotes the cosmological constant given in terms of the AdS radius,  $G_5$  is the five-dimensional Newton's constant, and  $S_{ct}$  is the counterterm action containing the Gibbons-Hawking-York boundary term required for a well-defined variation and other counterterms required to render the boundary action finite. Variation of  $S_{EH}$  leads to the standard source free Einstein equations with cosmological constant

$$R_{\mu\nu} - \frac{1}{2}(R - 2\Lambda)g_{\mu\nu} = 0. \quad (10)$$

Given our focus on the finite temperature rotating states of the dual field theory, we are interested in the most general rotating BH solution with boundary topology  $\mathbb{R} \times S^3$

---

<sup>8</sup>Whether a spacetime can be called *asymptotically AdS* is a rather subtle issue that was carefully examined in [98]. Here, we briefly recapitulate the salient points. Given a conformally compact manifold  $\mathcal{M}$  that solves the Einstein equations, the metric near the boundary can always be brought to the form

$$ds^2 = \frac{dz^2}{z^2} + \frac{1}{z^2} g_{ij}(x, z) dx^i dx^j, \quad g(x, z) = g_{(0)} + z g_{(1)} + \dots + z^d g_{(d)} + h_{(d)} z^d \log z^2 + \dots. \quad (8)$$

With this expansion we can distinguish between three types of AdS spacetimes (in d+1 dimensions):

- AdS<sub>d+1</sub>: A maximally symmetric solution to the Einstein equations that is conformally flat, and has a conformal boundary with topology  $\mathbb{R} \times S^{d-1}$ . Expanding the metric as in Eq. (8) it terminates at order  $z^d$ , and  $g_{(0)}$  can be chosen to be the standard metric on  $\mathbb{R} \times S^{d-1}$ .
- Asymptotically AdS<sub>d+1</sub>: These solutions also have a conformally flat representative  $g_{(0)}$ , and all coefficients up to order  $z^d$  are the same as AdS<sub>d+1</sub> but  $g_{(d)}$  differs. There are no logarithms in either of the above cases.
- Asymptotically Locally AdS<sub>d+1</sub>: These solutions can have an arbitrary conformal structure, a general  $g_{(d)}$ , the logarithms in general do not vanish, and there is no a priori restriction on the topology of the conformal boundary.

The techniques developed in [98] were necessary to end the confusion regarding the variational procedure and the correct definition of charges for MP BH spacetimes. A succinct summary of the many issues up leading to this work is efficiently recounted in [21].

to the Einstein equations.<sup>9</sup> The solution is given by the following metric [19, 20]

$$\begin{aligned}
ds^2 = & \frac{(1 + r_H^2/\ell^2)}{\rho^2 r_H^2} \left( ab dt_H - \frac{b(a^2 + r_H^2) \sin^2(\theta_H)}{\Xi_a} d\phi_H - \frac{a(b^2 + r_H^2) \cos^2(\theta_H)}{\Xi_b} d\psi_H \right)^2 \\
& - \frac{\Delta_r}{\rho^2} \left( dt_H - \frac{a \sin^2(\theta_H)}{\Xi_a} d\phi_H - \frac{b \cos^2(\theta_H)}{\Xi_b} d\psi_H \right)^2 + \frac{\rho^2}{\Delta_\theta} d\theta_H^2 + \frac{\rho^2}{\Delta_r} dr_H^2 \\
& + \frac{\Delta_\theta \sin^2(\theta_H)}{\rho^2} \left( a dt_H - \frac{a^2 + r_H^2}{\Xi_a} d\phi_H \right)^2 + \frac{\Delta_\theta \cos^2(\theta_H)}{\rho^2} \left( b dt_H - \frac{b^2 + r_H^2}{\Xi_b} d\psi_H \right)^2,
\end{aligned} \tag{11}$$

with coordinates  $(r_H, t_H, \theta_H, \phi_H, \psi_H)$  residing in ranges

$$-\infty < t_H < \infty, \tag{12a}$$

$$0 \leq r_H < \infty, \tag{12b}$$

$$0 \leq \theta_H \leq \pi/2, \tag{12c}$$

$$0 \leq \phi_H < 2\pi, \tag{12d}$$

$$0 \leq \psi_H < 2\pi, \tag{12e}$$

and we define

$$\Delta_r = \frac{1}{r_H^2} (r_H^2 + a^2)(r_H^2 + b^2) \left( \frac{r_H^2}{\ell^2} + 1 \right) - 2M, \tag{13}$$

$$\Delta_\theta = 1 - \frac{a^2}{\ell^2} \cos^2(\theta_H) - \frac{b^2}{\ell^2} \sin^2(\theta_H), \tag{14}$$

$$\rho^2 = r_H^2 + a^2 \cos^2(\theta_H) + b^2 \sin^2(\theta_H), \tag{15}$$

$$\Xi_a = 1 - \frac{a^2}{\ell^2}, \quad \Xi_b = 1 - \frac{b^2}{\ell^2}. \tag{16}$$

Although originally discovered in [19], this solution is referred to as the Myers-Perry BH due to the pioneering work of Malcolm Perry and Robert Myers to extend Kerr BHs to higher dimensions [18].<sup>10</sup> The solution features two rotational parameters,  $(a, b)$ , related to the two angular momenta,  $(J_\phi, J_\psi)$ . This can be anticipated from the fact that in (4+1)-dimensions the rotation group is  $SO(4)$  whose double cover is  $SU(2) \times SU(2)$ ; irreducible representations of the rotation group are thus labeled by two parameters. It is however important to note that the full  $SO(4)$  is not present in the solution, Eq. (11), which is only invariant under time translations and the two  $U(1)$  transformations associated with independent rotations in  $(\phi_H, \psi_H)$ .

The two angular momenta,  $(J_\phi, J_\psi)$ , are given by [98]

$$J_\phi = \frac{4\pi^2 M}{\kappa^2 \Xi_a^2 \Xi_b} a, \quad J_\psi = \frac{4\pi^2 M}{\kappa^2 \Xi_a \Xi_b^2} b, \tag{17}$$

<sup>9</sup>For higher dimensional BHs we note that other topologies are possible besides  $\mathbb{R}^{1,1} \times S^3$ , e.g. black saturns [99] and black rings [88]. We do not consider these more exotic topologies here.

<sup>10</sup>It should be noted that their generalized Kerr solutions were computed without a cosmological constant. The generalization of the Kerr solution in (3+1)-dimensions to include AdS-dS boundary conditions was found by Carter [17] and subsequently generalized to all higher dimensions by Gibbons, Lu, Page and Pope [22].

where  $\kappa^2 = 8\pi G_5$ . Associated with  $(J_\phi, J_\psi)$  are the two angular velocities,  $(\Omega_a, \Omega_b)$ , which are non-vanishing throughout the entire spacetime.<sup>11</sup> In particular, at the horizon and the conformal infinity, i.e. the AdS boundary, they taken on values

$$\Omega_a|_{hor} = \frac{a - a^3/\ell^2}{a^2 + r_H^{+2}}, \quad \Omega_b|_{hor} = \frac{b - b^3/\ell^2}{b^2 + r_H^{+2}}, \quad (18a)$$

$$\Omega_a|_{bdy} = -a/\ell^2, \quad \Omega_b|_{bdy} = -b/\ell^2, \quad (18b)$$

where  $r_H^+$  denotes the radius of the outer horizon defined as the largest real root of the equation  $\Delta_r = 0$ . Defining the relative angular velocities,  $(\tilde{\Omega}_a, \tilde{\Omega}_b)$ , by the respective differences [98]:

$$\tilde{\Omega}_a = \Omega_a|_{hor} - \Omega_a|_{bdy} = \frac{(1 + r_H^{+2}/\ell^2)}{(a^2 + r_H^{+2})} a, \quad (19a)$$

$$\tilde{\Omega}_b = \Omega_b|_{hor} - \Omega_b|_{bdy} = \frac{(1 + r_H^{+2}/\ell^2)}{(b^2 + r_H^{+2})} b, \quad (19b)$$

we have the quantities thermodynamically conjugate to  $(J_\phi, J_\psi)$ .

As the metric is independent of the coordinates  $(t, \phi, \psi)$ ,  $(\partial_t, \partial_\phi, \partial_\psi)$  are Killing vectors. The combination  $\partial_t + \Omega_a \partial_\phi + \Omega_b \partial_\psi$  is tangent to the null generators of the horizon from which one can obtain the Hawking temperature of the horizon (and thus the temperature of the dual field theory) from the surface gravity of the horizon:

$$T = \frac{r_H^{+4} (a^2/\ell^2 + b^2/\ell^2 + 1) - a^2 b^2 + 2r_H^{+6}/\ell^2}{2\pi r_H^+ (a^2 + r_H^{+2}) (b^2 + r_H^{+2})}. \quad (20)$$

One can notice that there exist extremal solutions for which the temperature vanishes, an explicit relation between the horizon radius and the rotational parameters where this occurs will be given in Sec.3.2.

The first law of BH thermodynamics and the definition of conserved holographic charges can be found in [98] along with the analysis for MP BHs in (4+1)-dimensions. The entropy which appears in this first law is given by the Bekenstein-Hawking formula  $S = A/(4G_5)$ , where  $A$  is area of the event horizon (as given by the integral over the square root of the spatial determinant of the metric evaluated at the event horizon):

$$A = \frac{2\pi^2 (a^2 + r_H^{+2}) (b^2 + r_H^{+2})}{\Xi_a \Xi_b r_H^+}. \quad (21)$$

As usual, the entropy density is obtained from the entropy by dividing out the volume. The relevant volume here is the spatial volume of the boundary metric,  $V_{bdy} = 2\pi^2 \ell^3$ , and thus the entropy density of the dual field theory is

$$s = \frac{S}{V_{bdy}} = \frac{A/(4G_5)}{V_{bdy}} = \frac{\ell (a^2 + r_H^{+2}) (b^2 + r_H^{+2})}{4G_5 r_H^+ (\ell^2 - a^2)(\ell^2 - b^2)}. \quad (22)$$

---

<sup>11</sup>See for instance [100] for an argument about how to obtain the angular velocity by the consideration of a stationary, or ‘‘locally non-rotating’’ observer.

### 3.2. Linearized metric fluctuation equations and separability

As stated in the introduction, our goal is to provide an overview of the recent progress in the analysis of the field equations in (4+1)-dimensional MP BH. To that end we consider perturbations of the metric in Eq. (11) as was done in [23, 24, 29, 32, 33]:

$$g_{\mu\nu}^p dx^\mu dx^\nu = (g_{\mu\nu} + \epsilon h_{\mu\nu} + O(\epsilon^2)) dx^\mu dx^\nu, \quad (23)$$

where  $g$  is the metric satisfying the Einstein equations (at order  $\epsilon^0$ ). Expanding the Einstein equations to leading order in  $\epsilon$ , the perturbation  $h_{\mu\nu}$ , is required to satisfy [100]

$$-\frac{1}{2}\nabla_\mu\nabla_\nu h - \frac{1}{2}\nabla^\lambda\nabla_\lambda h_{\mu\nu} + \nabla^\lambda\nabla_{(\mu}h_{\nu)\lambda} = \frac{2\Lambda}{D-2}h_{\mu\nu}, \quad (24)$$

where  $h = h_{\mu}{}^{\mu} = h_{\nu\mu}g^{\mu\nu}$ , and the covariant derivatives in Eq. (24) are constructed entirely from the background metric  $g_{\mu\nu}$ . Although the metric in Eq. (11) may not be the most complicated solution to the Einstein equations, it is not immediately clear if or when linearized field equations in this geometry are separable. It is typically the case that separability is intimately tied to symmetry, for instance the field equations in a highly symmetric Schwarzschild geometry may be easily separated by considering an expansion in spherical harmonics. Furthermore, for a clever choice of field variables, fields carrying a spin under the little group may be decoupled into invariant sectors. While this may be expected in highly symmetric spacetimes, it is obviously not guaranteed in general. For the (4+1)-dimensional MP BH we consider, separability of the field equations of a propagating spin-2 field was demonstrated in [23] for the case of equal angular momenta.<sup>12</sup> We will follow this technique of decomposition of the field equations in what follows.

#### 3.2.1. Equal angular momenta Myers Perry black hole

The metric in Eq. (11) simplifies in two special cases:

$$(i) \quad J_\phi = J_\psi \quad (a = b), \quad (ii) \quad J_\psi = 0 \quad (b = 0); \quad (25)$$

note the equivalent definition, due to Eq. (17), in terms of the rotational parameters  $a$  and  $b$ . We shall refer to (i) as the equal angular momenta case<sup>13</sup>, and (ii) the singly spinning case. The singly spinning case may be thought of as a more direct analogy to the (3+1)-dimensional Kerr solution, but it is also much more complicated compared to the case where the two angular momenta are equal. Consider the metric given in Eq. (11), and in particular the quantities  $\Delta_\theta$  and  $\rho$ . The  $\theta_H$  dependence goes away when  $a = b$  but not when only  $b = 0$ , and this leads to great simplification in the equal momentum case that does not happen in the singly spinning case. For instance, the angular velocity

---

<sup>12</sup>Separability of the field equations for dimensions larger than six was demonstrated in [101] for equal angular momenta.

<sup>13</sup>Note that this has been referred to as the simply spinning case by some of us in the past. We shall not use that terminology here as it may be misleading. As we discuss at the end of this subsection, we work with coordinates related to the Hopf fibration with all angular velocities placed onto the interlocking  $S^1$  fibers of the base  $S^2$ ; topologically, the rotation described involves synchronization of the  $S^1$  fibers which may not be “simple” at all.

associated with a zero momentum observer <sup>14</sup> in the two special cases are given by

$$(i) \quad \Omega_a = \Omega_b = \frac{a(\ell^2 - a^2)(a^4 + 2a^2r_H^2 - 2M\ell^2 + r_H^4)}{\ell^2 [a^6 - r_H^4\ell^2 - a^4(\ell^2 - 2r_H^2) + a^2(r_H^4 - 2r_H^2\ell^2 - 2M\ell^2)]}, \quad (26)$$

$$(ii) \quad \Omega_a = \frac{a(\ell^2 - a^2)[a^2(a^2 + r_H^2)\cos^2(\theta_H) + a^2r_H^2 - 2M\ell^2 + r_H^4]}{\ell^2 D_a}, \quad \Omega_b = 0, \quad (27)$$

where

$$D_a = a^2(a^2 + r_H^2)^2 \cos^2(\theta_H) - \ell^2(a^2 + r_H^2)^2 + a^2[a^2(r_H^2 + \ell^2) + r_H^4 + r_H^2\ell^2 - 2M\ell^2] \sin^2(\theta_H). \quad (28)$$

Again, in the equal momentum case the angular velocity is independent of the angular coordinate  $\theta_H$ , and this independence is at the heart of what allows for a great simplification in the fluctuation equations (as a result of a symmetry enhancement as we shall see later). Going forward, we shall focus on the equal momentum case.

After setting  $a = b$ , consider the following coordinate transformation:

$$\theta_H = \frac{\theta}{2}, \quad \phi_H = \frac{1}{2} \left( \frac{2a}{\ell^2} t + \psi - \phi \right), \quad \psi_H = \frac{1}{2} \left( \frac{2a}{\ell^2} t + \psi + \phi \right), \quad (29a)$$

$$t_H = -t, \quad r_H = \sqrt{r^2 - \frac{a^2(r^2 + \ell^2)}{\ell^2}}, \quad M = \mu(1 - a^2\ell^{-2})^3, \quad (29b)$$

where we have defined the effective mass parameter  $\mu$ . Note that, importantly, the coordinate ranges are now given by

$$-\infty < t < \infty, \quad (30a)$$

$$0 \leq r < \infty, \quad (30b)$$

$$0 \leq \theta \leq \pi, \quad (30c)$$

$$0 \leq \phi < 2\pi, \quad (30d)$$

$$0 \leq \psi < 4\pi. \quad (30e)$$

Under the transformation of Eq. (29) the metric is brought to the form first described in [23, 24]

$$ds^2 = \frac{dr^2}{G(r)} - dt^2 \left( \frac{r^2}{\ell^2} + 1 \right) + \frac{1}{4} r^2 ((\sigma^1)^2 + (\sigma^2)^2 + (\sigma^3)^2) + \frac{2\mu \left( \frac{a\sigma^3}{2} + dt \right)^2}{r^2}, \quad (31)$$

with the blackening factor given by

$$G(r) = -\frac{2\mu(1 - a^2/\ell^2)}{r^2} + \frac{2a^2\mu}{r^4} + \frac{r^2}{\ell^2} + 1, \quad (32)$$

and we have introduced the one-forms  $\sigma^a$ ,  $a = 1, 2, 3$ , defined by

$$\begin{aligned} \sigma^1 &= d\phi \sin(\theta) \cos(\psi) - d\theta \sin(\psi), \\ \sigma^2 &= d\theta \cos(\psi) + d\phi \sin(\theta) \sin(\psi), \\ \sigma^3 &= d\psi + d\phi \cos(\theta). \end{aligned} \quad (33)$$

---

<sup>14</sup>Note this is how Eq. 18 was obtained.

The location of the (outer) event horizon in this set of coordinates corresponds to the largest positive real root of the polynomial equation  $G(r_+) = 0$ . Expanding this equation one can define a relation between the horizon radius  $r_+$  and the effective mass  $\mu$ :

$$\mu = \frac{r_+^4 (\ell^2 + r_+^2)}{2\ell^2 r_+^2 - 2a^2 (\ell^2 + r_+^2)}. \quad (34)$$

In terms of the redefined parameters and coordinates <sup>15</sup> the Hawking temperature, in particular, is given by

$$T = \frac{r_+^2 \ell^2 (2r_+^2 + \ell^2) - 2a^2 (r_+^2 + \ell^2)^2}{2\pi r_+^2 \ell^3 \sqrt{r_+^2 \ell^2 - a^2 (r_+^2 + \ell^2)}}, \quad (35)$$

and the entropy density of the dual field theory has the expression

$$s = \frac{r_+^4}{4G_5 \ell^2 \sqrt{r_+^2 \ell^2 - a^2 (r_+^2 + \ell^2)}}. \quad (36)$$

The extremal value of the rotational parameter,  $a_{\text{ext}}$ , at which the temperature vanishes is given by

$$a_{\text{ext}} = \pm \frac{r_+^2}{1 + r_+^2/\ell^2} \sqrt{\frac{1}{2r_+^2} + \frac{1}{\ell^2}}. \quad (37)$$

For  $a = b$ , the two angular momenta as well as the associated angular velocities coincide, i.e.,  $J_a = J_b = J$  and  $\Omega_a = \Omega_b = \Omega$ . The Smarr relation of the equal momentum BH now contains identical factors related to the contribution from the rotation, namely  $\sum_i J_i \tilde{\Omega}_i = 2J\tilde{\Omega}$ , where  $\tilde{\Omega}$  is the thermodynamically relevant angular velocity. Note that the coordinate transformation given in Eq. (29) does two things to the angular coordinates: first is a shift to co-rotating coordinates at the conformal boundary, second is a mixing of the angular coordinates that leads to the linking circles of the Hopf fibration. Indeed, if we repeat the calculation of the angular velocity associated with the new Killing vectors  $(\partial_\phi, \partial_\psi)$  at the horizon and the AdS boundary, they taken on values

$$\Omega_\phi|_{\text{hor}} = 0, \quad \Omega_\psi|_{\text{hor}} = -2a \left( \frac{1}{\ell^2} + \frac{1}{r_+^2} \right), \quad (38a)$$

$$\Omega_\phi|_{\text{bdy}} = 0, \quad \Omega_\psi|_{\text{bdy}} = 0. \quad (38b)$$

Likewise the relative angular velocities <sup>16</sup>,  $(\tilde{\Omega}_\phi, \tilde{\Omega}_\psi)$ , given by the respective differences becomes [98]

$$\tilde{\Omega}_\phi = \Omega_\phi|_{\text{hor}} - \Omega_\phi|_{\text{bdy}} = 0, \quad (39a)$$

$$\tilde{\Omega}_\psi = \Omega_\psi|_{\text{hor}} - \Omega_\psi|_{\text{bdy}} = -2a \left( \frac{1}{\ell^2} + \frac{1}{r_+^2} \right). \quad (39b)$$

Clearly, while  $\partial_\phi$  remains a Killing vector, there is no longer any motion in this direction. Instead, in this new set of coordinates where  $\psi$  denotes the position along the  $S^1$  fiber,

<sup>15</sup>The thermodynamic data displayed in previous sections are in the Boyer-Lindquist coordinate system used in [19, 20].

<sup>16</sup>Notice that thermodynamic value of the angular velocity is identical to the horizon value.



all spacetime motion can be thought of as being along the fiber coordinates (which varies as a function of the holographic coordinate,  $r$ ). Therefore, the spacetime motion in these coordinates is characterized by synchronously moving  $S^1$  Hopf links. Given that there is only motion along  $\psi$ , we will relabel  $\tilde{\Omega}_\psi$  as  $\tilde{\Omega}'$ .

The angular momentum thermodynamically conjugate to  $\tilde{\Omega}'$  can be found simply by substituting  $\mu$  for  $M$  and identifying  $a = b$  in Eq. 17. Recall that under time reversal  $J \rightarrow -J$ , the resulting expression is thus

$$J' = -\frac{4a\pi^2\mu}{\kappa^2}. \quad (40)$$

As expected, it is easy to check that we have not physically changed the system and the Smaar relations agree:  $\sum_i J_i \tilde{\Omega}_i = 2J\tilde{\Omega} = J'\tilde{\Omega}'$ .

### 3.2.2. Symmetries and separable field equations

With the thermodynamic information associated with the metric in these new coordinates recounted, we now turn to the symmetries of the metric. We begin our discussion with the form basis  $\sigma^a$  introduced in Eq. (33). These forms are the left-invariant 1-forms of the group  $SU(2)$ .<sup>17</sup> Dual to the left-invariant 1-forms are the left-invariant vector fields  $\sigma_a$  (which can be expanded in a basis  $E_a$  of the tangent space):<sup>18</sup>

$$\begin{aligned} \sigma_1 &= -\sin\psi \partial_\theta + \frac{\cos\psi}{\sin\theta} \partial_\phi - \cos\theta \sin\phi \partial_\psi, \\ \sigma_2 &= \cos\psi \partial_\theta + \frac{\sin\psi}{\sin\theta} \partial_\phi - \cot\theta \sin\psi \partial_\psi, \\ \sigma_3 &= \partial_\psi. \end{aligned} \quad (41)$$

Expanding in the coordinate basis spanned by  $Y = (\theta, \phi, \psi)$ , the components of the left-invariant 1-forms are given by  $\sigma^a = \sigma_i^a dY^i$ , while that of the left-invariant vector fields are given by  $\sigma_a = \sigma_a^i \partial_i$ , and by definition  $\sigma_i^a \sigma_b^i = \delta_b^a$ . Likewise, one can write down the right-invariant 1-forms and their dual right-invariant vector fields. While the right-invariant 1-forms are not used here, the right-invariant vector fields are used in what follows, they

---

<sup>17</sup>We recall here some basic results of the theory of Lie groups and their algebras (see for instance [102] or the classic text [103]; also [104] covers explicitly the  $SU(2)$  case of interest here). Let  $E^a$  ( $E_a$ ) be a basis of the cotangent (tangent) space at the unit element of a group  $G$ , the left invariant 1-forms on  $G$  are generated by  $E^a$ . Given a parameterization of a generic element of the group,  $A$ , the left-invariant 1-forms (also known as the Maurer-Cartan form) can be found from  $A^{-1}dA = \sigma^a E_a$ ; the right-invariant 1-forms,  $\xi^a$ , are likewise given by  $dAA^{-1} = \xi^a E_a$ . In the case of  $SU(2)$ , the standard basis of the algebra  $su(2)$  that we work in is given by  $E_a = -\frac{1}{2}i\tau_a$ , where  $\tau_a$  are the Pauli matrices. Parameterize  $A \in SU(2)$  as

$$A = \begin{pmatrix} z & -w^* \\ w & z^* \end{pmatrix}, \quad z = \cos(\theta/2)e^{-i(\psi+\phi)}, \quad w = \sin(\theta/2)e^{-i(\psi-\phi)},$$

where  $(\theta, \psi, \phi)$  range as in Eq. (30), one would get  $\sigma^1 = -d\phi \sin(\theta) \cos(\psi) + d\theta \sin(\psi)$  in the standard basis, and the same for  $\sigma_1$  but with a corresponding opposite sign. Since a constant multiple of a left-invariant field is still a left invariant field and  $\sigma^1$  only appears in the metric as  $(\sigma^1)^2$ , we redefine these as displayed in the text.

<sup>18</sup>Note that Refs. [23, 24, 25, 29, 32, 33] make the non-standard choice of labelling the vector fields dual to  $\sigma^a$  with a different symbol,  $e$ , rather than  $\sigma^a$  with the index lowered. In order to clear the notational mine-field surrounding the discussion of separability in MP BHs, we change to the standard notation in this work.

are given by <sup>19</sup>

$$\begin{aligned}\xi_1 &= \cos \phi \partial_\theta + \frac{\sin \phi}{\sin \theta} \partial_\psi - \cot \theta \sin \phi \partial_\phi, \\ \xi_2 &= -\sin \phi \partial_\theta + \frac{\cos \phi}{\sin \theta} \partial_\psi - \cot \theta \cos \phi \partial_\phi, \\ \xi_3 &= \partial_\phi.\end{aligned}\tag{42}$$

Naturally the left-invariant 1-forms are invariant under the action of a right translation generated by the curve  $\xi_a$  which can be written as the Lie derivative of  $\sigma^b$  along  $\xi_a$ , i.e.  $\mathcal{L}_{\xi_a} \sigma^b = 0$ . Furthermore since these do not involve the temporal or radial coordinates it is then easy to see this can be extended to the whole metric  $\mathcal{L}_{\xi_a} g_{\mu\nu} = 0$  and hence the  $\xi_a$  constitute a set of Killing vectors generating an  $SU(2)$  symmetry of the spacetime. Furthermore, since the metric contains no explicit time dependence there exists a time translation symmetry generated by  $\partial_t$ . And, finally, while not obvious in the form notation it can be shown that

$$\mathcal{L}_{\sigma_3} \sigma^1 = -\sigma^2, \quad \mathcal{L}_{\sigma_3} \sigma^2 = \sigma^1, \quad \mathcal{L}_{\sigma_3} \sigma^3 = 0,\tag{43}$$

and therefore  $\sigma_3 = \partial_\psi$  generates an additional  $U(1)$ . Hence the full isometry group of the equal angular momenta MP BH metric given in Eq. (31) is  $\mathbb{R}_t \times (SU(2) \times U(1))/\mathbb{Z}_2$  [24], generated by  $(\xi_a, \sigma_3, \partial_t)$ . Given this set of isometries the separability of the field equations can be demonstrated, as in [23], by considering irreducible representations of  $SU(2) \times U(1)$ .

Defining the differential operators  $W_a = i\sigma_a$  and  $L_a = i\xi_a$  one can check that the following commutation relations are satisfied:

$$[L_a, L_a] = i\epsilon_{abc} L_c \quad [W_a, W_b] = -i\epsilon_{abc} W_c \quad [W_a, L_b] = 0\tag{44}$$

and the symmetry group of interest,  $SU(2) \times U(1)$ , is generated by  $L_a$  and  $W_3$ . In addition, one can show that the left- and right-invariant operators share the same quadratic Casimir  $L_a L_a = W_a W_a = L^2$ . As a result  $L^2$ ,  $L_3$ , and  $W_3$ , are compatible (mutually commuting operators) which can be simultaneously diagonalized. The eigenfunctions associated with this set of compatible operators are the Wigner-D functions,  $D_{\mathcal{K}\mathcal{M}}^{\mathcal{J}}$  [23] which obey the following operator equations

$$L^2 D_{\mathcal{K}\mathcal{M}}^{\mathcal{J}} = \mathcal{J}(\mathcal{J} + 1) D_{\mathcal{K}\mathcal{M}}^{\mathcal{J}},\tag{45}$$

$$L_3 D_{\mathcal{K}\mathcal{M}}^{\mathcal{J}} = \mathcal{M} D_{\mathcal{K}\mathcal{M}}^{\mathcal{J}},\tag{46}$$

$$W_3 D_{\mathcal{K}\mathcal{M}}^{\mathcal{J}} = \mathcal{K} D_{\mathcal{K}\mathcal{M}}^{\mathcal{J}}.\tag{47}$$

The Wigner-D functions, expanded in coordinate basis  $D_{\mathcal{M}\mathcal{K}}^{\mathcal{J}}(\psi, \phi, \theta)$ , for different  $\mathcal{J}$  are mutually orthogonal when integrated over the volume of  $SU(2)$ , defined in Eq. (30)

$$\int_0^{4\pi} d\psi \int_0^\pi d\theta \sin(\theta) \int_0^{2\pi} d\phi D_{\mathcal{K}_2 \mathcal{M}_2}^{\mathcal{J}_2*}(\psi, \phi, \theta) D_{\mathcal{K}_1 \mathcal{M}_1}^{\mathcal{J}_1}(\psi, \phi, \theta) = \frac{16\pi^2}{2\mathcal{J}_1 + 1} \delta_{\mathcal{J}_1 \mathcal{J}_2} \delta_{\mathcal{M}_1 \mathcal{M}_2} \delta_{\mathcal{K}_1 \mathcal{K}_2}\tag{48}$$

---

<sup>19</sup>Naively computing the right-invariant forms and vector fields as described in the previous footnote, one would find that  $\xi_1$  and  $\xi_2$  are interchanged along with the 1-forms  $\xi^1$  and  $\xi^2$ . We rearrange them as displayed in the text.

and form a complete set of eigenfunctions

$$\begin{aligned} & \frac{1}{\sin(\theta_1)} \delta(\tilde{\psi} - \tilde{\psi}_1) \delta(\phi - \phi_1) \delta(\theta - \theta_1) \\ &= \sum_{\mathcal{J}=0,1/2,1,\dots}^{\infty} \sum_{\mathcal{K}=-\mathcal{J}}^{\mathcal{J}} \sum_{\mathcal{M}=-\mathcal{J}}^{\mathcal{J}} \frac{2\mathcal{J}+1}{16\pi^2} D_{\mathcal{K}\mathcal{M}}^{\mathcal{J}}(\tilde{\psi}, \phi, \theta) D_{\mathcal{K}\mathcal{M}}^{\mathcal{J}*}(\tilde{\psi}_1, \phi_1, \theta_1). \end{aligned} \quad (49)$$

on  $S^3$  (see for instance [105]).

These commutation relations, Eq. (44), and eigenvalue equations, Eq. (45), are immediately familiar since the Wigner-D functions are precisely the matrix elements of the rotation operator  $\mathcal{D}(R)$  of ordinary, non-relativistic quantum mechanics [106]

$$\mathcal{D}_{\mathcal{K}\mathcal{M}}^{\mathcal{J}} = \langle \mathcal{J}\mathcal{K} | e^{\left(\frac{-i\mathbf{J}\cdot\hat{n}\phi}{\hbar}\right)} | \mathcal{J}\mathcal{M} \rangle. \quad (50)$$

For this reason, we refer to  $\mathcal{J}$  as the total angular momentum. Also, familiar from ordinary quantum mechanics is the ability to raise and lower the eigenvalue of  $L_3$  and  $W_3$  by the action of ladder operators which, for the eigenvalue of  $W_3$ , can be defined as  $W_{\pm} := W_1 \pm iW_2$ . Using (45), we can express the action of  $W_{\pm}$  and  $W_3$  on  $D_{\mathcal{K}\mathcal{M}}^{\mathcal{J}}$  as

$$W_+ D_{\mathcal{K}\mathcal{M}}^{\mathcal{J}} = i\sqrt{(\mathcal{J} + \mathcal{K})(\mathcal{J} - \mathcal{K} + 1)} D_{\mathcal{K}-1 \mathcal{M}}^{\mathcal{J}} \quad (51)$$

$$W_- D_{\mathcal{K}\mathcal{M}}^{\mathcal{J}} = -i\sqrt{(\mathcal{J} - \mathcal{K})(\mathcal{J} + \mathcal{K} + 1)} D_{\mathcal{K}+1 \mathcal{M}}^{\mathcal{J}} \quad (52)$$

$$W_3 D_{\mathcal{K}\mathcal{M}}^{\mathcal{J}} = \mathcal{K} D_{\mathcal{K}\mathcal{M}}^{\mathcal{J}} \quad (53)$$

These ladder operators take a particularly useful form when rewritten in terms of the partial derivatives<sup>20</sup>,  $\partial_{\pm} = \sigma_{\pm}^a \partial_a$  and  $\partial_3 = \sigma_3^a \partial_a$

$$\partial_+ D_{\mathcal{K}\mathcal{M}}^{\mathcal{J}} = \sqrt{(\mathcal{J} + \mathcal{K})(\mathcal{J} - \mathcal{K} + 1)} D_{\mathcal{K}-1 \mathcal{M}}^{\mathcal{J}} \quad (54)$$

$$\partial_- D_{\mathcal{K}\mathcal{M}}^{\mathcal{J}} = -\sqrt{(\mathcal{J} - \mathcal{K})(\mathcal{J} + \mathcal{K} + 1)} D_{\mathcal{K}+1 \mathcal{M}}^{\mathcal{J}} \quad (55)$$

$$\partial_3 D_{\mathcal{K}\mathcal{M}}^{\mathcal{J}} = -i\mathcal{K} D_{\mathcal{K}\mathcal{M}}^{\mathcal{J}}. \quad (56)$$

Finally, given that our goal is to use the expressions detailed above to separate the equations of motion of the metric fluctuations it will be advantageous to rephrase the metric in terms of the  $\pm$  basis where  $\sigma^{\pm} = \frac{1}{2}(\sigma^1 \mp i\sigma^2)$  and  $\sigma_{\pm} = \sigma_1 \pm i\sigma_2$ . In this basis, the metric in Eq. (31) now takes the form

$$ds^2 = - \left( 1 + \frac{r^2}{\ell^2} \right) dt^2 + \frac{dr^2}{G(r)} + \frac{r^2}{4} (4\sigma^+ \sigma^- + (\sigma^3)^2) + \frac{2\mu}{r^2} \left( dt + \frac{a}{2} \sigma^3 \right)^2. \quad (57)$$

### 3.2.3. General ansatz for spin-2 fields

We are now in the position to describe the general ansatz for the fluctuations. As originally discussed in [23] the choice of ansatz is facilitated by two parts, a decomposition of coordinate dependence of  $h_{\mu\nu}$  in terms of a suitable basis of eigenfunctions and a compensating choice of frame/basis, i.e. a decomposition of the fluctuation in the invariant basis  $h_{\mu\nu} = h_{ij} \bar{\sigma}_{\mu}^i \bar{\sigma}_{\nu}^j$ . Here we have introduced  $\bar{\sigma}^a$  as an extension of the frame

<sup>20</sup>Note again here  $a = 1, 2, 3$  and  $\partial_a = \partial/\partial Y^a$  where as before  $Y^a$  is the angular set of coordinates  $Y^a = (\theta, \phi, \psi)$

basis <sup>21</sup> defined in Eq. (33) with  $\bar{\sigma}^i = (dt, \sigma^+, \sigma^-, \sigma^3, dr)$ . However when constructing the decomposition it is important to note that  $\bar{\sigma}^b$  are charged under the operator  $W_3$ ,

$$\mathcal{L}_{W_3}\sigma^\pm = \pm\sigma^\pm, \quad \mathcal{L}_{W_3}\sigma^3 = 0. \quad (58)$$

Hence in constructing the ansatz it is important to compensate for the additional charge of the basis under  $W_3$ . This can be written succinctly by introducing the function  $Q$ , defined as

$$Q(\bar{\sigma}^i) = \begin{cases} 0, & i = r, t, 3 \\ 1, & i = + \\ -1, & i = - \end{cases}. \quad (59)$$

This auxiliary function  $Q$  gives the charge of the form basis under the operator  $W_3$ . With it, we write the ansatz for the fluctuations as

$$h_{\mu\nu} = \int d\omega e^{-i\omega t} \sum_{\mathcal{J}=0}^{\mathcal{J}} \sum_{\mathcal{M}=-\mathcal{J}}^{\mathcal{J}} \sum_{\mathcal{K}'=-(\mathcal{J}+2)}^{\mathcal{J}+2} h_{ij}(r, \omega, \mathcal{J}, \mathcal{M}, \mathcal{K}') \bar{\sigma}_\mu^i \bar{\sigma}_\nu^j D_{\mathcal{K}'-Q(\bar{\sigma}^i)-Q(\bar{\sigma}^j)\mathcal{M}}^{\mathcal{J}} \quad (60)$$

One can choose a particular mode since the modes of different  $(\mathcal{J}, \mathcal{K}')$  decouple.

Note, we choose to work in the radial gauge  $h_{r\mu} = 0$ , in order to find solutions to (24) in what follows.

### 3.3. Rigidly rotating fluids and large Myers-Perry black holes

Having detailed the geometry and its thermodynamic data as well as fluctuations around this geometry, it will be useful for interpreting results later to now examine more closely the CFT state dual to the MP BH. To this end, we examine the one-point function of the energy-momentum tensor, and we look at, in particular, the behavior of its timelike eigenvector which corresponds to the fluid velocity. Since the boundary theory is topologically  $\mathbb{R} \times S^3$ , we have two options: either study the fluid velocity in this given geometry, or make contact with a flat spacetime via stereographic projection. The stereographic projection will be of great use to us later as we interpret our results in the context of a CFT in flat spacetime. Our discussion in this section will largely follow that of [98, 36, 32].

#### 3.3.1. Vacuum expectation value of the energy-momentum tensor

There are different ways to construct the one-point function of the energy-momentum tensor. Our focus is primarily on the standard method introduced in [107], which was used in [98] to construct the energy-momentum tensor associated with the MP BH.<sup>22</sup> We discuss also the other method of constructing conserved charges at the boundary of the AdS geometry (in the next subsection). It is an important technical tool, and has crucial connections with the MP BH literature that should never be overlooked.

In the standard method, the essential step is to put the most general rotating BH metric described in Eq. (11) into Fefferman-Graham coordinates, which has the general

<sup>21</sup>In these expressions Latin symbols near the beginning of the alphabet,  $a, b, c$  take values 1, 2, 3 over the angular coordinates, Latin symbols near the middle of the alphabet  $i, j, k$  take the values  $t, 1, 2, 3, r$ .

<sup>22</sup>The counterterm subtraction method was first used to compute the energy-momentum tensor for the Kerr-AdS BH and MP solution with  $a = b$  in [108], while the general case was first considered in [109].

form

$$ds^2 = g_{\mu\nu}^{FG} dx^\mu dx^\nu = \ell^2 \left( \frac{d\rho_{FG}^2}{4\rho_{FG}^2} + \frac{1}{\rho_{FG}} g_{ij} dx^i dx^j \right), \quad (61)$$

$$g_{ij} = g_{ij}^{(0)} + \cdots \rho_{FG}^{d/2} g_{ij}^{(d)} + h_{ij}^{(d)} \rho_{FG}^{d/2} \log \rho_{FG}, \quad (62)$$

where  $i$  runs over the field theory directions<sup>23</sup>. As written, the metric in Eq. (11) is not of this form: the obstruction being the  $\theta_H$ -dependence of  $g_{r_H r_H}$ . The goal, then, is to find a coordinate transformation such that we arrive in the end with  $g_{\rho_{FG} \rho_{FG}}^{FG} = 1/\rho_{FG}^2$  and  $g_{\rho_{FG} \theta}^{FG} = g_{\theta \rho_{FG}}^{FG} = 0$ .<sup>24</sup> A technical issue here is that the required coordinate transformation unfortunately does not have a closed form; to get at it, we have to do a near-boundary expansion and find it order by order.

The simplest way to achieve our goal is to do it in steps. First we would obtain a set of coordinates  $(r', \theta_{FG})$  such that  $g_{r' r'}$  has no dependence on  $\theta_{FG}$  and  $g_{r' \theta_{FG}} = 0$  (to sufficiently high order). This can be done through the ansatz

$$r_H = r' [1 + q(r', \theta_{FG})], \quad \theta_H = \theta_{FG} + e(r', \theta_{FG}). \quad (63)$$

Here  $q(r', \theta_{FG})$  and  $e(r', \theta_{FG})$  are regular functions near the AdS boundary such that  $r'$  and  $r_H$  approach infinity at the same rate while  $\theta_{FG}$  remains a constant. Expanding the metric in Eq. (11) near the boundary ( $r' \rightarrow \infty$ ) and performing the coordinate transformation order-by-order in  $r'$  gives

$$\begin{aligned} r_H &= r' + \frac{a^2 \cos^2(\theta_{FG}) + b^2 \sin^2(\theta_{FG})}{4r'} \\ &\quad - \frac{(a^2 - b^2) [(a^2 - b^2) \cos(4\theta_{FG}) + 2 \cos(2\theta_{FG})(a^2 + b^2 - \ell^2)]}{64r'^3} + O(r'^{-5}) \quad (64) \\ \theta_H &= \theta_{FG} + \frac{(a^2 - b^2) \sin(2\theta_{FG}) [(a^2 - b^2) \cos(2\theta_{FG}) + a^2 + b^2 - 2\ell^2]}{32r'^4}, \\ &\quad - \frac{(a^2 - b^2) \sin(2\theta_{FG})}{128r'^6} \left\{ [(a^2 - b^2) \cos(2\theta_{FG}) + a^2 + b^2 - 2\ell^2] \times \right. \\ &\quad \left. [3(a^2 - b^2) \cos(2\theta_{FG}) + 5a^2 + 5b^2 + 2\ell^2] \right\} + O(r'^{-8}). \quad (65) \end{aligned}$$

The metric in this set of coordinates is not particularly illuminating. It is displayed in full in [98], and one can check that  $dg_{r' r'}/d\theta_{FG} = O(r'^{-7})$  and  $g_{r' \theta_{FG}} = O(r'^{-7})$ .

As  $g_{r' r'}$  is not yet of the form  $g_{r' r'} = 1/r'^2$ , the next step is doing another coordinate transformation,  $r' \rightarrow r_{FG}$ , such that  $g_{r_{FG} r_{FG}}^{FG} = \ell^2/r_{FG}^2$ . This can be accomplished with the ansatz

$$r' = r_{FG} [1 + p(r_{FG})]. \quad (66)$$

As before, expanding with  $r_{FG} \rightarrow \infty$  and performing the coordinate transformation order-by-order we get

$$r' = r_{FG} - \frac{a^2 + b^2 + \ell^2}{4r_{FG}} - \frac{a^4 + 6a^2 b^2 + b^4 + 6\ell^2 (a^2 + b^2) - 16M\ell^2}{64r_{FG}^3} + O(r_{FG}^{-5}). \quad (67)$$

<sup>23</sup>For the five-dimensional MP BH,  $x^i = (t_{FG}, \theta_{FG}, \phi_{FG}, \psi_{FG})$ .

<sup>24</sup>The temporal and the rest of the angular coordinates remain the same in the Fefferman-Graham coordinate system, i.e.  $t_{FG} = t_H$ ,  $\phi_{FG} = \phi_H$  and  $\psi_{FG} = \psi_H$ .

We have now achieved our goal: with  $g_{r_{FG}r_{FG}}^{FG} = \ell^2/r_{FG}^2 + O(r_{FG}^{-6})$ , setting  $r_{FG} = \rho_{FG}^{1/2}$  quickly reveals

$$\ell^2 \frac{dr_{FG}^2}{r_{FG}^2} = \ell^2 \frac{d\rho_{FG}^2}{4\rho_{FG}^2}, \quad (68)$$

and the transformed metric takes precisely the form of Eq. 61.

Note that in applications, it is not necessary to have transformed metric computed to all orders in  $\rho_{FG}$ ; going to sufficiently high order such that the relevant coefficients  $g_{ij}^{(k)}$  can be read off is enough. As a case in point, the standard formula for the energy-momentum tensor gives [107]

$$\langle T_{ij} \rangle = \frac{1}{4\pi G \ell} \left( g_{ij}^{(4)} - \frac{1}{8} (\text{tr}(g^{(2)})^2 - \text{tr}((g^{(2)})^2)) - \frac{1}{2} (g^{(2)})_{ij}^2 + \frac{1}{4} g_{ij}^{(2)} \text{tr}(g^{(2)}) \right), \quad (69)$$

where the trace is done with respect to the boundary metric,  $g^{(0)}$ , the leading term in the expansion of Eq. 61. For the MP BH spacetime,  $g^{(0)}$  is given by

$$\begin{aligned} \ell^2 ds_{bdy}^2 &= \ell^2 g_{ij}^{(0)} dx^i dx^j \\ &= -dt_{FG}^2 + \frac{\ell^2}{\Delta\theta} d\theta_{FG}^2 + \frac{\ell^2 \cos^2(\theta_{FG})}{\Xi_b} d\psi_{FG}^2 + \frac{\ell^2 \sin^2(\theta_{FG})}{\Xi_a} d\phi_{FG}^2 \\ &\quad + dt_{FG} \left( \frac{2a \sin^2(\theta_{FG})}{\Xi_a} d\phi_{FG} + \frac{2b \cos^2(\theta_{FG})}{\Xi_b} d\psi_{FG} \right). \end{aligned} \quad (70)$$

The general form of the energy-momentum tensor (and that of  $g^{(2)}$  and  $g^{(4)}$ ) is not particularly illuminating (for completeness we show it in full in Appendix A as it is not given in [98]). A key fact about it, however, is that it can be separated into two parts:

$$\langle T_{ij} \rangle = \langle T_{ij}^{BH} \rangle + \langle T_{ij}^{AdS} \rangle, \quad (71)$$

where the first term is associated with the contribution from the BH in the bulk, and the second from the vacuum energy of the dual CFT (on the boundary  $\mathbb{R} \times S^3$ ) to the ambient AdS spacetime. This is further evident when computing the conserved charge referred to as the holographic mass. This conserved charge is associated with the Killing vector  $\xi_t = \partial_t - a \ell^{-2} \partial_\phi - b \ell^{-2} \partial_\psi$ , and it is given by

$$\bar{M} = - \int d^3x \sqrt{g^{(0)}} T_j^t \xi^j, \quad (72)$$

$$= \frac{2\pi^2 M (2\Xi_a - 2\Xi_b - \Xi_a \Xi_b)}{\kappa^2 \Xi_a^2 \Xi_b^2} + M_{Casimir}. \quad (73)$$

The Casimir energy is given by

$$M_{Casimir} = \frac{3\pi^2 \ell^2}{4\kappa^2} \left( \frac{(\Xi_a - \Xi_b)^2}{9\Xi_a \Xi_b} + 1 \right), \quad (74)$$

which is in perfect agreement with the vacuum energy of a CFT in a rotating Einstein spacetime whose metric is precisely given by Eq. (70) [110, 109, 111, 98].<sup>25</sup>

---

<sup>25</sup>As noted in [111], the famous factor of 3/4 between strong and weak coupling in  $\mathcal{N} = 4$  SYM does not appear here as pure AdS is protected from stringy corrections; see also [112].

The angular momenta obtained through BH thermodynamics in Eq. (17) are also conserved charges that can be computed from the holographic energy-momentum tensor. Denoting  $J_i = (J_\phi, J_\psi)$  and the corresponding Killing vectors  $\xi_J^i = (\partial_\phi, \partial_\psi)$ , it can be quickly checked that

$$J_i = \int d^3x \sqrt{g^{(0)}} T_j^{tFG} \xi_J^j, \quad (75)$$

which reproduces the result given in Eq. (17).

Finally, from the full expression of  $\langle T^{ij} \rangle$  given in Appendix A we can check explicitly that the Ward identity,  $\nabla_i \langle T^{ij} \rangle = 0$ , is satisfied, and that there is a conformal anomaly

$$\begin{aligned} 4\pi G_5 \langle T_i^i \rangle &= \frac{1}{\ell^3} \left( \frac{1}{8} R^{ij} R_{ij} - \frac{1}{24} R^2 \right) \\ &= \frac{1}{8\ell^5} (a^2 - b^2) [(a^2 - b^2)(3 \cos(4\theta_{FG}) + 1) + 4 \cos(2\theta_{FG})(a^2 + b^2 - 2\ell^2)], \end{aligned} \quad (76)$$

where  $R_{ij}$  and  $R$  are the Ricci tensor and scalar, respectively, built from the boundary metric  $g^{(0)}$ .

### 3.3.2. Ashtekar-Magnon charges, the conformal fluid, and the large black hole limit

The separation of the energy momentum tensor shown in Eq. 71 is very useful as we shall see. To derive it, we now describe another method of obtaining a local stress-energy tensor near the conformal boundary, which was first used to construct conserved charges known as the Ashtekar-Magnon charges [113, 114]. Roughly stated, the energy momentum tensor obtained in this way will differ from that obtained by the *counter-term method* [111] by a *Casimir energy* as shown in [114]. The Ashtekar-Magnon charges are computed from the Ashtekar-Magnon tensor,  $E_j^i$ , which is the electric part of the Weyl tensor. In our choice of coordinates, this is related to the local tensor displayed in Eq. (69) by the formula [113, 114, 98]<sup>26</sup>

$$E_j^i = \langle T_j^i \rangle - \frac{1}{2\kappa^2} H_j^i \ell^3, \quad (77)$$

$$H_j^i = \frac{1}{4} \left( -R^i_k R^k_j + \frac{2}{3} R R^i_j + \frac{1}{2} \left[ R^m_k R^k_m - \frac{1}{2} R^2 \right] \delta_j^i \right). \quad (78)$$

The Ashtekar-Magnon tensor is exactly the energy-momentum tensor of an  $AdS_5$  BH and we identify

$$E_{ij} = \langle T_{ij}^{BH} \rangle, \quad (79)$$

Recall the indices are raised and lowered with the boundary metric,  $g^{(0)}$ .

The Ashtekar-Magnon tensor is a symmetric tensor, i.e.  $E_{ij} = E_{ji}$ . For the MP BH,

---

<sup>26</sup>The process to obtain this formula is rather involved. One must first find a relation between the counter-term method of doing holographic renormalization [107] (which we use in this article) and the Hamiltonian method organized in terms of eigenfunctions of the dilation operator [115]. Only then can one construct a relation between the two sets of conserved tensors as was done in [98]. For full details, see the references cited in this footnote.

its non-zero components are given by (recall  $x^i = (t_{FG}, \theta_{FG}, \phi_{FG}, \psi_{FG})$  in our conventions)

$$\begin{aligned}
E_{00} &= \frac{3M}{\ell\kappa^2}, \\
E_{02} &= -\frac{3aM \sin^2(\theta_{FG})}{\Xi_a \ell \kappa^2}, \\
E_{03} &= -\frac{3bM \cos^2(\theta_{FG})}{\Xi_b \ell \kappa^2}, \\
E_{11} &= \frac{2\ell M}{\kappa^2 (\cos^2(\theta_{FG})(\Xi_a - \Xi_b) + \Xi_a + \Xi_b)}, \\
E_{22} &= \frac{M\ell \sin^2(\theta_{FG}) (-2(1 - \Xi_a)(2\cos^2(\theta_{FG}) - 1) - \Xi_a + 2)}{\kappa^2 \Xi_a^2}, \\
E_{23} &= \frac{abM \sin^2(2\theta_{FG})}{\kappa^2 \Xi_a \Xi_b \ell}, \\
E_{33} &= \frac{M\ell \cos^2(\theta_{FG}) (2(1 - \Xi_b)(2\cos^2(\theta_{FG}) - 1) - \Xi_b + 2)}{\kappa^2 \Xi_b^2}, \tag{80}
\end{aligned}$$

and their symmetric counterparts. We see that  $E_{ij}$  is directly proportional to the BH mass,  $M$ . As the difference between  $E_{ij}$  and  $\langle T_{ij} \rangle$  has no contribution from  $M$ , in the large BH limit where the outer horizon radius  $r_H^+$  and thus  $M = (r_H^+)^4 / (2\ell^2) + O((r_H^+)^2)$  become large, the Ashtekar-Magnon tensor would dominate the full energy-momentum tensor.

The contribution of the Ashtekar-Magnon tensor to the full energy-momentum tensor was studied in detail in [67, 36]. For a relativistic fluid described by it, the solution to the fluid equations turns out to be one associated with a flat spacetime [36].<sup>27</sup> To see this, which shall take some effort as we outline below, consider first the transformation

$$t_{FG} = \tilde{t}\ell, \quad \phi_{FG} = \Phi - a\tilde{t}/\ell, \quad \psi_{FG} = \Psi - b\tilde{t}/\ell, \quad \tan(\theta_{FG})^2 = \frac{\Xi_a}{\Xi_b} \tan(\tilde{\theta})^2. \tag{81}$$

After doing this, we get  $E_{ij} \rightarrow \tilde{E}_{ij}$ , and a static metric (up to a conformal factor) on the  $\mathbb{R} \times S^3$  boundary:

$$\tilde{g}_{ij}^{(b)} dx^i dx^j = \frac{\sec^2(\tilde{\theta})}{\Xi_a \tan^2(\tilde{\theta}) + \Xi_b} \left( -d\tilde{t}^2 + d\tilde{\theta}^2 + d\Psi^2 \cos^2(\tilde{\theta})^2 + d\Phi^2 \sin^2(\tilde{\theta})^2 \right). \tag{82}$$

Going forward, as our interests lie in the large BH limit in which the BH contribution dominates, we shall henceforth disregard the vacuum energy contribution to the energy-momentum tensor and take  $T_{ij} = \tilde{E}_{ij}$  from now on.

To have a (proper) static metric on  $\mathbb{R} \times S^3$  without the conformal factor, we perform another transformation

$$\tilde{g}_{ij}^{(b)'} = e^{-2\Upsilon} \tilde{g}_{ij}^{(b)}, \quad \tilde{g}^{(b)'}{}_{ij} = e^{2\Upsilon} \tilde{g}^{(b)}{}_{ij}, \quad e^{-2\Upsilon} = \ell^2 \cos^2(\tilde{\theta})(\Xi_a \tan^2(\tilde{\theta}) + \Xi_b), \tag{83}$$

and the resulting boundary metric is

$$\tilde{g}_{ij}^{(b)'} dx^i dx^j = \ell^2 \left( -d\tilde{t}^2 + d\tilde{\theta}^2 + d\Psi^2 \cos^2(\tilde{\theta})^2 + d\Phi^2 \sin^2(\tilde{\theta})^2 \right). \tag{84}$$

---

<sup>27</sup>For more information on the conformal fluid dynamics, see e.g. the appendix in [67].



Under this transformation, the energy-momentum tensor goes to  $\tilde{T}'^{ij} = e^{(d+2)\Upsilon} T^{ij}$  with  $d = 4$  the dimension of the boundary theory. By redefining the parameters at the same time:

$$M = m\ell^2, \quad a = \omega_1\ell, \quad b = \omega_2\ell, \quad (85)$$

we get [36]

$$\tilde{T}'^{ij} = \frac{\gamma^6 T_0^4}{3\ell^2} \times \begin{pmatrix} v^2 + 3 & 0 & 4\omega_1 & 4\omega_2 \\ 0 & 1 - v^2 & 0 & 0 \\ 4\omega_1 & 0 & -\omega_2^2 \cot^2(\tilde{\theta}) + \csc^2(\tilde{\theta}) + 3\omega_1^2 & 4\omega_1\omega_2 \\ 4\omega_2 & 0 & 4\omega_1\omega_2 & -\omega_1^2 \tan^2(\tilde{\theta}) + \sec^2(\tilde{\theta}) + 3\omega_2^2 \end{pmatrix}, \quad (86)$$

where

$$T_0 = \left( \frac{3m}{\kappa^2\ell} \right)^{1/4}, \quad \gamma = \frac{1}{\sqrt{1-v^2}}, \quad v = \sqrt{\omega_1^2 \sin^2(\tilde{\theta}) + \omega_2^2 \cos^2(\tilde{\theta})}. \quad (87)$$

This energy-momentum tensor (and others like it) were thoroughly examined in [67]. It corresponds to a conformal,  $\mathcal{N} = 4$  SYM fluid having two independent planes of rigid rotation (with angular velocities  $|\omega_{1,2}| < 1$ ) in the  $\mathbb{R} \times S^3$  geometry described by Eq. (84). The fluid flow,  $u^i$ , and energy density,  $\epsilon$ , can be extracted from the (time-like) eigenvalue problem,  $\tilde{T}'^i_j u^j = -\epsilon u^i$ , which gives

$$u^i = \frac{\gamma}{\ell} (1, 0, \omega_1, \omega_2), \quad \epsilon = \frac{4T_0^4}{(2 - \omega_1^2 - \omega_2^2 + \cos(2\theta) (\omega_1^2 - \omega_2^2))^2}. \quad (88)$$

It can be explicitly checked that Eq. (88) is a solution to the ideal fluid equations (note that the solution is stationary).

To summarize, the Ashtekar-Magnon tensor describes a conformal fluid in  $\mathbb{R} \times S^3$ . It is also the part of the energy-momentum tensor describing a rotating BH in the five-dimensional AdS bulk with an  $\mathbb{R} \times S^3$  boundary. As the Ashtekar-Magnon tensor dominates over the energy-momentum tensor in the large BH limit, we have thus a connection between conformal fluid dynamics and large rotating BHs. This is why the large BH limit of the MP BH is so interesting, and why much of our attention is focused on it below.

### 3.3.3. Stereographic projection and the flat spacetime fluid velocity

We have seen from above that the gravity system in our holographic setup can be interpreted as a dual fluid rotating rigidly in the  $\mathbb{R} \times S^3$  geometry (boundary to the AdS bulk) when terms associated with the Casimir energy have been removed from the energy-momentum tensor<sup>28</sup>. Remarkably, this can also be understood as being equivalent to considering the large BH limit, where the contribution to the energy-momentum tensor associated with the rotating BH in the bulk dominates over the that from the vacuum energy of the dual rotating CFT on the boundary. At this stage, it is almost within our reach to make contact with the physics of rotating systems in flat spacetime. The last step is to perform a stereographic projection from  $\mathbb{R} \times S^3$  to  $\mathbb{R}^{1,3}$ . As we shall see below,

<sup>28</sup>More formally, a redefinition of the energy-momentum tensor by a conserved tensor has taken place.

this has the effect of transforming the fluid velocity, which describes the rigid rotation on  $S^3$ , into a highly non-trivial solution to the ideal, relativistic fluid equations.<sup>29</sup>

To project from  $\mathbb{R} \times S^3$  to the Minkowski spacetime (in spherical polar coordinates), consider the transformation  $(\tilde{t}, \tilde{\theta}, \Phi, \Psi) \rightarrow (t_m, r_m, \theta_m, \phi_m)$ :<sup>30</sup>

$$\begin{aligned}\tilde{t} &= \arctan\left(\frac{2\ell t_m}{\ell^2 + r_m^2 - t_m^2}\right), \\ \tilde{\theta} &= \arctan\left(\frac{2\ell r_m \sin(\theta_m)}{\sqrt{\ell^4 + 2\ell^2 r_m^2 \cos(2\theta_m) + 2\ell^2 t_m^2 + (r_m^2 - t_m^2)^2}}\right), \\ \Phi &= \phi_m, \\ \Psi &= -\arctan\left(\frac{\sec(\theta_m)(\ell^2 - r_m^2 + t_m^2)}{2\ell r_m}\right).\end{aligned}\tag{90}$$

The result of this transformation is a line element of the form

$$\eta_{ij}dx^i dx^j = B^2 (-dt_m^2 + dr_m^2 + d\theta_m^2 + r_m^2 \sin^2(\theta_m) d\phi_m^2).\tag{91}$$

The conformal factor,  $B^2$ , is given by

$$B^2 = \frac{4\ell^4}{2t_m^2(\ell - r_m)(r_m + \ell) + (r_m^2 + \ell^2)^2 + t_m^4},\tag{92}$$

and can be easily removed by a further conformal transformation. With this done, we have in this new set of coordinates the fluid velocity given by<sup>31 32</sup>

$$\begin{aligned}u'^{r_m}/u'^{t_m} &= \frac{\omega_2 \cos(\theta_m)(r_m^2 + t_m^2 + \ell^2) + 2r_m t_m}{2\omega_2 r_m t_m \cos(\theta_m) + r_m^2 + t_m^2 + \ell^2}, \\ u'^{\theta_m}/u'^{t_m} &= -\frac{\omega_2 r_m \sin(\theta_m)(-r_m^2 + t_m^2 + \ell^2)}{r_m(2\omega_2 r_m t_m \cos(\theta_m) + r_m^2 + t_m^2 + \ell^2)}, \\ u'^{\phi_m}/u'^{t_m} &= \frac{2\omega_1 \ell}{2\omega_2 r_m t_m \cos(\theta_m) + r_m^2 + t_m^2 + \ell^2},\end{aligned}\tag{93}$$

---

<sup>29</sup>We follow closely the supplemental material of [36] for the relevant set of coordinate transformations discussed in this subsection.

<sup>30</sup>The transformation here is not the standard  $S^3 \rightarrow \mathbb{R}^3$  projection. There, one typically begins by choosing a point on the sphere,  $q_0$ . Then the stereographic projection of a point,  $q_1$ , on the sphere is the point,  $q'_1$ , given by the intersection of the ray from  $q_0$  to  $q_1$  with  $\mathbb{R}^3$ . When applied to  $\mathbb{R} \times S^3$  (with the metric on  $S^3$  taken to be the standard one in hyperspherical coordinates), the standard project would result in a line element of the form

$$ds^2 = -dt^2 + C(X^2, Y^2, Z^2)(dX^2 + dY^2 + dZ^2),\tag{89}$$

with a non-trivial scale factor on the spatial sections. However, as our goal is to arrive at a boundary theory in Minkowski space, we must use a new time coordinate to have any hope in bringing the spacetime metric to the standard form, and thus the time coordinate transformation made in Eq. (90). The lesson here is that the time coordinate associated with the flat spacetime limit of field theories in  $\mathbb{R} \times S^3$  would not be the same time coordinate as the original curved geometry.

<sup>31</sup>Recall under a conformal transformation of the form  $\eta' = e^{-2\Upsilon'}\eta$  the fluid velocity transforms as  $u'^i = e^{\Upsilon'} u^i$ .

<sup>32</sup>We note here a discrepancy in the supplemental material of [36]: In Eq. (14) there, the denominator of the ratios as we have here is given as (in our notation)  $2\omega_2 r_m t_m \cos(\theta_m) + r_m^2 + \ell^2$ , where the  $t_m^2$  term is missing when compared to our expression. This omission, however, does not carry over into their final result in their Eq. (15).

where

$$u'^{t_m} = \frac{2\omega_2 r_m t_m \cos(\theta_m) + r_m^2 + t_m^2 + \ell^2}{\sqrt{D_{t_m}}}, \quad (94)$$

$$D_{t_m} = (1 - \omega_2^2) [(t_m^2 - r_m^2)^2 - t_m^4 + (t_m^2 + \ell^2)^2] + 2(\omega_1^2 - \omega_2^2) \ell^2 r_m^2 \cos(2\theta_m) + 2(1 - \omega_1^2) \ell^2 r_m^2, \quad (95)$$

and the energy density given by

$$\epsilon' = \frac{16T_0^4 \ell^8}{D_{t_m}}. \quad (96)$$

To have the fluid velocity in a more convenient form, we transform to the Milne coordinates  $(\tau, x_1, x_2, \xi)$ :

$$\begin{aligned} t_m &= \tau \cosh(\xi), \\ r_m &= \cosh(\xi) \sqrt{\tau^2 + \operatorname{sech}^2(\xi) (-\tau^2 + x_1^2 + x_2^2)}, \\ \theta_m &= \arccos \left( \frac{x_2 \operatorname{sech}(\xi)}{\sqrt{\tau^2 + \operatorname{sech}^2(\xi) (-\tau^2 + x_1^2 + x_2^2)}} \right), \\ \phi_m &= \arccos \left( \frac{\tau \tanh(\xi)}{\sqrt{\tau^2 + \operatorname{sech}^2(\xi) (x_1 - \tau)(\tau + x_1)}} \right). \end{aligned} \quad (97)$$

The resulting metric has now the standard form

$$\eta'' = \operatorname{diag}(-1, 1, 1, \tau^2), \quad (98)$$

and the fluid velocity is expressed by <sup>33</sup>

$$\begin{aligned} u''^\tau &= \lambda [\cosh \xi (\ell^2 + \tau^2 + x_\perp^2) + 2(\ell x_1 \omega_1 \sinh \xi + \tau x_2 \omega_2)], \\ u''^1 &= \lambda [2(\ell \tau \omega_1 \sinh \xi + \tau x_1 \cosh \xi + x_1 x_2 \omega_2)], \\ u''^2 &= \lambda [\omega_2 (\ell^2 + \tau^2 - x_1^2 + x_2^2) + 2\tau x_2 \cosh \xi], \\ u''^\xi &= -\tau^{-1} \lambda [\sinh \xi (\ell^2 - \tau^2 + x_\perp^2) + 2\ell x_1 \omega_1 \cosh \xi], \end{aligned} \quad (99)$$

where  $\tau = \sqrt{t^2 - x_3^2}$  is the proper time,  $\xi = \operatorname{arctanh}(x_3/t)$  is the spacetime rapidity and we have defined  $x_\perp^2 = x_1^2 + x_2^2$ . The quantity  $\lambda$  is defined in terms of the energy density, and they are given by

$$\lambda = \left( \frac{\epsilon''}{16\ell^8 T_0^4} \right)^{1/4}, \quad \epsilon'' = \frac{16\ell^8 T_0^4}{D_{\epsilon''}}, \quad (100)$$

where

$$\begin{aligned} D_{\epsilon''} &= (\omega_2^2 - 1) [\ell^4 + (x_\perp^2 - \tau^2)^2] + 2\ell^2 \tau^2 (\omega_1^2 - 1) \cosh(2\xi) \\ &\quad - 2\ell^2 [(\omega_1^2 - \omega_2^2)(\tau^2 + 2x_2^2) + x_\perp^2 (1 - 2\omega_1^2 + \omega_2^2)]. \end{aligned} \quad (101)$$

---

<sup>33</sup>The expressions here differ from that recorded in [36] because our coordinate transformation to the Milne spacetime is different, which has the coordinates  $x$  and  $y$  there (corresponding to our  $x_2$  and  $-x_1$  respectively) reshuffled. We have checked that we get the same expressions if we use the coordinate transformation described in their supplemental material.

As we are interested in the equal momentum case where the rotational parameters are the same,  $a = b$ , and  $\omega_1 = \omega_2 = \Omega$ , the fluid velocity  $u''$  simplifies to

$$\begin{aligned} u^\tau &= \lambda \left[ \cosh \xi (\ell^2 + \tau^2 + x_\perp^2) + 2\Omega(\ell x_1 \sinh \xi + \tau x_2) \right], \\ u^1 &= \lambda \left[ 2(\ell\tau\Omega \sinh \xi + \tau x_1 \cosh \xi + x_1 x_2 \Omega) \right], \\ u^2 &= \lambda \left[ \Omega (\ell^2 + \tau^2 - x_1^2 + x_2^2) + 2\tau x_2 \cosh \xi \right], \\ u^\xi &= -\tau^{-1} \lambda \left[ \sinh \xi (\ell^2 - \tau^2 + x_\perp^2) + 2\ell x_1 \Omega \cosh \xi \right], \end{aligned} \quad (102)$$

which agrees with that displayed in [32]<sup>34</sup>, and the energy density  $\epsilon''$  simplifies to

$$\epsilon = 16\ell^8 T_0^4 (1 - \Omega^2)^{-2} \left[ 2\ell^2 \tau^2 \cosh 2\xi + (\ell^2 + x_\perp^2)^2 + \tau^4 - 2\tau^2 x_\perp^2 \right]^{-2}. \quad (103)$$

Recall further that  $m = \mu(1 - \Omega^2)^3$ , the parameters  $\lambda$  and  $T_0$  are now given by<sup>35</sup>

$$\lambda = \left( \frac{\epsilon}{16\ell^8 T_0^4} \right)^{1/4}, \quad T_0 = \left( \frac{3(1 - \Omega^2)^3 \mu}{8\pi G_5 \ell} \right)^{1/4}. \quad (104)$$

We remark here that the general fluid velocity and energy density,  $u''$  and  $\epsilon''$ , satisfy the relativistic Navier-Stokes equations (as noted in [36]). In conjunction with the associated energy-momentum tensor, this represents a highly non-trivial analytic solution to relativistic hydrodynamical equations referred to as the Bantilan-Ishii-Romatschke (BIR) flow, which is unfortunately little known [36]. Below when interpreting our results in the coming section in the boundary field theory with a flat metric, it is important to recognize that our fluid is undergoing BIR flow.

To gain some intuition about this solution, we show in Fig. 1 the energy density  $\epsilon$  (normalized by the energy scale  $T_0$ ) as a function of rapidity  $\xi$  and spatial coordinate  $x_1/\ell$  (shown as the coloring of the graph), and we superimpose on it the flow vectors generated by  $(u_1, u_\xi)$ . One can see that the energy density (coloring) is nearly uniformly distributed in rapidity at small  $\tau$  (left plot in Fig. 1). This can be easily understood from the  $\xi$ -independence of the leading term when expanding  $\epsilon$  near  $\tau = 0$ :

$$\epsilon = \frac{16\ell^8 T_0^4}{(1 - \Omega^2)^2 (\ell^2 + x_\perp^2)^4} - \frac{64\tau^2 \ell^8 T_0^4 (\ell^2 \cosh(2\xi) - x_\perp^2)}{(1 - \Omega^2)^2 (\ell^2 + x_\perp^2)^6} + O(\tau^2). \quad (105)$$

While symmetric at  $\tau = 0$ ,  $\epsilon$  begins to develop an asymmetric distribution in the  $x_1$ - $\xi$  plane as  $\tau$  increases. Likewise, expanding the fluid velocity to leading order in  $\tau$  makes plain its asymmetry in the  $x_1$ - $\xi$  plane:

$$\begin{pmatrix} u_{x_1} \\ u_\xi \end{pmatrix} = \frac{\tau}{(1 - \Omega^2)^{1/2} (\ell^2 + x_\perp^2)^2} \begin{pmatrix} 2\ell\Omega \sinh(\xi) + 2x_1 \cosh(\xi) \\ -(\ell^2 + x_1^2) \sinh(\xi) - 2\ell x_1 \Omega \cosh(\xi) \end{pmatrix} + O(\tau^4). \quad (106)$$

Going to  $\tau/\ell = 1$  (center plot in Fig. 1),  $\epsilon$  is now concentrated at mid-rapidity, and the asymmetry of the fluid velocity is on full display as it spirals outward. Going further to  $\tau/\ell = 2$  (right plot of Fig. 1),  $\epsilon$  splits into two outgoing pieces (in the  $x_1$  direction) at mid-rapidity. It is rather remarkable that a relatively simple bulk spacetime geometry

<sup>34</sup>There is a sign error in the equation displayed in [32] in  $u^\xi$ . There, the additional overall negative sign should be removed.

<sup>35</sup>Note in [32] the quantity  $T_0$  was labeled as  $\Theta$ . In addition, there was a typo where the cubic power on  $\ell$  should have been on  $(1 - \Omega^2)$ , which is displayed correctly here.

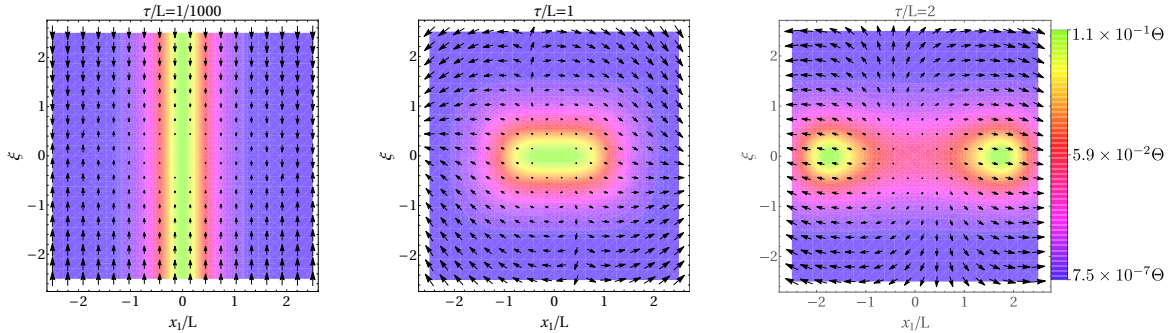


Figure 1: Energy density  $\epsilon$  and flow velocity vectors  $(u_1, u_\xi)$  at different times for  $\Omega = 1/2$  in the  $x_1$ - $\xi$  plane (with  $x_2 = 0$ ). The shading corresponds to level sets of the energy density. For ease of visualization, we have rescaled the energy density by a factor of approximately 250 in the left plot, and 15 in the middle plot. Plots adapted from [32] where  $L$  and  $\Theta$  correspond to the AdS radius  $\ell$  and the energy scale  $T_0$  here.

(through holography) can, with prudent coordinate transformations and rescalings, give rise to a time-dependent flow profile reminiscent of the generic flow expected for the QGP [1, 36].<sup>36</sup>

Looking at Fig. 1 one can see indications of the fluid velocity  $u$  containing non-trivial rotations in the transverse,  $x_1$ - $\xi$  plane. This is indeed the case, and can be made explicit by doing the following. First transform to the Cartesian coordinates<sup>37</sup>, next do a rescaling  $x^i \rightarrow x^i/\alpha$ , last expand around  $\alpha \rightarrow \infty$ , the fluid velocity  $u$  then becomes

$$u'^\mu = \frac{\alpha}{\sqrt{1-\Omega^2}}(1, 0, \Omega, 0) + \frac{2\Omega}{\ell\sqrt{1-\Omega^2}}(0, x_3, 0, -x_1) + O(\alpha^{-1}) \quad (107)$$

The expansion in Eq. (107) is very important to the interpretation of results we discuss below. At leading order (LO), we see that the fluid is uniformly boosted along the  $x_2$  direction.<sup>38</sup> The rotation in the  $x_1$ - $\xi$  plane (about the boost direction  $x_2$ ) advertised above shows up explicitly as the next-to-leading order (NLO) correction to the fluid velocity  $u'$ . In Fig. 2 we compare the full solution,  $u$ , given in Eq. (102) with the series expansion,  $u'$ , given in Eq. 107. To make the comparison in the same coordinates,  $u'$  is inverse transformed back to the Milne coordinates. From left to right, the plots display the contribution to  $u'$  at LO, at LO + NLO, and the full solution  $u$  given in Eq. (102). To aid the visual comparison, the full solution is displayed for a zoomed-in region of the middle plot in Fig. 1.

<sup>36</sup>Note that one can compute explicitly the vorticity  $\omega_{\text{vor}}^i = \frac{1}{2}\epsilon^{ijkl}u_j\nabla_{[k}u_{l]}$ , where  $i$  runs over  $(\tau, x_1, x_2, \xi)$ , and find

$$\begin{aligned} \omega_{\text{vor}}^\tau &= \lambda^{-2} [4\ell\Omega (\Omega \cosh(\xi) (\ell^2 + \tau^2 + x_\perp^2) + 2(\ell x_1 \sinh(\xi) + \tau x_2))] \\ \omega_{\text{vor}}^{x_1} &= \lambda^{-2} [8\ell\Omega(\ell\tau \sinh(\xi) + \tau x_1\Omega \cosh(\xi) + x_1x_2)] \\ \omega_{\text{vor}}^{x_2} &= \lambda^{-2} [4\ell\Omega (\ell^2 + \tau^2 - x_\perp^2 + 2\tau x_2\Omega \cosh(\xi))] \\ \omega_{\text{vor}}^\xi &= -\tau^{-1}\lambda^{-2} [4\ell\Omega (\Omega \sinh(\xi) (\ell^2 - \tau^2 + x_\perp^2) + 2\ell x_1 \cosh(\xi))] \end{aligned}$$

We see that the flow clearly possesses a highly non-trivial vorticity vector.

<sup>37</sup>Recall that the proper time and spacetime rapidity  $(\tau, \xi) = (\sqrt{t^2 - x_3^2}, \text{arctanh}(x_3/t))$  in Cartesian coordinates.

<sup>38</sup>This behavior is precisely what we shall see when we consider the fluctuation equations in the large BH limit (with simultaneous scaling of frequency and momentum); see Sec. 4.2.1.

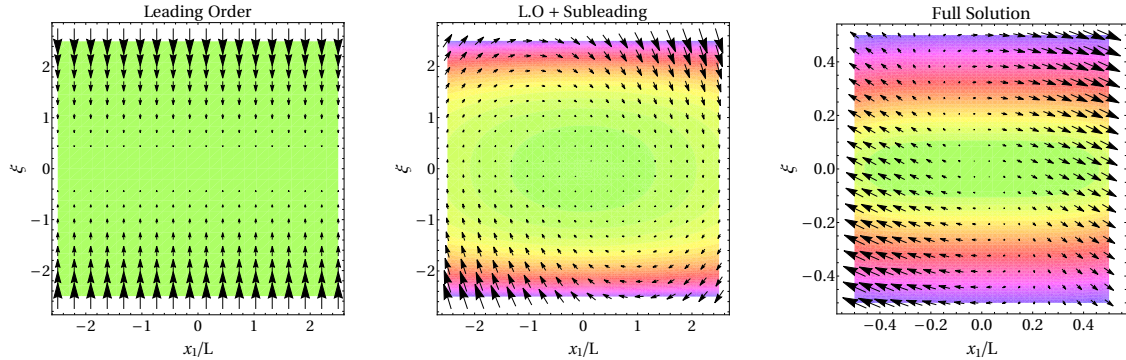


Figure 2: Flow velocity vectors  $(u'_1, u'_\xi)$  for  $\Omega = 1/2$  in the  $x_1$ - $\xi$  plane (with  $x_2 = 0$  and  $\tau/\ell = 1$ ). *Left:* LO in  $\alpha$ -expansion. *Middle:* LO + NLO in  $\alpha$ -expansion. *Right:* Full solution (middle plot in Fig. 1 zoomed in). Plots adapted from [32] where  $L$  and  $\Theta$  correspond to the AdS radius  $\ell$  and the energy scale  $T_0$  here.

To conclude, we reiterate and emphasize:

In the rotating state, the vacuum expectation value of the energy-momentum tensor of the  $\mathcal{N} = 4$  SYM theory can be separated into two components in the dual gravity theory: one associated with the dual MP BH, and the other the ambient AdS spacetime.

In the large BH limit, the component associated with the BH dominates and corresponds to that of a rigidly rotating fluid in  $\mathbb{R} \times S^3$ . If one projects this fluid to a flat spacetime, one finds a highly non-trivial fluid flow displaying non-trivial vorticity and expansion, see Fig. 1. Zooming in onto small patches of the flow, one finds that at LO in the large BH expansion (107) the fluid flow behaves as a uniformly boosted fluid solving the ideal relativistic fluid dynamic equations of motion, while the NLO correction encodes a rotation about the boost direction, see Fig. 2.

Starting from a rotating equilibrium state on a (compact) three-sphere, a stereographic projection onto (a non-compact, flat) Minkowski space leads to an analytical vortical fluid flow [36].

#### 4. Hydrodynamic and non-hydrodynamic modes of rotating plasma from quasinormal modes

In this section we collect and summarize the salient results from recent studies of QNMs of metric fluctuations in the MP BH geometry [29, 32, 33]. By holography, these QNM results encode the dispersion relations of hydrodynamic and non-hydrodynamic modes in the dual fluid. Technical details of the numerical methods developed and used are gathered in the appendices. A different holographic dual to a rotating fluid has also been constructed by boosting a static black brane in [97] and the references therein. It should be contrasted with the current work where again we emphasize that low energy fluctuations see the fluid as a boosted with boost parameter  $a$ .

##### 4.1. Basic facts about quasinormal modes

Below we briefly describe how QNMs are defined and interpreted in the context of BH spacetimes. We shall follow the discussion in [116], which is comprehensive on the subject; we refer readers to this excellent review and the references therein for details.

QNMs are characteristic dissipative oscillation of perturbations. In general, QNM frequencies are complex with the imaginary part being associated with the decay time scale of the perturbation. In the context of General Relativity, QNMs naturally appear in the analysis of linear perturbations of fixed gravitational backgrounds. In this article, we are interested, in particular, in the linearized metric perturbation  $h_{\mu\nu}$ . These perturbations obey linear second-order differential equations, which reduce to a set of linear ordinary differential equations (ODEs) with an appropriate choice of coordinates. QNMs are the eigenmodes of this system of ODEs with the appropriate boundary conditions imposed.

For perturbed BH spacetimes in classical gravity, because of the presence of an event horizon, the system is necessarily dissipative and time-asymmetric as modes fall into the BH but cannot escape from it. The associated boundary value problem is non-Hermitian with complex eigenvalues. In particular, in-going boundary condition has to be imposed on the perturbations at the horizon, while a second boundary condition fixes the normalization of the solution. Together these two boundary conditions uniquely determine a solution to the metric perturbation for all values of frequency and momentum,  $\omega$  and  $\vec{k}$ .<sup>39</sup> It should be emphasized here that we are not interested in solutions with arbitrary frequency and momentum; what we seek in a QNM problem are the eigenfrequencies,  $\omega$ , of the system for a given momentum  $\vec{k}$ .

The appropriate boundary condition to impose at the spatial infinity (boundary) of the spacetime depends on its cosmological constant. For asymptotically AdS spacetimes where the cosmological constant does not vanish, the so-called source-less (Dirichlet) boundary condition is chosen such that when expanding about the spatial boundary, the leading order solution vanishes. Schematically, metric perturbations near the AdS-boundary ( $r \rightarrow \infty$ )<sup>40</sup> can be expanded as

$$h_{\mu\nu} = \underbrace{h_{\mu\nu}^{(0)}}_{\text{source}} r^2 + \dots + \underbrace{h_{\mu\nu}^{(4)}}_{\text{vev}} r^{-2} + \dots, \quad (108)$$

where the *normalizable mode* (subleading term) is identified with the vacuum expectation value (vev) of the energy-momentum tensor in the dual field theory, i.e.  $\langle T^{\mu\nu} \rangle \sim h_{\mu\nu}^{(4)}$ , while the *non-normalizable mode* (leading term),  $h_{\mu\nu}^{(0)}$ , is identified with the source of  $T^{\mu\nu}$ ; the dots (...) indicate that other powers are generally non-zero in this expansion. The Dirichlet boundary condition to be imposed at the AdS-boundary is then

$$\lim_{r \rightarrow \infty} h_{\mu\nu}^{(0)}(r, \omega, \vec{k}) = 0, \quad (109)$$

which for each momentum  $\vec{k}$  determines the QNM values of the frequency,  $\omega(\vec{k})$ , yielding the dispersion relations of hydrodynamic and non-hydrodynamic eigenmodes of the dual field theory.

The retarded Green's function is given by the variation of the vev with respect to the source. Schematically, the retarded Green's function of the energy-momentum tensor

---

<sup>39</sup>We work in Fourier space where  $(\omega, \vec{k})$  is conjugate to  $(t, \vec{x})$ , the time and spatial coordinates. If the system is invariant under temporal and spatial translations,  $h_{\mu\nu} \propto e^{-i\omega t + i\vec{k} \cdot \vec{x}}$ , and plane waves,  $e^{i\vec{k} \cdot \vec{x}}$ , are eigenfunctions in the  $\vec{x}$ -directions.

<sup>40</sup>In four dimensions, metric perturbations have a conformal dimension of  $\Delta = 4$ , thus the difference between the source term and the vev-term in the near-boundary expansion is 4.

with itself is then given by

$$G^R \propto \langle T^{\mu\nu} T^{\rho\sigma} \rangle \propto \frac{\delta \langle T^{\mu\nu} \rangle}{\delta h_{\mu\nu}^{(0)}} \sim \frac{h_{\mu\nu}^{(4)}}{h_{\mu\nu}^{(0)}}. \quad (110)$$

As explained in [38], the metric QNMs of a BH spacetime are holographically dual to the poles of the retarded Green's function, thus we have also

$$G^R \propto \langle T^{\mu\nu} T^{\rho\sigma} \rangle \propto \frac{1}{\omega - \omega_{QNM}^{(n)}}, \quad (111)$$

where  $n = 1, 2, 3, \dots$  labels the QNMs.

What sets QNM problems apart from the typical problems involving small oscillations, such as the vibrating string, is the energy dissipation: waves can escape either to infinity or into the BH, and this precludes a normal-mode analysis. As QNMs decay exponentially with time, and cannot have existed for all times, they should be thought of as *quasistationary* states [116].

#### 4.2. Quasinormal modes dual to hydrodynamic and non-hydrodynamic modes

Central to the definition of different sectors of perturbations and their interpretation within holography is [38]. As pointed out in [38], QNMs can be categorized according to their charges under symmetry transformations. In a rotation invariant system, perturbations fall into one of three classes (scalar, vector, tensor) under  $O(2)$ -rotations around the direction of the perturbations' momentum. Consider, for example, metric perturbations  $h_{\mu\nu} \propto e^{ik_3 x_3}$  with a *linear* momentum in the  $x_3$ -direction. Then, the metric perturbations (under  $O(2)$ -rotations) carry either spin-0 (scalar sector:  $h_{tt}, h_{11}+h_{22}, h_{33}, h_{t3}, h_{rr}, h_{rt}, h_{r3}$ ), spin-1 (vector sector:  $h_{t1}, h_{t2}, h_{31}, h_{32}, h_{r1}, h_{r2}$ ), or spin-2 (tensor sector:  $h_{12}$ ), where the labels  $t, 1, 2, 3, r$  refer to the  $t, x_1, x_2, x_3, r$ -directions, respectively.

In this subsection, we provide an overview of the QNM spectrum of perturbations around (rotating five-dimensional) MP BHs along the idea of decoupling sectors outlined in the previous paragraph. However, in a rotating system on an  $S^3$  (like the MP BHs we study here), plane waves  $e^{i\vec{k}\cdot\vec{x}}$  are not a complete basis. Instead, the basis consists of Wigner-D functions  $\mathcal{D}_{\mathcal{K}\mathcal{M}}^{\mathcal{J}}$ , which are eigenfunctions<sup>41</sup> of  $S^3$ , whose eigenvalues,  $\mathcal{K}$ , under the  $W_3$  operator are  $\mathcal{K} = \mathcal{J}, \mathcal{K} = \mathcal{J} - 1$ , or  $\mathcal{K} = \mathcal{J} - 2$  as originally analyzed in [29].

This set of perturbations is sufficient to ensure that, in the limiting case, the shared spectrum matches that of a boosted Schwarzschild black brane. Reminiscent of the classification of metric fluctuations under rotations in the Schwarzschild black brane, these “sectors” are referred to as tensor, vector, and scalar sectors respectively. Given that there is a infinite parameter space one can explore, we limit our discussion to cases where the background spacetime configuration is away from the Hawking-Page phase transition which is dual to the deconfinement transition [117], and we choose the outer horizon radius such that  $T\ell > 1/2$ . Below we work in units where the AdS radius is set to unity,  $\ell = 1$ , and the QNM frequency is normalized by the outer horizon radius so that  $\nu = \omega/(2r_+)$ .

---

<sup>41</sup>Recall spatial translation invariance is broken by the rotation, so plane waves  $e^{i\vec{k}\cdot\vec{x}}$  are no longer the eigenfunctions of the symmetry operator.



#### 4.2.1. Previous quasinormal mode results for large black holes

In the present article, QNMs of rotating MP BHs with small as well as large horizon radius are examined. A previous analysis of these QNMs was focused on the large temperature or large BH limit [29]. It is so called because the dual field theory temperature,  $T$ , is proportional to the horizon radius,  $r_+$ , which was taken large; see Eq. (35). This limit was taken directly on the level of the equations of motion, Eq. (24), and is defined by

$$r \rightarrow \alpha r, \quad r_+ \rightarrow \alpha r_+, \quad \alpha \rightarrow \infty, \quad (112)$$

with

$$\omega \rightarrow \alpha 2\nu r_+/\ell, \quad \mathcal{J} \rightarrow \alpha j r_+/\ell, \quad \alpha \rightarrow \infty, \quad (113)$$

where only terms leading order in  $\alpha$  are kept in the fluctuation equations. QNM frequencies are reported in terms of the dimensionless frequency,  $\nu$ , which is a function of the dimensionless angular momentum parameter,  $j$ .

As  $\omega$  and  $\mathcal{J}$  scale with  $r_+$ , as  $r_+$  is taken large, fluctuation frequency  $\nu$  and angular momentum  $j$  are necessarily small at any finite values of  $\omega$  and  $\mathcal{J}$ . In this limit, instead of decoupling according to  $(\mathcal{J}, \mathcal{K})$ , modes decouple according to the  $\mathcal{K}$  charge of the  $\sigma$  basis, e.g. the  $\mathcal{K}$  charge of  $h_{++} \rightarrow 2$  and  $h_{3-} \rightarrow -1$ . Up to parity, this results in three sectors: tensor, scalar, and vector.<sup>42</sup> Below we reproduce figures from [29] that show the dispersion relations of hydrodynamic and low-lying non-hydrodynamic QNMs in the vector and scalar sector in the large BH limit. Note the notation used in [29] is slightly

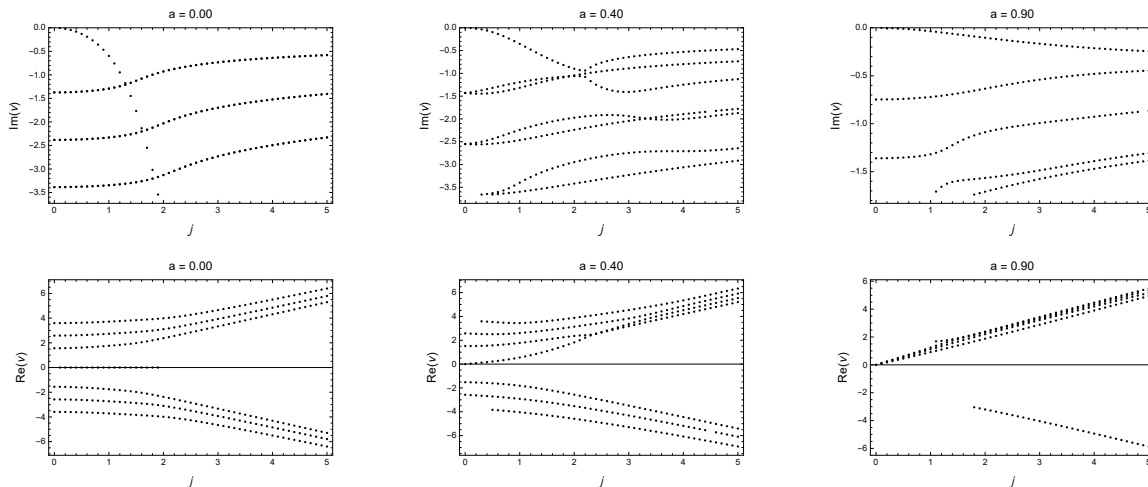


Figure 3: Vector sector dispersion relations. Displayed here are the real and imaginary parts of quasinormal frequencies of  $h_{3+}$  and  $h_{t+}$  for large BHs in case (ii) as a function of  $j$ . Modes displayed here were found with precision of at least  $d\nu = \nu 10^{-5}$ . Missing modes did not converge to sufficient precision and have been filtered out by the numerical routine.

different: in Fig. 3 and 4,  $a \equiv a/\ell$  is implicit as  $\ell = 1$ . Note also there is a sign flip in the values of  $a$  used in [29], so the real part of the QNMs found there has the opposite sign when compared to the results in this work below.

<sup>42</sup>In [29] there was a mistake in obtaining the fluctuation equations for the boosted black brane, which is referred to as case (iii) in [29]. Thus, in [29] it was not recognized that the metric fluctuation equations in the large BH limit (112) and (113) are identical to those around a boosted black brane. Already in [32] it was realized that the large BH limit leads to this identification. We stress, however, that the metric in this limit is *not* that of a boosted black brane, but that of a nontrivially rotating BH.

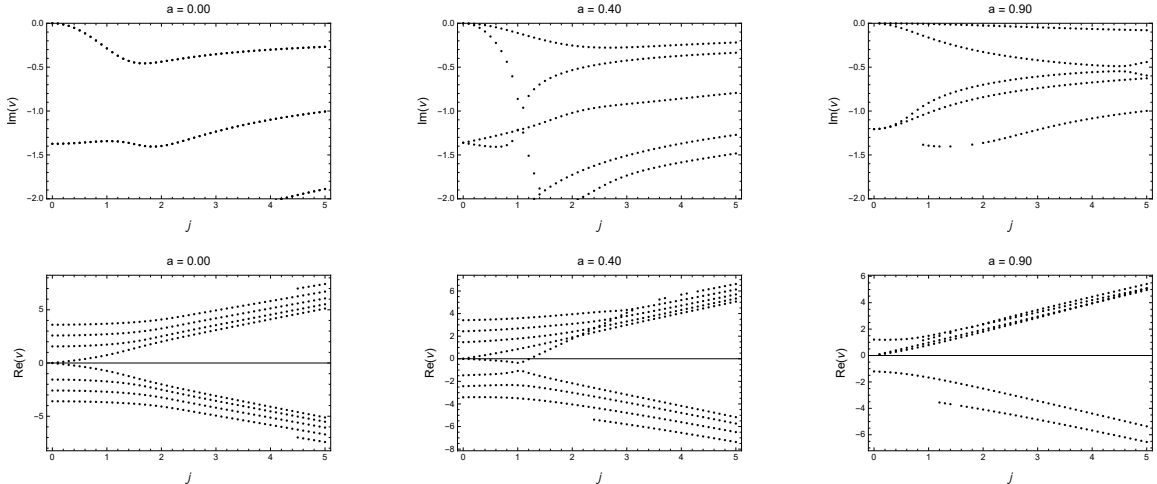


Figure 4: Scalar QNMs of the equal angular momenta BH in the large BH limit. There are two hydrodynamic modes, which we identify as sounds modes, which mirror each other regarding their real part at  $a/\ell = 0$ , and both have the same imaginary part. At  $a/\ell = 0$  these two modes behave differently. Modes displayed here were found with precision of at least  $d\nu = \nu 10^{-5}$ . Missing modes did not converge to sufficient precision and have been filtered out by the numerical routine.

To further study the role of the angular momentum parameter  $j$ , QNMs for large  $j$  were calculated in [29]. In the *eikonal limit*, which is defined by  $j \rightarrow \infty$ , a general analytic expectation for the behavior of QNM frequencies was known [118, 119]. Reproduced in Fig. 5 is the figure from [29] that shows the large BH limit tensor sector result confirming the known scaling in [118, 119].<sup>43</sup> As  $j$  is equivalent to the linear momentum  $k$  [32], the quantity  $c(k) \rightarrow c(j)$  defined in [118, 119] satisfies the predicted behavior at large values of  $j$ . The numerical results in [29] imply the following large- $j$  expansion for the  $n$ th mode:  $2\nu = 2j + c_n e^{-i(\pi/3)} (2j)^{-1/3} + O((2j)^{-1})$ , where the conjugate frequency  $-2\nu^* = -2j + c_n e^{-i(2\pi/3)} (2j)^{-1/3}$  is also included in our analysis, and  $c_n$  are real numbers in agreement with [119].<sup>44</sup> This observation further confirmed that the angular momentum  $j$  is associated with the linear momentum  $q$  from [120]. As we now know, in the large BH limit the two are related by  $j = q/(2\pi T)$ .

Summarizing the remaining results from [29], mostly the hydrodynamic behavior in large equal angular momenta five-dimensional AdS BHs was analyzed in the large BH limit (112) and (113). These are holographically dual to spinning quantum fluids. Due to the spatial anisotropy introduced by the angular momentum, hydrodynamic transport coefficients are split into groups longitudinal or transverse to the angular momentum. Since chirality is broken by the rotating background, transport also splits into being aligned or anti-aligned with that background rotation. Analytic expressions are provided for the two shear viscosities,  $\eta_{\parallel}$  and  $\eta_{\perp}$ , the longitudinal momentum diffusion coefficient,  $D_{\parallel}$ , two speeds of sound,  $v_{\pm}$ , and two sound attenuation coefficients,  $\Gamma_{\pm}$  in the momentum diffusion dispersion relation  $\nu = v_{\parallel} j - \mathcal{D}_{\parallel} j^2$  and the sound dispersion relation  $\nu = v_{s,\pm} j -$

<sup>43</sup>Again,  $\ell = 1$  is implicit here.

<sup>44</sup>In order to relate to [119], the following identifications are needed:  $\omega_F \equiv 2\nu$  and  $q_F \equiv 2j$  with subscript “F” indicating quantities in [119].

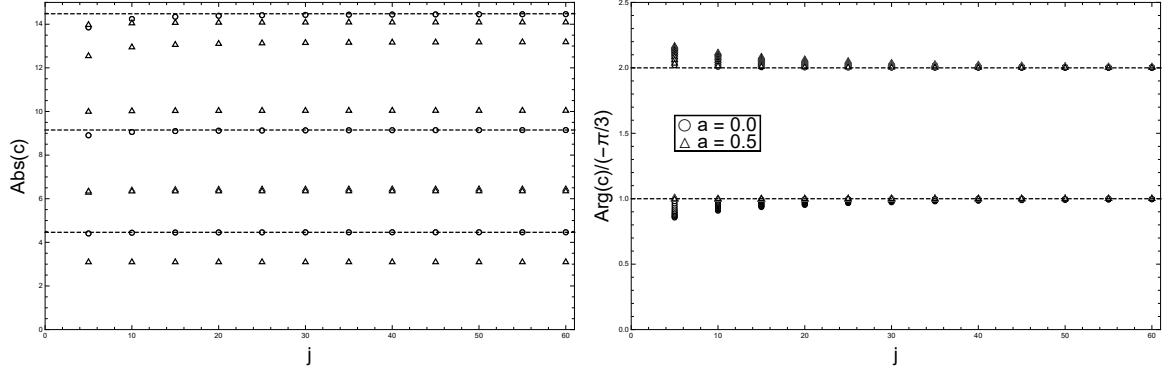


Figure 5: Large  $j$  (eikonal limit) analysis. Shown here are the quantities  $\text{Abs}(c)$  and  $\text{Arg}(c)/(-\pi/3)$ . The dashed lines are the expected values according to [118, 119]. For large  $j$ , the values at  $a/\ell = 0$  (circles) and  $a/\ell = 0.5$  (triangles) in the right plot converge to the predicted ones. In the left plot, the same is true for the case  $a/\ell = 0$  (circles). But for  $a/\ell \neq 0$  (triangles), the large  $j$  asymptotes change depending on the value of  $a/\ell$ . These plots are generated from data computed in the large BH limit.

$i\Gamma_{s,\pm} j^2$  [29]:

$$\eta_{\perp}(a) = \eta_0 \frac{1}{\sqrt{1-a^2}}, \quad (114)$$

$$\eta_{\parallel}(a) = \eta_0 \sqrt{1-a^2}, \quad (115)$$

$$v_{\parallel}(a) = a, \quad (116)$$

$$\mathcal{D}_{\parallel}(a) = (2\pi T) \mathcal{D} (1-a^2)^{3/2} = \frac{1}{2} (1-a^2)^{3/2}, \quad (117)$$

$$v_{\pm}(a) = v_0 \frac{\sqrt{3}a \pm 1}{1 \pm \frac{a}{\sqrt{3}}}, \quad (118)$$

$$\Gamma_{\pm}(a) = \Gamma_0 \frac{(1-a^2)^{3/2}}{\left(1 \pm \frac{a}{\sqrt{3}}\right)^3}, \quad (119)$$

where for the holographic ( $\mathcal{N} = 4$  SYM) fluid the quantities at vanishing angular momentum,  $a = 0$ , are given by:  $\eta_0 = N^2 \pi T_0^3 / 8$ , conformal speed of sound  $v_0 = 1/\sqrt{3}$ , and conformal sound attenuation  $\Gamma_0 = 1/3$ . Known relations between these coefficients are generalized to include dependence on angular momentum:

$$\mathcal{D}_{\parallel}(a) = 2\pi T_0 \frac{\eta_{\parallel}(a)}{\epsilon(a) + P_{\perp}(a)}, \quad (\text{Einstein relation}) \quad (120)$$

$$\Gamma_{\pm}(a) = \frac{2\eta_{\parallel}(a)}{3(\epsilon(a) + P_{\perp}(a))} \frac{1}{(1 \pm a/\sqrt{3})^3}. \quad (121)$$

The shear viscosity to entropy density ratio varies between zero and  $1/(4\pi)$ , depending on the direction of the shear. Its value can go from  $\eta_{\perp}/s = 1/(4\pi)$  when the shear is *transverse* to the direction of the fluid anisotropy, down to  $\eta_{\parallel}/s = (1-a^2)/(4\pi)$  with  $|a| < 1$  when the shear is *longitudinal* along the anisotropy direction.

Eqs. (114) to (121) are transport coefficient relations for shear transport, momentum diffusion and sound propagation in a boosted fluid, as discussed in [65, 66]. But the holographic fluid considered in this section is still a true rotating fluid—and not just a boosted one—even in the large BH limit. Only when probed by low energy fluctuations (hydrodynamic fluctuations having frequency and angular momentum small compared to the temperature, i.e.  $\nu, j \ll T$ ) in the strict large BH limit given by Eqs. (112) and (113) do their dispersion relations *look* like those of a fluid boosted with boost parameter  $a$ . This statement gets corrected at any finite horizon radius when the large BH limit is not taken (see [32]).

Mathematically, the fundamental difference between longitudinal and transverse shear viscosity can be traced to the equations of motion for the hydrodynamic modes. In the anisotropic case, the rotational symmetry is broken. This leads to the longitudinal shear perturbations (along the anisotropy direction, which is the  $x_3$ -axis in our case) transforming as vectors under rotations around the anisotropy direction. The longitudinal shear perturbations then couple to the momentum diffusion modes which also transform like vectors under such rotations. Meanwhile, the transverse shear perturbation is unaffected, retaining its transformation properties as a 2-tensor under rotations, decoupling from all other perturbations, and hence yielding a transverse shear viscosity to entropy ratio that takes the known holographic value of  $1/(4\pi)$ . This is an important general result, because it implies that in anisotropic holographic fluids—for which rotating fluids are examples—the value of shear viscosity depends on the direction and there is no lower bound on the shear to entropy ratio for the longitudinal shear viscosity. This result was first established in anisotropic holographic superfluids [121, 122] and later in an anisotropic holographic model for the pre-equilibrium stage of the QGP [123].

In anisotropic holographic fluids [121, 122, 123], which include rotating fluids, the value of shear viscosity can vary depending on the direction of the shear relative to the anisotropy [29]. There is no lower bound [124] on the shear viscosity to entropy density ratio for the longitudinal shear viscosity. The lack of a bound and the direction-dependence of the shear viscosity are both entirely based on the breaking of the rotation symmetry. Thus, both effects will have a strong impact on the QGP physics if the QGP plasma turns out to be strongly anisotropic, a case discussed for example in [125, 126, 127]. In that case, this strongly anisotropic shear viscosity should be taken into account in hydrodynamic models of the QGP.

Finally, these results furthermore demonstrate that large equal angular momenta five-dimensional MP BHs in the large BH limit are perturbatively stable for all angular momenta which we tested below extremality (which occurs at the same angular momentum  $a = \ell$  in this limit as the superradiance instabilities). Away from the large BH limit, this statement is limited by superradiance instabilities which then occur at lower values of  $a$  than extremality, as discussed in Sec. 4.2.7. Beyond the large BH limit, also the QNMs for metric fluctuations around the full rotating BH metric were considered, merely evaluated at a large value for  $r_+ = 100$ , this is referred to as “case (i)” in [29]. Qualitatively and quantitatively, the results from the large BH limit were confirmed by this computation.

One major task in the present article is to go beyond large BHs and examine intermediate to small BHs, which is mainly discussed in Sec. 4.2.6.

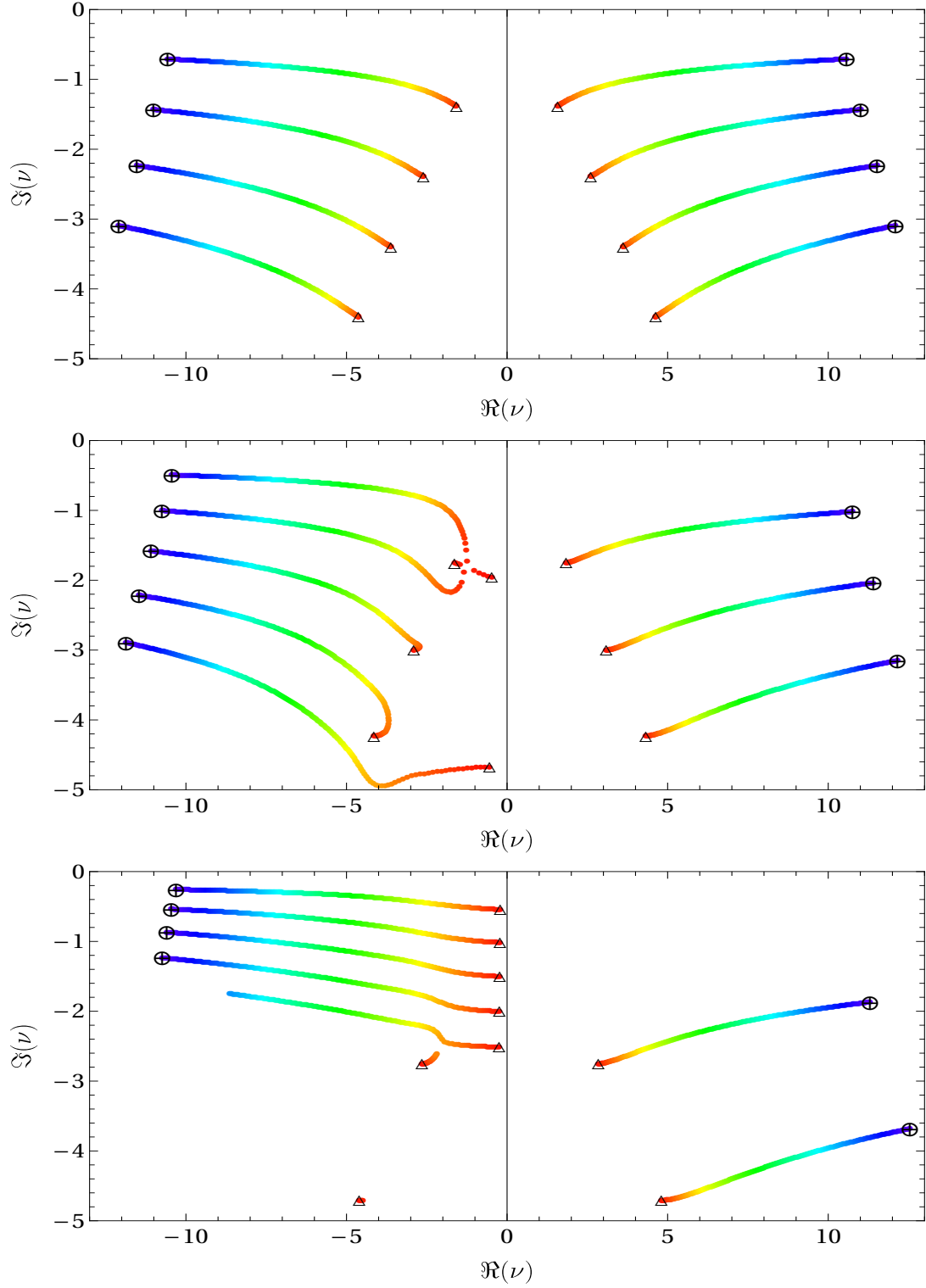


Figure 6: Scaled tensor modes,  $\nu$ , for three values of  $a/l$  at  $r_+/l = 10$ . *Top:*  $a/l = 0$ . *Middle:*  $a/l = 1/2$ . *Bottom:*  $a/l = 9/10$ . The total angular momentum of the fluctuation,  $\mathcal{J}$ , ranges from 0 to 100 in steps of  $1/2$ . Modes with  $\mathcal{J} = 0$  and 100 are marked by  $\Delta$  and  $\oplus$  respectively in the plots.

#### 4.2.2. $\mathcal{K} = \mathcal{J}$ — Tensor fluctuations

For  $\mathcal{K} = \mathcal{J}$ , the fluctuation  $h_{++}$  decouples from all other fields and hence it is a naturally gauge invariant master variable for this class of fluctuations. In Fig. 6 we display the spectrum for three different values of angular momentum per mass  $a/\ell = 0, 1/2, 9/10$ , for total angular momentum of the fluctuation  $\mathcal{J} = 0, 1/2, 1, \dots, 100$  (increasing in steps of  $1/2$ ), and horizon radius  $r_+/\ell = 10$ . In Fig. 6 (and all figures in this subsection displaying spectra) we see that for each  $\mathcal{J}$  (whose value is denoted by a particular color), there are a group of modes descending into the complex plane. It is standard in the literature (see for instance [116]) to refer to them as overtones and label them by the index  $n$ . The lowest mode has an imaginary part that is smallest in magnitude, and is called the  $n = 0$  or fundamental tone. It is thus the longest lived and the dominant mode in the BH ringdown. As an example, the top plot of Fig. 6 displays the overtones  $n = 0, 1, 2, 3$ .

From Fig. 6 it is immediately clear that there is no mode with frequency  $\nu$  for which  $\lim_{\mathcal{J} \rightarrow 0} \nu = 0$ , and hence there are no “hydrodynamic” modes in the tensor sector. This is quite remarkable as the  $h_{++}$  fluctuation couples to other fluctuations at nonzero  $a$ .

At  $a/\ell = 0$  the modes are mirror symmetric about the imaginary axis. This is due to the time reversal invariance in the background geometry present when  $a/\ell = 0$ , but broken by the angular momentum when  $a/\ell \neq 0$ , which then separates modes into those rotating with and against the BH/fluid. Indeed, as  $a/\ell$  becomes positive definite and increases towards one, the trajectories of modes as  $\mathcal{J}$  varies move down and further apart for  $\Re(\nu) > 0$ , but they move up and closer together for  $\Re(\nu) < 0$ . Furthermore, QNMs from deep down in the  $\Im(\nu) < 0$  complex half plane are pushed up vertically towards  $\Im(\nu) = 0$ , moving up like a “bowl of a spoon” that then joins up with the “handle of the spoon” provided by the  $\mathcal{J}$ -trajectory of each successively higher mode. This behavior as  $a/\ell$  increases resembles that of the purely imaginary QNMs in the Reissner-Nordström BH as the charge is pushed towards extremality [128].

To show in more detail how the QNM spectrum changes in the tensor sector, and in particular this movement of QNMs coming up from the deep of the  $\Im(\nu) < 0$  complex half plane as  $a/\ell$  changes, we display in the top of Fig. 7 the spectrum for  $a/\ell \in [0.30, 0.34]$  in steps of  $\Delta a/\ell = 0.001$ . We see from the inset a behavior that looks like “level touching”, which is quite remarkable as  $\mathcal{J}$  is discrete here: first a spoon is formed with the  $\mathcal{J}$ -trajectory of a lower mode, but as the bowl of the spoon is pushed up with increasing  $a/\ell$ , at some point the “neck of the spoon” curls up so much it breaks off and a new spoon is formed with the upper mode. This “spoon formation” continues as  $a/\ell$  is increased to ever higher values until there is a spoon for each of the modes, starting with the highest. A snapshot of the spoon forming process in the early and late stages are shown in the bottom of Fig. 7 and Fig. 6 respectively. An animated GIF showing the this process in real time is also provided in the supplementary material.

Another feature to note from Figs. 6 and 7 is that as  $a/\ell$  increases and the spoons form, the  $\mathcal{J} = 0$  mode approaches the imaginary axis. This behavior is perhaps not surprising as a branch cut is expected to form when linear differential equations contain essential singularities<sup>45</sup>, and this can only happen if modes can come back onto the imaginary axis and coalesce.

<sup>45</sup>For a general discussion see [129], while specific examples of this in the fluctuations around Reissner-Nordström BHs can be found in [130, 131].

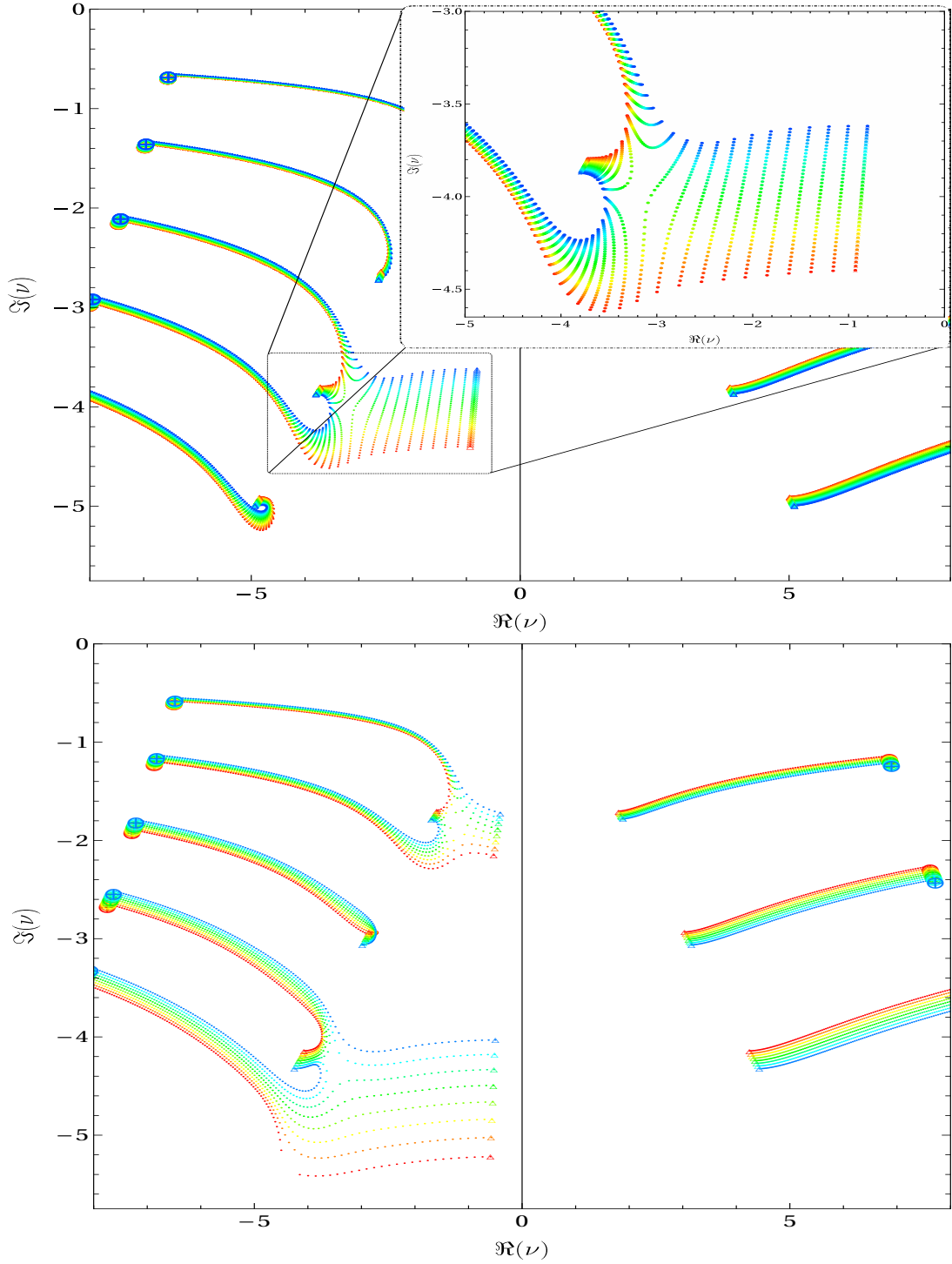


Figure 7: Scaled tensor modes,  $\nu$ , for two different ranges of  $a/l$  at  $r_+/l = 10$ .  $\mathcal{J}$  ranges from 0 to 60 here in steps of  $1/2$ . Modes with  $\mathcal{J} = 0$  and 60 are marked by  $\Delta$  and  $\oplus$  respectively in the plots. *Top:*  $a/l \in [0.3, 0.34]$  in steps of  $\Delta a/l = 0.001$ . *Bottom:*  $a/l \in [0.47, 0.54]$  in steps of  $\Delta a/l = 0.01$ . Colors denote the different values of  $a/l$ : **red** corresponds to the minimum value of the  $a/l$  in the range, **blue** the maximum. The inset of the top image zooms in on the region containing the dovetailing behavior. An animated GIF showing this in real time is included in the supplementary material.

#### 4.2.3. $\mathcal{K} = \mathcal{J} - 1$ — Vector fluctuations

From the ansatz given in Eq. (60) one can see that for the choice of  $\mathcal{K} = \mathcal{J} - 1$  the modes  $h_{+t}$ ,  $h_{+3}$ , and  $h_{++}$  couple together. This occurs for all modes for which  $\mathcal{K} < \mathcal{J}$ , and all modes for  $\mathcal{K} \in [n, \mathcal{J}]$  will couple. In Fig. 8 we display the spectrum for three different values of angular momentum per mass  $a/\ell = 0, 1/2, 9/10$ , for total angular momentum of the fluctuation  $\mathcal{J} = 0, 1/2, 1, \dots, 100$  (increasing in steps of  $1/2$ ), and horizon radius  $r_+/\ell = 10$ .

Like in the tensor sector, the trajectories of modes are mirror symmetric about the imaginary axis at  $a/\ell = 0$ , but once  $a/\ell \neq 0$  this symmetry (due to time reversal invariance) is broken by the angular momentum, and the  $\Re(\nu) > 0$  trajectories are pushed down relative to the  $\Re(\nu) < 0$  ones.

Unlike the tensor sector though, there does exist a mode  $\nu$  for which  $\lim_{\mathcal{J} \rightarrow 0} \nu = 0$  and hence a potential hydrodynamic mode in this sector. At  $a/\ell = 0$ , this is the expected shear diffusion mode residing on the imaginary axis. Furthermore, we observe at  $a/\ell = 0$  each non-hydrodynamic QNM splits into two trajectories, one for  $\mathcal{K} = \mathcal{J}$  and the other  $\mathcal{K} = \mathcal{J} - 1$ .

As  $a/\ell$  becomes positive definite and increases, we see from Fig. 8 again this behavior of QNMs deep down in the  $\Im(\nu) < 0$  complex half plane being pushed up and forming spoons with the  $\mathcal{J}$ -trajectories of the vector modes. What is interesting here is that as the QNMs move up for  $a/\ell > 0$ , the two branches previously joined at  $\mathcal{J} = 0$  when  $a/\ell = 0$  split open to form spoons. Even more so is that not only is there “level touching” seen in the middle of Fig. 8 when  $a/\ell = 1/2$ , there is also “level crossing” seen in the bottom of Fig. 8 when  $a/\ell = 9/10$ . As  $a/\ell$  approaches one, we see again the  $\mathcal{J} = 0$  modes approaching the imaginary axis as seen in the tensor sector.

At  $a/\ell = 0$ , the spectrum contains, in addition to the expected vector modes, also an almost exact copy of the tensor modes from Fig. 6. This is perhaps surprising given that the fields  $h_{++}$ ,  $h_{+t}$ , and  $h_{+3}$  all couple together and the QNMs frequencies of  $h_{++}$  are expected to be modified by this coupling compared to the tensor case discussed above. However, away from  $a/\ell = 0$  one observes strong effects from the coupling of modes, as discussed above, there is a level crossing between modes formerly from the tensor sector and those from the vector sector. Furthermore, additional modes from the tensor sector continue to appear in the vector sector, although they are no longer a copy of the modes found for  $\mathcal{K} = \mathcal{J}$ .

#### 4.2.4. $\mathcal{K} = \mathcal{J} - 2$ — Scalar fluctuations

As discussed in the beginning of Sec.4.2.3, lowering the eigenvalue of the operator  $W_3$  couples fields to all higher  $W_3$  eigenfunctions. Thus choosing  $\mathcal{K} = \mathcal{J} - 2$  introduces four additional fields  $h_{33}$ ,  $h_{tt}$ ,  $h_{t3}$ , and  $h_{+-}$ , which couple to  $h_{+t}$ ,  $h_{+3}$ , and  $h_{++}$ . In Fig. 9 we display the spectrum for three different values of angular momentum per mass  $a/\ell = 0, 1/2, 9/10$ , for total angular momentum of the fluctuation  $\mathcal{J} = 0, 1/2, 1, \dots, 100$  (increasing in steps of  $1/2$ ), and horizon radius  $r_+/\ell = 10$ .

Like in the vector sector, there is also a mode  $\nu$  for which  $\lim_{\mathcal{J} \rightarrow 0} \nu = 0$ , and so a potential hydrodynamic mode in the scalar sector. In addition, at  $a/\ell = 0$  the spectrum contains an almost exact copy of both the tensor and vector spectra. As a result, the scalar sector contains three hydrodynamic modes: two are sound modes new in this sector, and one corresponds to the diffusion mode encountered in the vector sector discussed above. For  $a/\ell > 0$ , we see again the diffusion mode shifts away from the imaginary axis with an increasingly large negative real part for increasing  $\mathcal{J}$ .



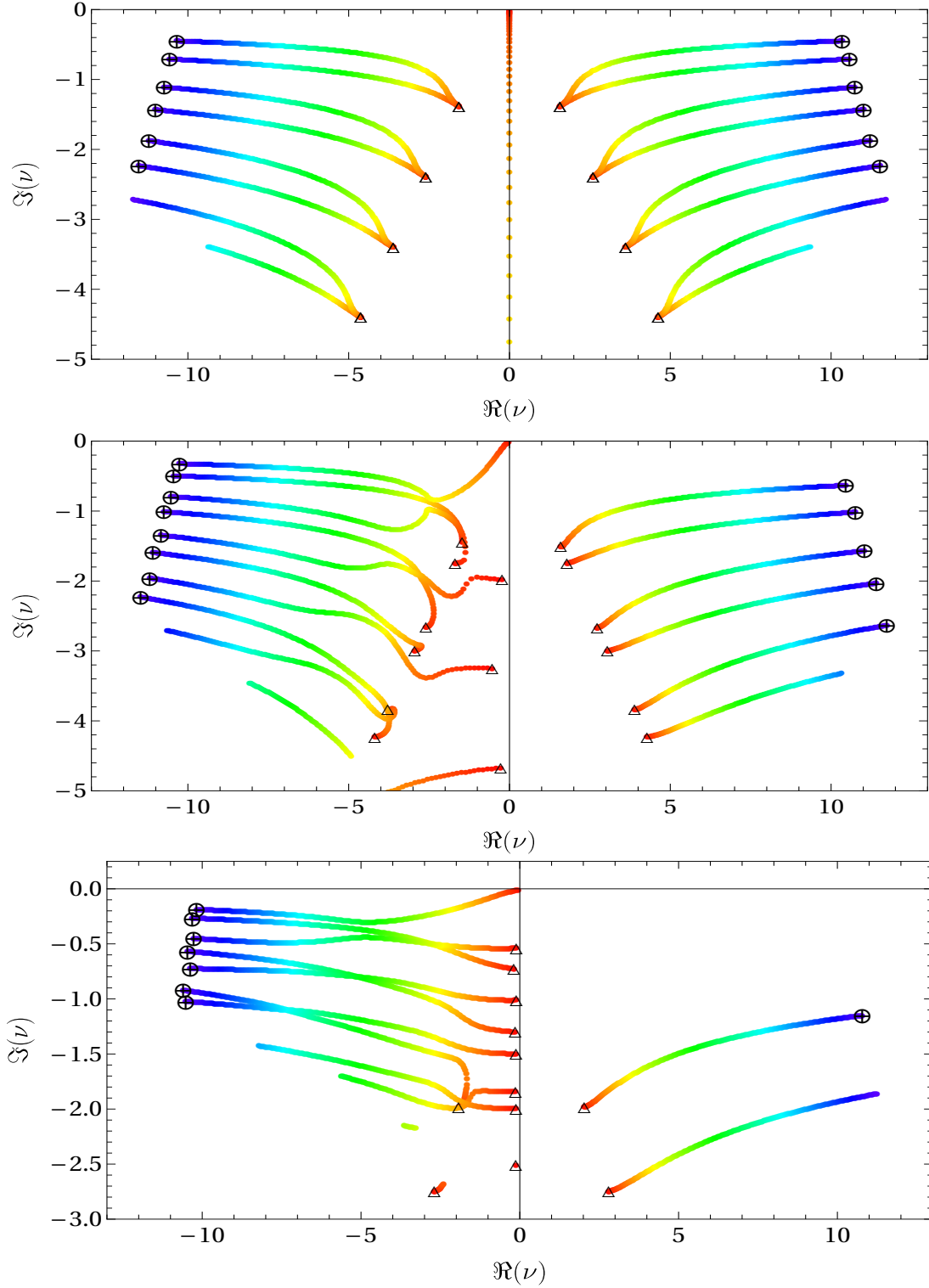


Figure 8: Scaled vector modes,  $\nu$ , for three values of  $a/\ell$  at  $r_+/\ell = 10$ . *Top:*  $a/\ell = 0$ . *Middle:*  $a/\ell = 1/2$ . *Bottom:*  $a/\ell = 9/10$ . The total angular momentum of the fluctuation,  $\mathcal{J}$ , ranges from 0 to 100 in steps of  $1/2$ . Modes with  $\mathcal{J} = 0$  and 100 are marked by  $\Delta$  and  $\oplus$  respectively in the plots.

Also like in the vector sector, the coupling of the fields in the scalar sector at  $a/\ell = 0$  leads to bands of non-hydrodynamic QNM modes degenerate at  $\mathcal{J} = 0$ , but split up for  $\mathcal{J} > 0$ . While there are only bands of two modes in the vector sector, this is enhanced to bands of three in the scalar sector, one for each of the possibilities:  $\mathcal{K} = \mathcal{J}, \mathcal{J} - 1, \mathcal{J} - 2$ . While  $\mathcal{J} > 0$  lifts the degeneracy at  $a/\ell = 0$ , this is automatically lifted for  $a/\ell > 0$ . Indeed, this “split open” of the bands at  $\mathcal{J} > 0$  when  $a/\ell > 0$  happens as QNMs deep down in the  $\Im(\nu) < 0$  complex half plane move up and form spoons with the  $\mathcal{J}$ -trajectories of the scalar modes.

Analogous to the vector sector, we see again the “level crossing” behavior in Fig. 9 as the spoons form with increasing  $a/\ell$ . As the spoons are locked into place for each of the mode trajectories displayed (starting from the highest), the  $\mathcal{J} = 0$  modes again approach the imaginary axis as  $a/\ell$  approaches one.

#### 4.2.5. Cross sector spectrum comparison

For  $\mathcal{J} \geq 2$  there is non-trivial coupling in tensor fields in the vector sector equation of motion and tensor/vector fields in the scalar sector. Non-trivial coupling means, that despite enhanced  $U(2)$  angular symmetry, linearized field equations do not couple cleanly by component. It is thus interesting to compare the spectra of the tensor, scalar, and vector sector to each other. Graphically, this has been done in Fig. 10. The first observation is, for  $a = 0$ , the tensor spectrum appears in the spectra of the vector and scalar sectors. Similarly, the vector spectrum appears in the scalar spectrum. This points to the fact that for  $a = 0$ , the full spherical symmetry of the spacetime is restored, and the tensor, vector, and scalar fields decouple from each other for all  $\mathcal{J}$  and  $\mathcal{K}$ . A similar decoupling was seen in the large temperature [29] limit as defined in Sec. 4.2.1. The second observation is that the once degenerate modes of the  $a = 0$  split in the  $a \neq 0$  case, as seen in the second plot of Fig. 10. Because the splitting occurs for  $a \neq 0$  and for finite  $r_+$ , it is reasonable to conclude that curvature scale associated with the spherical geometry of the BH causes this.

#### 4.2.6. Horizon radius dependence & the emergence of hydrodynamics

In all previous subsections of this section (except Sec. 4.2.1), the horizon radius was chosen to be  $r_+ = 10$  (in units of the AdS radius,  $\ell = 1$ ). In this subsection, we discuss how different values of the horizon radius influence the QNM spectra. Recall that the horizon radius corresponds to the temperature of the rotating fluid by Eq. (35). In particular, in the large BH limit (F.5), the dispersion relations of the lowest gapless QNMs display the hydrodynamic behavior expected for  $\mathcal{N} = 4$  SYM theory in a boosted fluid state, and the temperature is proportional to the horizon radius,  $T = r_+ \sqrt{\ell^2 - a^2} / (\pi \ell^3)$ .

In order to study the dispersion relations of the lowest gapless modes, we choose the momentum diffusion sector as an example. Dispersion relations of the lowest gapless QNM in that channel have been computed for various values of the horizon radius from  $r_+ = 10$  to  $r_+ = 10^7$ . The momentum of the mode has been chosen in half-integer steps  $\mathcal{J} = 0, 1/2, 1, \dots, \mathcal{J}_{max}$  up to a maximal value of  $\mathcal{J} = \mathcal{J}_{max}$ , which is determined by the relation  $\mathcal{J}_{max}/r_+ = j_{max} = 0.1$ .<sup>46</sup> These values will be used as data points that will be fitted to the expected form of the hydrodynamic dispersion relation below. It is important to note that with this definition of a fit window for the momentum  $0 < j \leq j_{max}$ , there are fewer data points to fit at small  $r_+$  than at larger  $r_+$ . This is because  $j = \mathcal{J}/r_+$ ,

---

<sup>46</sup>This value of  $j$  is well within the radius of convergence indicated by  $R_c$  as shown in [32]

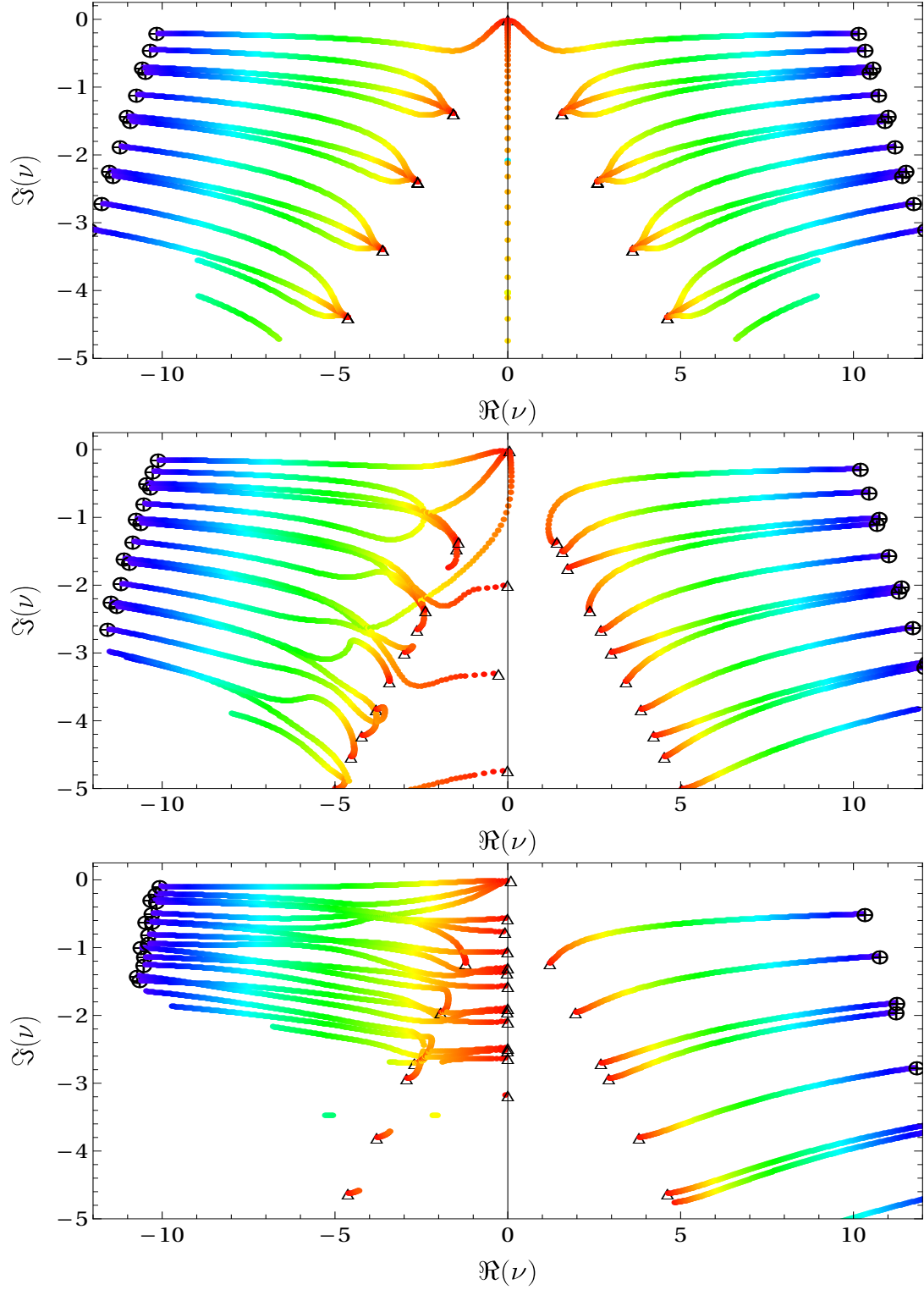


Figure 9: Scaled scalar modes,  $\nu$ , for three values of  $a/\ell$  at  $r_+/\ell = 10$ . *Top:*  $a/\ell = 0$ . *Middle:*  $a/\ell = 1/2$ . *Bottom:*  $a/\ell = 9/10$ . The total angular momentum of the fluctuation,  $\mathcal{J}$ , ranges from 0 to 100 in steps of  $1/2$ . Modes with  $\mathcal{J} = 0$  and 100 are marked by  $\Delta$  and  $\oplus$  respectively in the plots.

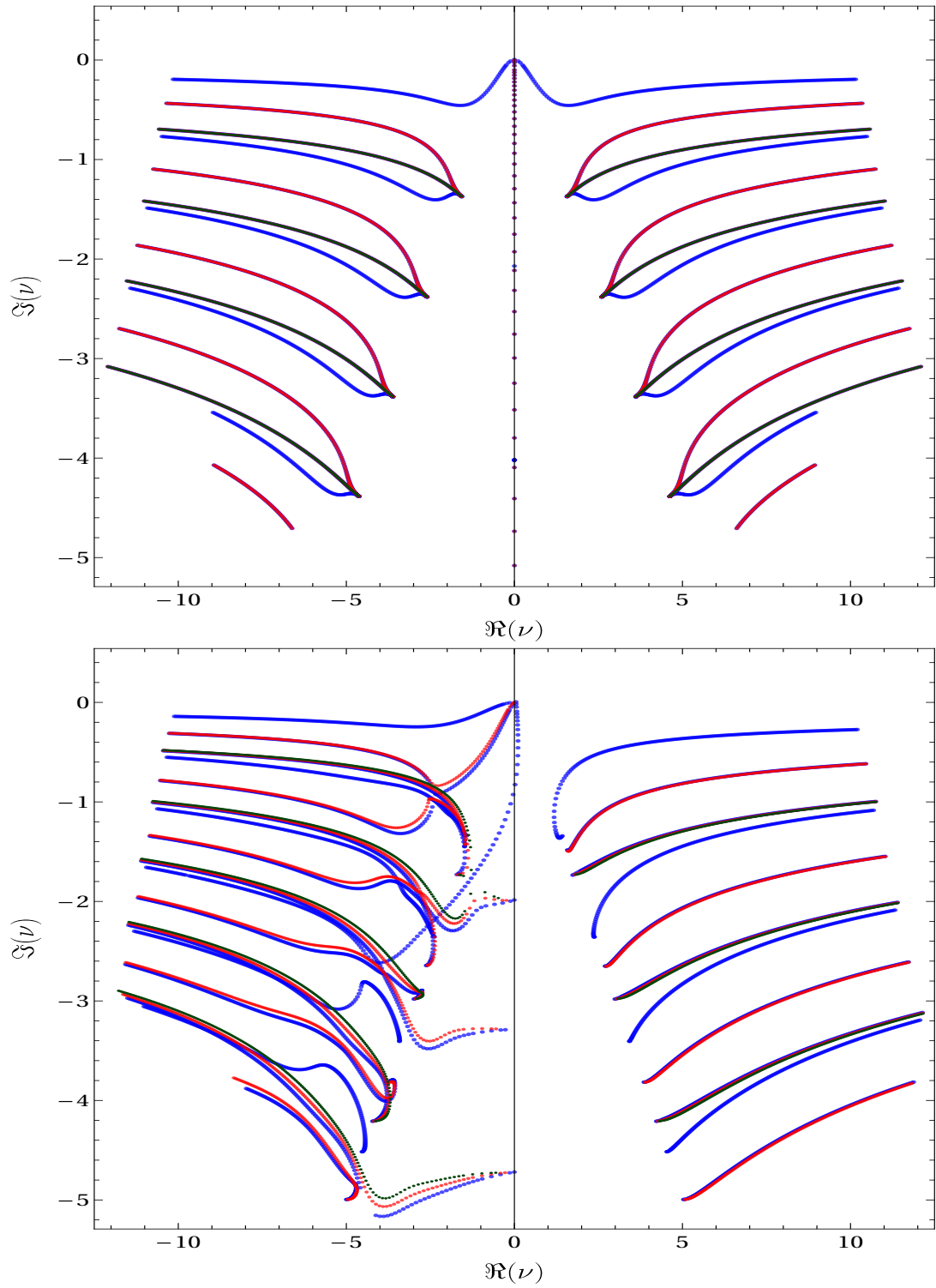


Figure 10: Combined spectra of the sectors considered in sections 4.2.2-4.2.4 at  $r_+/l = 10$ . The green depicts the tensor sector, red the vector sector, and blue the scalar sector. The modes are plotted for total angular momentum of the fluctuation,  $\mathcal{J}$ , ranging from 0 to 100 in steps of  $1/2$ . *Top:*  $a/l = 0$ . *Bottom:*  $a/l = 1/2$ .

where  $\mathcal{J}$  takes discrete values. This introduces an increasing systematic error for this fit at decreasing  $r_+$ .

Now this QNM data is fitted to the dispersion relation:

$$\omega = v\mathcal{J}^\beta - iD\mathcal{J}^\alpha, \quad (122)$$

where we expect a diffusion mode of  $\mathcal{N} = 4$  SYM theory at rest ( $a = 0$ ) to take the values  $\alpha = 2$ ,  $\beta = 1$ ,  $v = 0$ ,  $D = 1/(\pi T) = 1/r_+$ . Here,  $D$  is related to the coefficient defined in [120] by  $\mathcal{D} = D/4$ . The result of this fit is shown in Fig. 11. This figure shows that in the fit window  $\mathcal{J}/r_+ \leq j_{max} = 0.1$  the expected diffusion scaling  $\alpha = 2$  occurs for  $r_+ \approx 1000$  while the linear velocity term scaling  $\beta = 1$  occurs already at much smaller radii  $r_+ \approx 10$ . For larger values of  $a$ , these integer scaling values  $\alpha = 2$ ,  $\beta = 1$  are reached at larger  $r_+$  values.

As pointed out in Appendix E, for a boosted fluid with boost velocity  $a$  one expects  $r_+D = (1-a^2)^{3/2}$  and  $v = 2a$  [65, 66, 29].<sup>47</sup> As seen in Fig. 11, these values are approached at large horizon radius  $r_+ \approx 10^6$  for the diffusion coefficient  $r_+D$ , but already at small radii  $r_+ \approx 10$  for the propagation speed  $v$  of this former diffusion mode.

Finally, we point out two distinct features displayed in Fig. 11 as the horizon radius (and thus the temperature in the dual field theory) are increased:

- The temperature  $T$  becomes the largest scale in the system, therefore the hydrodynamic approximation becomes more applicable.
- For fluctuations at a fixed energy  $\omega$ , increasing the horizon radius leads to the large BH limit given by eqs. (112) and (113), and such fluctuations become hydrodynamic ( $\omega, j \ll T$ ). This occurs as these fluctuations see less and less of the rotating fluid and perceive it rather as a boosted fluid with boost velocity  $a$ .

In the case of the strict large rotating BH limit (applying eqs. (112) and (113), keeping only the leading order in scaling coefficient  $\alpha$ ), the metric given in Eq. (57) simplifies slightly. But it retains the topology  $S^3 \times \mathbb{R}$ , and remains in a rotating state with nonvanishing angular momentum. In particular, it does *not* simplify to a boosted black brane, and the dual fluid is *not* merely a boosted fluid, but a *nontrivially rotating fluid*. If one now chooses to probe this slightly simplified rotating background metric with metric fluctuations having *small frequency and momentum compared to the horizon radius* (i.e. hydrodynamic fluctuations), then these fluctuations effectively *see* a boosted black brane metric. This is explicitly seen in the equations of motion obeyed by the metric fluctuations around the rotating background metric in the large BH limit given by eqs. (112) and (113), which we have shown to be identical to those of the metric fluctuations around a boosted black brane with boost parameter  $a$ .<sup>48</sup>

**Summary:** While there are gapless QNMs of rotating BHs at any value of the angular momentum parameter  $a$ , these modes apparently only start following hydrodynamic dispersion relations with integer powers (e.g.  $\omega = v\mathcal{J} - iD\mathcal{J}^2 + \mathcal{O}(3)$ ) at larger values

<sup>47</sup>Note, that here the “speed”  $v$  is defined in such a way that it can take on the value 2 as a maximum. It would be better to refer to  $v$  as “double-speed”, or to redefine  $\bar{v} = v/2$  and  $\bar{\mathcal{J}} = 2\mathcal{J}$ . The physical speed of the mode is  $v/2$ . However, we retain this notation here in favor of clear relations with previous papers.

<sup>48</sup>This had not been recognized in the originally published version of [29], which is to be updated shortly.

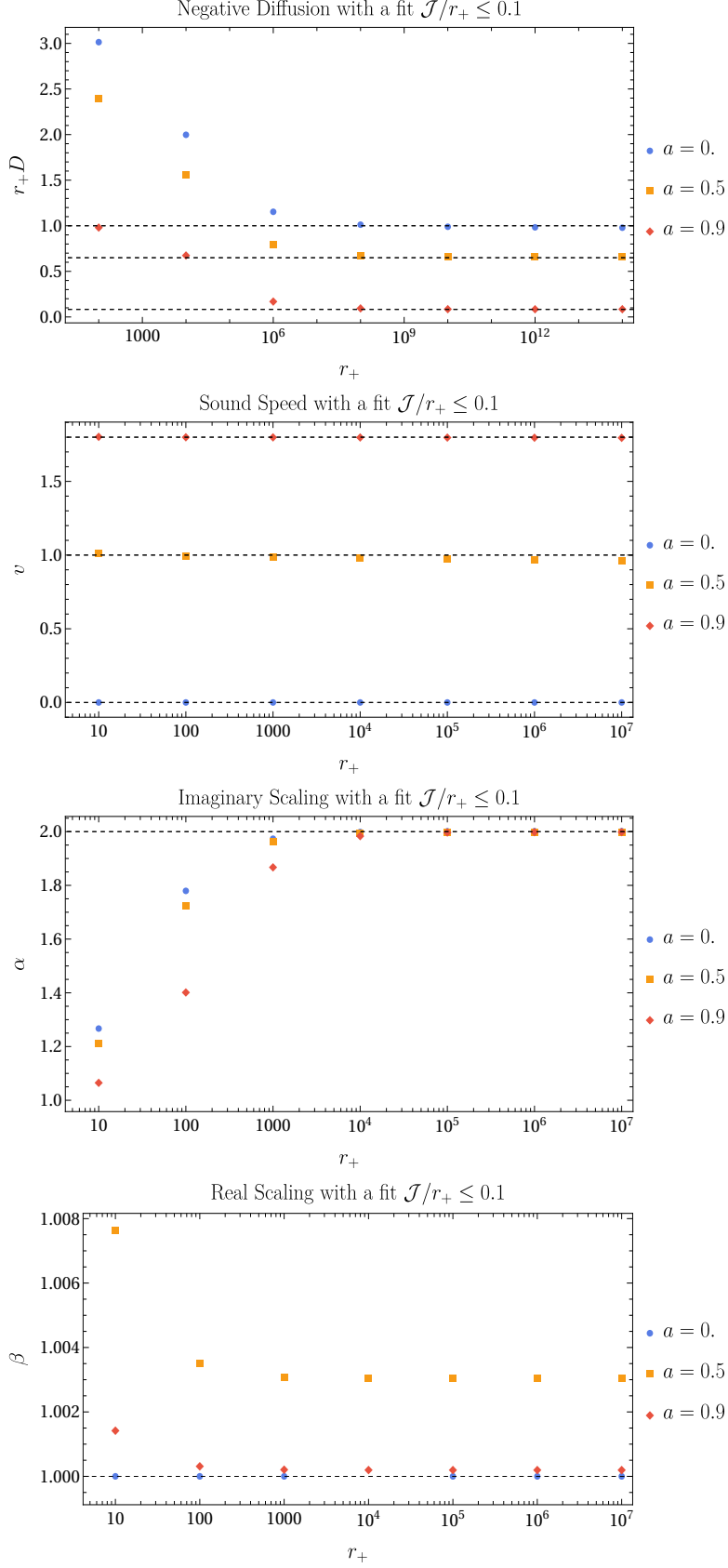


Figure 11: Horizon radius dependence & emergence of hydrodynamic scaling. The dashed horizontal lines indicate the values of diffusion coefficient  $r_+ D = r_+ \mathcal{D}/4$  and “diffusion speed”  $v$  expected for a fluid boosted with velocity  $a = 0, 0.5, 0.9$  (taken from Table E.10 derived in appendix Appendix E). Note that this  $v$  can take a maximum value of 2 as a result of our notation, the physical speed of this mode, however, is  $v/2 \leq 1$ , which is always subluminal. Dashed horizontal lines at  $\alpha = 2$  and  $\beta = 1$  indicate the expected hydrodynamic dispersion scaling (linear propagation  $\propto \mathcal{J}$ , quadratic damping  $\propto -i\mathcal{J}^2$ ).

of the horizon radius  $r_+ \approx 1000$ . This may merely be due to the growing systematic error in the fit window  $0 \leq \mathcal{J}/r_+ \leq 0.1$  at small  $r_+$ , as discussed above, or due to the discreteness of the momentum in principle. It is remarkable that the mode at  $r_+ = 1000$  scales hydrodynamically as  $\alpha \approx 1$ ,  $\beta \approx 2$ , but the diffusion coefficient has not yet taken the value expected for a boosted fluid: that value is reached only at very large horizon values  $r_+ > 10^6$ .<sup>49</sup>

There is thus an interesting window of horizon values (which corresponds, via Eq. (35), to a window of temperatures),  $1000 \lesssim r_+ < 10^7$ , in which these holographic rotating fluids display hydrodynamic behavior that is distinct from a boosted fluid. In this window, we expect to see hydrodynamic transport coefficients being changed as a result of rotation (and not only a boost); see Fig. 11.

In [32] the convergence radius of the hydrodynamic expansion in momentum space is computed for a range of horizon radii,  $100 \leq r_+ \leq 10^6$ , overlapping with the window in which we expect hydrodynamic scaling with nontrivially modified transport coefficients due to rotation, see Fig. 13.

#### 4.2.7. Perturbative instabilities: superradiant and Gregory-Laflamme

It was first found by [24] that the equal angular momenta five-dimensional AdS BH suffered from a linear superradiant instability. This instability is caused by the presence of the conformal boundary in combination with the Penrose process. It was found in [24] that modes of high enough  $\mathcal{J}$  would induce such an instability. It is still an open question what is the final state of such an unstable system.

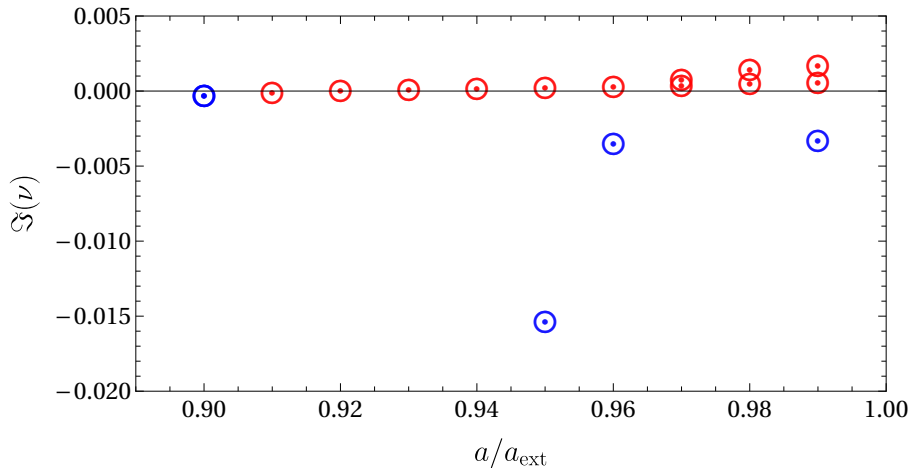


Figure 12:  $\Im(\nu)$  vs  $a/a_{\text{ext}}$  in the tensor sector for  $a \lesssim a_{\text{ext}}$ ,  $r_+ = \ell$ , and  $\mathcal{J} = 5$ . The red points indicate unstable modes, while the blue points mark stable modes.

<sup>49</sup>We note that the dispersion relations analyzed in a regime around  $r_+ \approx 10$  may also be described by a derivative expansion. In this regime, there are less numerical data points available for the fit in the window  $0 \leq \mathcal{J}/r_+ \leq 0.1$ . Thus the fit values  $\alpha, \beta, D, v$  displayed for  $r_+ = 10$  in Fig. 11 have a large systematic error. Thus, hydrodynamic scaling  $\alpha = 2$ ,  $\beta = 1$  may persist to these small horizon values. Alternatively, in that regime there may be a scaling with non-integer exponents  $\alpha$  and  $\beta$ ; for examples of such a behavior see [132, 133].

Several meta-stable states have been found [134, 135, 136, 137, 31]. Such states have an angular momentum but bear neither  $U(1)$  axial nor time translational symmetry. Instead, what is present is a helical symmetry that is a combination of the time translation and axial rotation. In Figs. 6, 8, and 9, the modes to the left of the imaginary axis approach the real axis as  $a$  and  $\mathcal{J}$  are increased. For a large enough but non-extremal  $a$  and  $J$ , these modes cross the imaginary axis. For example, in the tensor sector, for  $r_+/\ell = 1$ ,  $\mathcal{J} = 5$ , and  $a/a_{\text{ext}} = 91/100$  there is an unstable mode with a frequency of  $\nu \approx -15.56 + i0.00004541$ . This behavior of modes can further be seen in Fig. 12. It was shown in [24] that superradiant modes occur when

$$a_{\text{unstable}} = \frac{r_+^2/\ell}{1 + r_+^2/\ell^2} < a < a_{\text{ext}} = \frac{r_+^2/\ell}{1 + r_+^2/\ell^2} \sqrt{1 + \frac{\ell^2}{2r_+^2}}. \quad (123)$$

In the regime of large  $r_+$  and thus large temperature,  $a_{\text{unstable}}$  and  $a_{\text{ext}}$  would coincide as  $r_+ \rightarrow \infty$ . The reason behind such an instability is similar to Cherenkov radiation. The constant time-directed vector field

$$v_t := \partial_t - 2a \left( \frac{1 + r_+^2/\ell^2}{r_+^2} \right) \partial_\psi \quad (124)$$

measures the angular velocity of the horizon up to an overall constant normalization. For values of  $a$  in the superradiant regime, this timelike vector cannot be normalized such that it remains timelike at the AdS boundary. Rather, it becomes spacelike, and perturbations of the BH can be dragged faster than the local speed of light, thus leading to an instability.

### 4.3. Critical points

In this section we give an overview of the recent work [32], whose goal was to study the behavior of bounds on the convergence of linearized hydrodynamic expansions when the fluid is in a rotating state. Taking the MP geometry in Eq. (31) as a concrete example, such bound for  $\mathcal{N} = 4$  SYM theory in a rotating state was found in [32] by calculating critical points (as introduced in [39]).

#### 4.3.1. Implicit functions and their series expansions

As discussed in [39], a relativistic fluid supports, in general, collective excitations – linearized fluctuations of energy and momentum – around its equilibrium state, and these are referred to as hydrodynamic modes. The frequency of these modes  $\omega$  are related to the momentum via a dispersion relation which takes the form,

$$\omega(\mathbf{q}) = \sum_{c=0}^{\infty} d_n \mathbf{q}^{c/m}, \quad (125)$$

where  $\mathbf{q}$  is the wave vector,  $d \in \mathbb{C}$ , and  $m \in \mathbb{N}$ . The number of terms in the series is significant as it indicates the number of terms kept in the derivative expansion. Indeed, the series representation of the dispersion relation  $\omega(\mathbf{q})$  truncates when the hydrodynamics is considered up to a certain finite order, and it is infinite only when hydrodynamic expansion to all orders is considered. The coefficients of the series can naturally be matched to the transport coefficients at each order.

It is important to understand how dispersion relations such as Eq. (125) arise. One begins by linearizing around an equilibrium state ( $T_{\mu\nu} + \delta T_{\mu\nu}$ ) and making a choice of



the hydrodynamic degrees of freedom. The derivative expansion is then contained in the constitutive relations: e.g. by expressing the spatial stress in terms of the energy and momentum density, these relations then contain up to  $k$  derivatives of the energy and momentum density and so correspond to  $k$ -th order hydrodynamics. The resulting linear system, when expressed in terms of Fourier modes proportional to  $\exp(-i\omega t + i\mathbf{q} \cdot \mathbf{x})$ , contains non-trivial solutions provided its determinant vanishes. This determinant defines a non-trivial polynomial in  $\omega$  and  $\mathbf{q}$  and thus a complex algebraic curve for general  $(\omega, \mathbf{q}) \in \mathbb{C}^2$ , and may hence be regarded as an implicit function with the form  $F(\mathbf{q}, \omega) = 0$ .

Given that we can construct this implicit function, we are now in a position to borrow some basic results from the theory of algebraic curves. Consider an implicit function  $f(x, y) = 0$  defining a curve. Points on the curve can be classified by how it intersects with a line  $L$ . Following [138], by choosing a point  $p_0 = (x_0, y_0)$  on the curve the line  $L$  can be parametrized by  $(x_0 + \lambda t, y_0 + \mu t)$ . Intersections of the line with the curve are then roots of

$$f(x_0 + \lambda t, y_0 + \mu t) = 0. \quad (126)$$

Taylor expanding this expression around  $t = 0$  leads to the following equation for the intersection

$$(\partial_x f \lambda + \partial_y f \mu)t + \frac{1}{2}(\partial_x^2 f \lambda^2 + 2\partial_{xy}^2 f \lambda \mu + \partial_y^2 f \mu^2)t^2 + \dots = 0, \quad (127)$$

from which we can classify the number of intersections of the line and the curve.

*Single intersections:* Consider first the term linear in  $t$ ,  $df/dt|_{t=0}$ . If either or both of the partial derivatives are non-zero, then every line through  $p_0$  has a single intersection with the curve. There is however an exception: it is possible that  $\mu/\lambda$  takes a value such that  $\partial_x f \lambda + \partial_y f \mu = 0$ , and this line is the tangent to the curve at the point  $p_0$ .

*Double intersections:* Consider now the term quadratic in  $t$ ,  $d^2 f/dt^2|_{t=0}$ , supposing that  $\partial_x f = \partial_y f = 0$ . Suppose further that not all of the second partial derivative are zero. Then every line through  $p_0$  has at least 2 intersections at  $p_0$ . As before, there is again an exception: it is possible that  $\mu/\lambda$  takes a value such that  $\partial_x^2 f \lambda^2 + 2\partial_{xy}^2 f \lambda \mu + \partial_y^2 f \mu^2 = 0$ , and these lines are the tangents to the curve at the point  $p_0$ .

*$r^{\text{th}}$  intersections:* Consider now the  $r$ -th term in  $t$ ,  $d^r f/dt^r|_{t=0}$ , supposing that all partial derivatives up to and including the  $(r - 1)$  order vanish. Again, suppose further that not all of the  $r$ -th partial derivative are zero. Then every line through  $p_0$  has at least  $r$  intersections at  $p_0$ . The exceptional case still remains that it is possible that  $\mu/\lambda$  takes a value such that

$$\partial_x^r f \lambda^r + \binom{r}{1} \partial_x^{r-1} \partial_y f \lambda^{r-1} \mu + \dots + \binom{r}{r} \partial_y^r f \mu^r = 0. \quad (128)$$

Again these lines are the tangents to the curve at the point  $p_0$ .

In each of these examples  $p_0$  is said to be an  $r$ -fold point, or a point of multiplicity  $r$ ; a point with multiplicity two or more is referred to as singular. It is clear that for a point to be singular it must be the case that  $f(x_0, y_0) = \partial_x f(x_0, y_0) = \partial_y f(x_0, y_0) = 0$ . We are most interested in 1-fold points, which are referred to as critical points in [39]. One can

prove that the point  $p_0$  is an  $r$ -fold point of the curve if and only if all of the  $(r - 1)$ -th derivatives  $f$  vanish at  $p_0$  but not all the  $r$ -th derivatives [138].

With this in hand we are now in a position to understand the derivation of dispersion relations we are interested in. If the curve  $f(x, y) = 0$  has a non-singular point at  $(x_0, y_0)$ , then either  $\partial_x f$  or  $\partial_y f$  is non-zero. Without loss of generality we can assume it to be  $\partial_y f$ , and this allows the use of the implicit function theorem.

*Analytic implicit function theorem:* Suppose  $f(x_0, y_0) = 0$  and  $\partial_y f(x_0, y_0) \neq 0$ . Then there exist  $\epsilon > 0$  and  $\delta > 0$  such that  $\mathbb{D}_\epsilon(x_0) \times \mathbb{D}_\delta(y_0)$  is in the neighborhood of where  $f$  is defined. In addition there exists an injective function  $g : \mathbb{D}_\epsilon(x_0) \rightarrow \mathbb{D}_\delta(y_0)$  such that  $f(x_0, g(x_0)) = 0$ . Furthermore, for each  $x \in \mathbb{D}_\epsilon(x_0)$ ,  $g(x)$  is the unique solution of  $f(x, g(x)) = 0$ . The mapping  $g(x)$  is analytic in  $\mathbb{D}_\epsilon(x_0)$  and that

$$g'(x) = -\frac{\partial_x f(x, g(x))}{\partial_y f(x, g(x))}. \quad (129)$$

Higher order derivatives can be obtained in a similar way, and hence the implicit function theorem guarantees that an expression for  $y(x)$  exists locally when expressed as a power series of  $(x - x_0)$ , and it converges in a neighborhood of  $x_0$ .

Unfortunately this theorem applies only to a non-singular point, and for the hydrodynamic dispersion relations we are interested in, there can be in principle 1-fold points at the origin of the complex frequency and momentum plane. However, as discussed in [138, 139], the analytic implicit function theorem can be extended to points  $(x_0, y_0) \in \mathbb{C}^2$ , singular or not. In particular, there exist branches of functions  $(x(t), y(t))$  parameterized by  $t$  that are analytic in a neighborhood of  $t = 0$  such that  $(x(0), y(0)) = (x_0, y_0)$  is a root, viz.  $f(x_0, y_0) = 0$ . Furthermore, for every other point  $(x, y)$  there is a unique branch in a suitable neighborhood of  $(x_0, y_0)$  for which  $x = x(t)$  and  $y = y(t)$ . The proof of this is typically attributed to Puiseux and arises from the proof that the field of Puiseux series is algebraically closed. The construction of such a Puiseux series solution to  $f(x, y) = 0$  as well as the pertinent proof can be found in any text on algebraic curves including [138, 139]<sup>50</sup>, and we refer interested readers to them for further details.

The most important result of all this, as was pointed out in [39], is that for a branch given in the neighborhood of  $(x_0, y_0)$ , the series is convergent with a radius of convergence determined by the location of next closest critical point. This can be easily seen recalling the conditions that define the 1-fold or critical points:  $f(x, y) = 0$ ,  $\partial_y f(x, y) = 0$ . With  $f = 0$ , the total derivative is

$$df = \partial_x f dx + \partial_y f dy = 0 \quad \implies \quad \frac{dy}{dx} = -\frac{\partial_x f}{\partial_y f}, \quad (130)$$

and the slope clearly diverges when  $\partial_y f(x, y) = 0$  is also satisfied. In the case of hydrodynamic dispersion relations,  $y$  can be considered as the frequency and  $x$  the momentum. Hence the slope of the dispersion relation diverges at the critical points: i.e. the local explicit solution to the implicit function  $f = 0$  defines the dispersion relation and this relation becomes ill-defined at the location of a critical point. We have thus a method of

---

<sup>50</sup>A particularly easy to follow description of the construction of such a Puiseux series solution is given in [39].

determining the radius of convergence of a hydrodynamic series without having to calculate a large number of coefficients of the series expansion, which may be computationally expensive or difficult.

#### 4.3.2. Determination of the critical point

With the tools discussed above in hand we can proceed to compute the locations of the critical points of the linearized hydrodynamic expansion of a rotating fluid. For this purpose, we focus on the fluid behavior of the  $\mathcal{N} = 4$  SYM theory in a rotating state dual to the MP BH given by Eq. (31), as was done in [32]. From the previous discussion it is clear we must search for 1-fold points, which are solutions to the equations

$$P(j, \nu) = 0, \quad \partial_\nu P(j, \nu) = 0, \quad (131)$$

where  $P$  is the implicit function encoding the dispersion relations  $\nu(j)$ , and  $j = \mathcal{J}/r_+$  here. To obtain  $P$  we recall the method of obtaining QNMs. Roughly, the field equations can be arranged as a generalized eigenvalue problem of the form  $M(j, \nu)\Phi_0 = 0$  where we have grouped the fields together into the object  $\Phi_0$ . The differential operator  $M$  is a function of the frequency and momentum, encoding the QNM spectrum. While we directly solved the generalized eigenvalue problem in Sec. 4.2, an alternative method of obtaining the QNMs is to evaluate the determinant of this operator,  $P(\nu, j) = \det(M(\nu, j))$ , leading to an implicit function in terms of  $(j, \nu)$ , whose roots are precisely the QNM spectrum (more details on the QNM problem and the numerical techniques used in this work can be found in Appendix C). Crucially, this is precisely the implicit function which encodes the dispersion relations of both hydrodynamic and non-hydrodynamic modes of collective excitations about the equilibrium of the CFT dual to this BH geometry.

In Fig. 13 we present the distance from the origin (recall hydrodynamic dispersion relations, constructed as Puiseux series, are roots of the implicit function around the origin of complex frequency-momentum plane) to the nearest critical point of the implicit function  $P$  encoding the dispersion relations for the MP BH in Eq. (31). In the figure we display the nearest critical point for each of the three sectors discussed in Sec. 4.2 as hollow symbols. Interestingly, as already discussed in Sec. 4.2 sectors with successively lower values of  $\mathcal{K}$ , i.e. for instance the scalar sector defined by  $\mathcal{K} = \mathcal{J} - 2$  contain the fields of all higher sectors. As a result, when constructing the implicit function  $P$  one can find numerically that the critical points obtained in, say the tensor sector, also appear in the scalar sector. An organizational strategy is then needed to understand the appearance of the modes. A simple one is to organize by the importance of contributions in a large  $r_+$  expansion. In the strict large BH limit where we consider only the leading term in the limit  $r_+ \rightarrow \infty$  as shown in [29, 32], the behavior of the fluctuation equations is that of a boosted planar black brane.<sup>51</sup> In this limit the sectors decouple, hence the vector sector does not interact with tensor sector, nor does the scalar sector interact with the vector and tensor sector. Furthermore, the discrete momentum  $j = \mathcal{J}/r_+$  becomes a continuous variable. Hence the hollow symbols in Fig. 13 are those obtained in this limit. A consequence of this limit is that one can interpret these critical points like in [39] as radii of convergence of the dispersion relations obtained from the implicit function representing the hydrodynamic expansion. It is for this reason we label the vertical axis in the plot as  $R_c$ , the convergence radius of the corresponding sector.<sup>52</sup>

---

<sup>51</sup>An example of the relation between the Wigner-D functions and Fourier transformations in the large

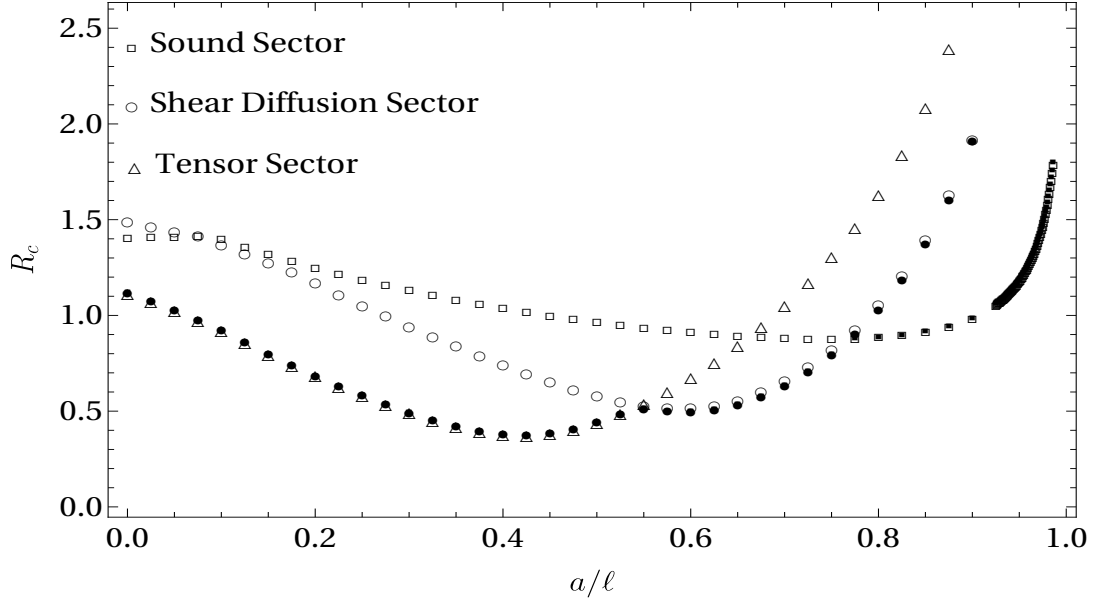


Figure 13: The convergence radius,  $R_c$ , of the hydrodynamic expansion as a function of the angular momentum parameter  $a/\ell$ . Hollow symbols indicate the value of the distance from the origin ( $j = 0$ ) to the nearest critical point  $j = j_c$  in the strict large BH limit (large temperature),  $R_c(r_+ \rightarrow \infty)$ , while solid symbols indicate this value in the full MP BH with horizon radius  $r_+/\ell = 100$ . The sector with the smallest absolute value determines  $R_c$ . Adapted from [32].

It was already shown in [29] that the QNM spectrum behaves, roughly speaking, hydrodynamically for  $r_+/\ell \approx O(10^2)$ . Therefore one can think of the large BH limit, in a sense, as a hydrodynamic limit of the rotating MP BH solution. In [32] it was shown that the QNMs, which are also critical points, already behave hydrodynamically for  $r_+/\ell \approx O(10^2)$ . This is displayed in Fig. 14, which shows the ratio of the nearest critical point to the origin for a finite horizon radius to that of the nearest mode in the strict  $r_+ \rightarrow \infty$  limit. It is interesting to note that differences (on the percent level) in the radius of convergence only begin to appear for  $r_+/\ell \approx O(10^2)$ .

Interestingly, the effect which more severely limits the radius of convergence of the hydrodynamic series away from the large BH limit is the interaction of modes of different values of  $\mathcal{K}$ . While the tensor sector ( $\mathcal{K} = \mathcal{J} - 2$ ) does not contain any hydrodynamic modes, the implicit function encoding the dispersion relations does contain critical points, and these points are closer to the origin in the complex momentum plane. This is reflected in the radius of convergence displayed as the solid symbols in Fig. 13. The resulting radius of convergence is still non-zero and finite, but its behavior has changed qualitatively and quantitatively as a result of the appearance of the inter-sector couplings implied by the Einstein equations.

The radius of convergence of the hydrodynamic expansion in momentum space,  $R_c$ , is finite and non-zero in a holographic vortical fluid flow; see Fig. 13. Corrections to

BH limit is discussed in Appendix F.

<sup>52</sup>It should be noted that in the large BH limit there are no hydrodynamic modes in the tensor sector. However these play a role as one moves away from the large BH limit.

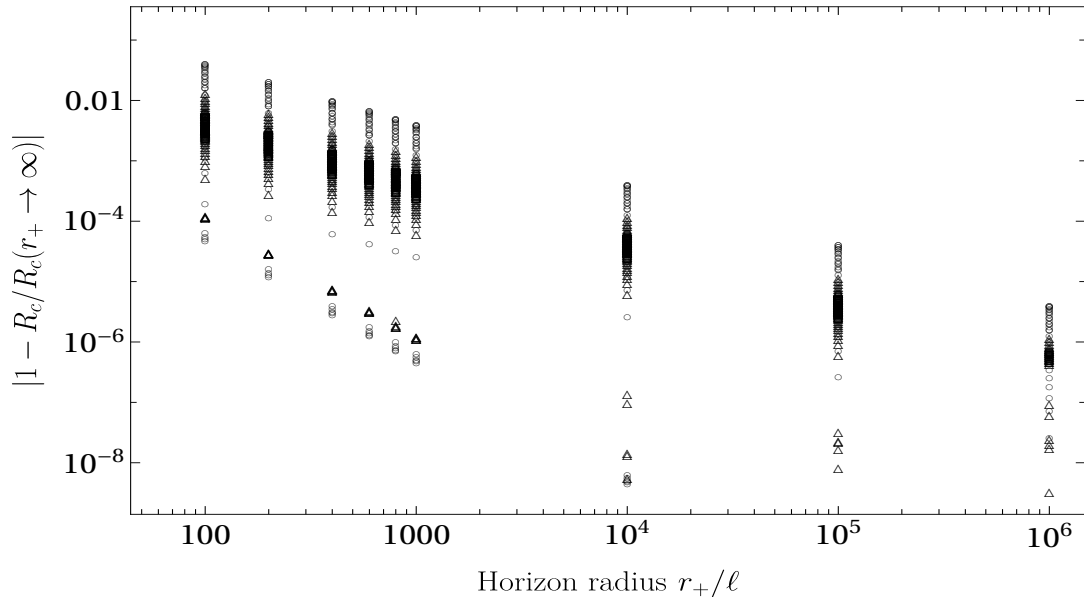


Figure 14: The deviation of the convergence radius of the hydrodynamic expansion,  $R_c$ , from its value in the large BH limit,  $R_c(r_+ \rightarrow \infty)$ , as a function of the horizon radius (normalized to its value in the large BH limit). The various points represent different values of the angular momentum parameter  $a/\ell$ . The vertical width of the bands displays the “strength” of rotational effects on the radius of convergence. The plot markers are the same as those used in Fig. 13. Adapted from [32].

the strict large temperature limit are at most at the percent level for intermediate temperatures (BH radii,  $r_+/\ell \approx 100$ ); see Fig. 14.

#### 4.4. Pole-Skipping

In this section, we give an overview of the pole-skipping phenomenon in the MP background (described in Sec. 3) discussed in the recent work [33]. While the critical points discussed in the previous section can be shown to arise as the result of mode collisions in the complex frequency-momentum plane, pole-skipping modes arise when the residue of a Green’s function “collides” with the would-be pole, and as a result the residue vanishes at the pole, and the pole is “skipped”. The study of pole-skipping has garnered much attention in recent years due to the discovery in [42]. The authors of [42] found that in the gravitational shockwave calculations [43, 44], the scrambling rate of the dual strongly-coupled quantum field theory is directly related to the hydrodynamic sound modes of the theory. This realization quickly led to the development of effective descriptions of quantum chaos, and the general prediction of pole-skipping in the energy-energy correlation functions as a “smoking gun” for the hydrodynamic origin for the chaotic mode [48, 49]. When this occurs, it provides a potentially simpler method of obtaining information to characterize the chaotic dynamics (maximal Lyapunov exponents and butterfly velocities) than the computation of OTOCs, a standard way to diagnose operator growth in chaotic quantum field theories. Although much is known about these quantities in simple settings, less is known about their behavior in non-trivial states of chaotic quantum field theories, such as the rotating state dual to the MP BH we consider. Earlier works have considered the rotating BTZ BH dual to a (1+1)-dimensional CFT with a chemical potential for rotation [140, 141, 84], and the field theory dual to a (3+1)-dimensional rotating Kerr-AdS BH [142].

#### 4.4.1. Gravitational shockwaves

Ref. [33] focused on computations of OTOCs in the field theory dual to Eq. (31) of the form

$$\langle \hat{W}(t_2, \Psi_2, \Phi_2, \Theta_2) \hat{V}(t_1, \Psi_1, \Phi_1, \Theta_1) \hat{W}(t_2, \Psi_2, \Phi_2, \Theta_2) \hat{V}(t_1, \Psi_1, \Phi_1, \Theta_1) \rangle, \quad (132)$$

where capital letters denote boundary coordinates, the difference in operator insertions is large compared to the inverse temperature  $t_2 - t_1 \gg \beta$  and the angled brackets denote the trace with respect to the thermal density matrix  $e^{-\beta H}/Z$  in the dual field theory. The gravitational process dual to this OTOC is the scattering amplitude between a particle of momentum  $p_1^U$  travelling along the  $V = 0$  horizon of the BH (corresponding to quanta created by the  $\hat{V}$  operator) and a particle of momentum  $p_2^V$  travelling along the  $U = 0$  horizon (corresponding to quanta created by the  $\hat{W}$  operator). The OTOC is then given by an integral, over momenta and angular coordinates, of  $e^{i\delta}$  (a two-two scattering amplitude) weighted by bulk-boundary wave functions, which describe the distribution of quanta along at the horizon [44].

The computation is made feasible by working in the eikonal approximation [143] which consists of linearizing the gravitational Lagrangian and treating the two particles (created by  $\hat{V}$  and  $\hat{W}$ ) as fixed energy momentum sources following their classical trajectories. The scattering amplitude for this process,  $e^{i\delta}$ , is given by evaluating the Einstein-Hilbert action, expanded to quadratic order, on the classical solutions sourced by the  $\hat{V}$  and  $\hat{W}$  operators [143, 43, 44]

$$\delta = \frac{1}{2} \int d^5x \sqrt{-g} (\delta g_{UU} \mathcal{D}^2 \delta g_{VV} + \delta g_{UU} T^{UU} + \delta g_{VV} T^{VV}), \quad (133)$$

where  $\mathcal{D}^2$  is related to the inverse of the graviton propagator and as noted in [44], the first term is equal in magnitude but opposite in sign as the other terms in Eq. (133).

Before discussing the extraction of the OTOC from the gravitational amplitude we begin by computing the linearized backreaction of the two particles following (near) geodesic trajectories on the geometry.<sup>53</sup> These solutions are examples of the well known shockwave geometries [45, 46, 47]. The trajectory of the particle of momentum  $p_1^U$  approximates the null geodesic given by  $(U = U(\tau), V = 0, \tilde{\psi}_1, \phi_1, \theta_1)$ . The only non-zero component of the stress tensor of this particle is given by

$$T^{UU} = \frac{1}{\sqrt{-g}} p_1^U \delta(V) \delta(\tilde{\psi} - \tilde{\psi}_1) \delta(\phi - \phi_1) \delta(\theta - \theta_1), \quad (134)$$

while the particle of momentum  $p_1^V$  follows the null-geodesic  $(U = 0, V = V(\tau), \tilde{\psi}_2, \phi_2, \theta_2)$ , with the stress tensor

$$T^{VV} = \frac{1}{\sqrt{-g}} p_2^V \delta(U) \delta(\tilde{\psi} - \tilde{\psi}_2) \delta(\phi - \phi_2) \delta(\theta - \theta_2). \quad (135)$$

The only non-zero component of the stress tensor sourced by the  $\hat{V}$  quanta is  $T_{VV} = A(0)^2 T^{UU}/4$ . The ansatz for the gravitational backreaction of this source takes the form

---

<sup>53</sup>This calculation is most easily done in Kruskal coordinates. These are detailed in the original paper [33] but are included in appendix Appendix D for convenience.

of a shockwave across the  $U = 0$  horizon,  $U \rightarrow U + f_1(\tilde{\psi}, \phi, \theta)$  which can be written to leading order as

$$\delta g_{VV} = -A(0)f_1(\tilde{\psi}, \phi, \theta)\delta(V). \quad (136)$$

Inserting the ansatz (136) into Einstein's equations, one finds that the  $VV$ -component is the only non-trivial equation, which reduces to the following partial differential equation for the angular profile  $f_1(\tilde{\psi}, \phi, \theta)$

$$\mathcal{D}f_1(\tilde{\psi}, \phi, \theta) = (\square + \lambda_1 + \lambda_2\partial_{\tilde{\psi}} + \lambda_3\partial_{\tilde{\psi}}^2)f = \frac{16\pi G_N}{\sin(\theta_1)} \frac{K}{\ell r_+^2} p_1^U \delta(\tilde{\psi} - \tilde{\psi}_1) \delta(\phi - \phi_1) \delta(\theta - \theta_1), \quad (137)$$

with  $\square$  given by <sup>54</sup>

$$\square = \cot(\theta)\partial_\theta + \partial_\theta^2 + \csc^2(\theta)\partial_{\tilde{\psi}}^2 + \csc^2(\theta)\partial_\phi^2 - 2\cot(\theta)\csc(\theta)\partial_{\tilde{\psi}}\partial_\phi, \quad (138)$$

where  $\lambda_1, \lambda_2, \lambda_3$  are constants given by the expressions

$$\lambda_1 = \frac{(2K^2 + \ell^2 r_+^2)(2a^2(r_+^2 + \ell^2)^2 - \Delta)}{4\ell^4 r_+^2 K^2}, \quad \lambda_2 = -\frac{2a(r_+^2 + \ell^2)K}{\ell^3 r_+^2}, \quad \lambda_3 = -\frac{a^2(r_+^2 + \ell^2)}{\ell^2 r_+^2}. \quad (139)$$

In these expressions, Eq. (137) and Eq. (139) we have made use of two quantities  $\Delta$  and  $K$  to shorten the expressions, these constants are defined as

$$\Delta = \ell^2 r_+^2 (\ell^2 + 2r_+^2), \quad K = \sqrt{\ell^2 r_+^2 - a^2(\ell^2 + r_+^2)} \quad (140)$$

Repeating these steps we can now consider the  $W$  quanta travelling on the  $U = 0$  horizon. The calculation goes through as above, only now the geometry is shifted across the  $U = 0$  horizon  $V \rightarrow V + f_2(\tilde{\psi}, \phi, \theta)$ . To linear order in  $f_2$  this leads to the requirement that  $f_2(\tilde{\psi}, \phi, \theta)$  satisfy

$$\tilde{\mathcal{D}}f_2(\tilde{\psi}, \phi, \theta) = \frac{16\pi G_N}{\sin(\theta_2)} \frac{K}{\ell r_+^2} p_2^V \delta(\tilde{\psi} - \tilde{\psi}_2) \delta(\phi - \phi_2) \delta(\theta - \theta_2), \quad (141)$$

where  $\tilde{\mathcal{D}}$  is the same differential operator given in (137) but with the replacements  $\partial_{\tilde{\psi}} \rightarrow -\partial_{\tilde{\psi}}$  and  $\partial_\phi \rightarrow -\partial_\phi$ .

As was first demonstrated in [33], we can find a general analytic solution to the angular profile of the shockwave. Introducing  $f(\tilde{\psi}, \phi, \theta, \theta')$  as the Green's function of the Laplacian on  $S^3$  with normalised delta-function source

$$\mathcal{D}f(\tilde{\psi}, \phi, \theta, \theta') = -\frac{1}{2\sin(\theta')} \delta(\tilde{\psi}) \delta(\phi) \delta(\theta - \theta') \quad (142)$$

we can expand the delta functions in terms of Wigner D-functions using the completeness relation given in Eq. (49). Using the fact that the Wigner D-functions satisfy

$$\square D_{\mathcal{KM}}^{\mathcal{J}} + \mathcal{J}(\mathcal{J} + 1)D_{\mathcal{KM}}^{\mathcal{J}} = 0, \quad (143)$$

---

<sup>54</sup>It turns out that this operator is one quarter of the Laplacian on the unit 3-sphere written in terms of the Hopf fibration.

we can solve Eq. (142) for the normalised shockwave profile

$$f(\tilde{\psi}, \phi, \theta, \theta') = \sum_{\mathcal{J}=0,1/2,1,\dots}^{\infty} \sum_{\mathcal{K}=-\mathcal{J}}^{\mathcal{J}} \sum_{\mathcal{M}=-\mathcal{J}}^{\mathcal{J}} \frac{2\mathcal{J}+1}{16\pi^2} \frac{d_{\mathcal{K}\mathcal{M}}^{\mathcal{J}}(\theta') d_{\mathcal{K}\mathcal{M}}^{\mathcal{J}}(\theta)}{\mathcal{J}(\mathcal{J}+1) - \lambda_1 - i\lambda_2\mathcal{K} + \lambda_3\mathcal{K}^2} e^{i\mathcal{K}\tilde{\psi} + i\mathcal{M}\phi}, \quad (144)$$

where we have made use of the decomposition of the Wigner D-functions in terms of the Wigner d-functions  $D_{\mathcal{K}\mathcal{M}}^{\mathcal{J}}(\tilde{\psi}, \phi, \theta) = d_{\mathcal{K}\mathcal{M}}^{\mathcal{J}}(\theta) e^{i\mathcal{K}\tilde{\psi} + i\mathcal{M}\phi}$ . Finally, by using the general Green's function, we compute the eikonal phase<sup>55</sup> from the action in Eq. (133)

$$\delta = \frac{16\pi G_N K}{\ell r_+^2} A(0) p_1^U p_2^V f(\psi_2 - \psi_1, \phi_2 - \phi_1, \theta_2, \theta_1). \quad (145)$$

Unfortunately, for general configurations  $(\psi, \phi, \theta, \theta')$  we have not encountered a simple way to evaluate the sum in Eq. (144). However, there do exist configurations for which one can obtain an explicit closed form of the OTOC in the large BH limit. Making use of the existence of radially in-falling geodesics which satisfy  $\dot{\theta} = \dot{\phi} = 0$  [144] we can consider configurations for which the operators  $\hat{V}$  and  $\hat{W}$  lie on a Hopf circle (and hence are only separated in the direction of the fibre coordinate  $\psi$ , parallel to the rotation). Such operator configurations with  $\Theta_1 = \Theta_2 = \Theta$  and  $\Phi_1 = \Phi_2 = \Phi$  can be mapped by an isometry to the North pole, i.e. without loss of generality we consider configurations for which  $\Theta = \Phi = 0$ . The OTOC then takes the form

$$H(t, \Psi) = \langle W(t_2, \Psi_2, 0, 0) V(t_1, \Psi_1, 0, 0) W(t_2, \Psi_2, 0, 0) V(t_1, \Psi_1, 0, 0) \rangle \quad (146)$$

where  $t = t_2 - t_1$  and  $\Psi = \Psi_2 - \Psi_1$ .

To obtain the closed form expression of the OTOC we work in the large BH limit  $r_+ \gg \ell$  where the bulk to boundary wave-functions describing the distribution of quanta on the horizon will be sharply peaked in the angular coordinates on the horizon around  $\tilde{\psi}_2 - \tilde{\psi}_1 = \Psi - \bar{\Omega}t$ ,  $\theta_1 \approx \theta_2 \approx 0$ ,  $\phi_1 \approx \phi_2 \approx 0$ . Expanding the standard expression from [44] for the OTOC to leading order in  $G_N$ , and using that the bulk-to-boundary wave-functions are sharply peaked around<sup>56</sup>  $p_1^U p_2^V \sim e^{2\pi T t}$ , the OTOC then takes the form

$$H(t, \Psi) \sim 1 - c G_N e^{2\pi T t} f(\Psi - \bar{\Omega}t), \quad (148)$$

where  $c$  is a constant and  $f(\tilde{\psi})$  is the solution to equation (142) with  $\theta = \theta' = \phi = 0$ . As was shown in the appendix of [33] in the large BH limit the expression (144) can be approximated by an integral, leading to the expression

$$f(\tilde{\psi}) = \int_0^\infty d\mathcal{J} \int_{-\mathcal{J}}^{\mathcal{J}} d\mathcal{K} \frac{\mathcal{J}}{4\pi^2} \frac{e^{i\mathcal{K}\tilde{\psi}}}{\mathcal{J}^2 - \lambda_1 - i\lambda_2\mathcal{K} + \lambda_3\mathcal{K}^2} \quad (149)$$

<sup>55</sup>Note here we have used rotational symmetry in the  $\phi, \tilde{\psi}$  directions and that  $\tilde{f}(\tilde{\psi}_1 - \tilde{\psi}_2, \phi_1 - \phi_2, \theta_1, \theta_2) = f(\tilde{\psi}_2 - \tilde{\psi}_1, \phi_2 - \phi_1, \theta_2, \theta_1)$  with  $\tilde{f}$  the solution to the analogous equation to Eq. (142) with  $\mathcal{D} \rightarrow \bar{\mathcal{D}}$ .

<sup>56</sup>we note that in the large BH limit the expressions for the temperature and angular velocity reduce to

$$2\pi T = \frac{2r_+}{\ell^2} \sqrt{1 - a^2/\ell^2}, \quad \bar{\Omega} = -2a/\ell^2. \quad (147)$$



for the shock-wave profile on Hopf circles. This integral can be computed exactly by contour integration (see [33] for details)

$$f(\tilde{\psi}) = -\frac{1}{4\pi|\tilde{\psi}|} \begin{cases} e^{-k_+\tilde{\psi}}, & \tilde{\psi} > 0 \\ e^{k_-\tilde{\psi}}, & \tilde{\psi} < 0 \end{cases} \quad (150)$$

where

$$k_{\pm} = \frac{r_+}{\ell\sqrt{1-a^2/\ell^2}} \left( \sqrt{\frac{3}{2}} \mp \frac{a}{\ell} \right). \quad (151)$$

In co-rotating coordinates, the OTOC is therefore exponentially growing in time with an exponent  $2\pi T t$  and exponentially decaying in the  $\tilde{\psi}$  direction governed by  $k_{\pm}$ . Hence we now arrive at one of the main results of [33] and of this section. Given in terms of the fixed boundary coordinates  $(t, \Psi)$  the OTOC takes the functional form

$$H(t, \Psi) \sim 1 - \frac{cG_N}{4\pi|\Psi - \Omega t|} \begin{cases} \exp\left(2\pi T_+ \left(t - \frac{\ell\Psi}{2v_B^{\pm}}\right)\right), & \Psi - \bar{\Omega}t > 0, \\ \exp\left(2\pi T_- \left(t - \frac{\ell\Psi}{2v_B^{\mp}}\right)\right), & \Psi - \bar{\Omega}t < 0 \end{cases} \quad (152)$$

where  $\ell\Psi/2$  corresponds to the spatial distance between the operators  $\hat{V}, \hat{W}$  and the exponents  $T_{\pm}, v_B^{\pm}$  are given by

$$2\pi T_{\pm} = \frac{2r_+}{\ell^2\sqrt{1-a^2/\ell^2}} \left( 1 \mp \sqrt{\frac{3}{2}} \frac{a}{\ell} \right), \quad (153)$$

$$\frac{2\pi T_{\pm}}{v_B^{\pm}} = \frac{2r_+}{\ell^2\sqrt{1-a^2/\ell^2}} \left( \sqrt{\frac{3}{2}} \mp \frac{a}{\ell} \right). \quad (154)$$

A quick inspection of Eq. (153) and Eq. (154) reveals that these expressions can be obtained by applying a boost of velocity  $v = -\bar{\Omega}\ell/2 = a/\ell$  to the expression  $H_4 \sim \exp(2\pi T_0(t - \ell\Psi/2v_B^{(0)}))$  for the OTOC of the AdS<sub>5</sub>-Schwarzschild black brane. Performing a Lorentz transformation of this form gives

$$2\pi T_{\pm} = 2\pi T_0 \gamma_v \left( 1 \mp \frac{v}{v_B^{(0)}} \right), \quad \frac{2\pi T_{\pm}}{v_B^{\pm}} = 2\pi T_0 \gamma_v \left( \frac{1}{v_B^{(0)}} \mp v \right), \quad (155)$$

which are equivalent to (153) and (154) upon using the expressions  $2\pi T_0 = 2r_+/\ell^2$  and  $v_B^{(0)} = \sqrt{2/3}$ , with  $v_B^{(0)}$  the butterfly velocity of the static Schwarzschild-AdS<sub>5</sub> black brane.

Before demonstrating that this butterfly also has a hydrodynamic origin, as discussed in the introduction to this section, we note that the Lyapunov exponent  $\lambda_L$  associated to the OTOC on Hopf circles can be extracted from  $H(t, 0)$  in Eq. (152) (see for instance [141]). Doing so gives  $\lambda_L = 2\pi T_+ = \text{Im}(\omega_+)$  (for  $a > 0$ ) and  $\lambda_L = 2\pi T_- = \text{Im}(\omega_-)$  (for  $a < 0$ ). We therefore have that

$$\lambda_L = 2\pi T \left( 1 - \sqrt{\frac{3}{2}} \frac{|a|}{\ell} \right) = 2\pi T \left( 1 - |v|/v_B^{(0)} \right) \quad (156)$$

which, as discussed in [33], saturates a velocity-dependent generalization of the Maldacena-Shenker-Stanford chaos bound [145] originally proposed in [141]. Furthermore, this naturally saturates the generalized bound for the positive operators  $\theta_a Q_a$  proposed in [141], given by

$$\frac{|\theta_a [Q_a]^\mu \partial_\mu H|}{1 - H} \leq 2\pi. \quad (157)$$

where  $H$  is the OTOC,  $\theta_a$  are chemical potentials and  $Q_a$  are the corresponding generators. In our case the operators are given by  $\theta_a Q_a = \beta(\tilde{H} + \bar{\Omega}J)$  (with  $\beta$  the inverse temperature,  $\tilde{H}$  the Hamiltonian,  $J$  the angular momentum and  $\bar{\Omega}$  the angular velocity) and in this case the generalized bound given above in equation (157) reduces to

$$\frac{|\partial_t H(t, \psi) + \bar{\Omega} \partial_\psi H(t, \psi)|}{1 - H(t, \psi)} \leq 2\pi T. \quad (158)$$

Using the definition of the OTOC given in equation (148) one finds the bound is saturated <sup>57</sup>

#### 4.4.2. Near horizon metric fluctuations

As demonstrated in [33] and discussed in the introduction of this section, we now turn to the hydrodynamic origin of chaos in our holographic system, and we give an overview of the calculation done to extract information about the retarded Green's function,  $G_{T00T00}^R$ , from the study of infalling metric perturbations. We will see that this exhibits the characteristic features of pole-skipping as identified in [42, 48, 49]. To be concrete, at a special value of the frequency  $\omega = i2\pi T$  the linearized Einstein equations admit an additional infalling mode when the angular profile of the metric component  $\delta g_{vv}$  at the horizon is solution to the (sourceless) shockwave Eq. (137) that governs the form of the OTOC.

Unlike the discussion of the previous section we now take the infalling Eddington-Finkelstein coordinates (see Appendix D)  $(v, r, \tilde{\psi}, \phi, \theta)$ .<sup>58</sup> We then study linearized perturbations of the metric of the form

$$\delta g_{\mu\nu}(v, r, \tilde{\psi}, \phi, \theta) = e^{i(k\tilde{\psi} - \omega v)} \delta g_{\mu\nu}(r, \phi, \theta) \quad (159)$$

Note that we have not yet employed the full machinery of the Wigner D-functions as developed in Sec.3. We initially refrain from this in order to demonstrate the equivalence between the linearized Einstein equations near the horizon and the shockwave computation. Inserting this ansatz into the linearized Einstein equations will give rise to a coupled set of coupled PDEs for  $\delta g_{\mu\nu}(r, \phi, \theta)$ . In particular, as in previous examples of pole-skipping, we find that at  $\omega = i2\pi T$  the  $vv$  component of the Einstein equations at  $r = r_+$  reduces to a decoupled equation for the angular profile of  $\delta g_{vv}$  evaluated at the horizon. Furthermore, all other metric perturbation decouple from this component of the

<sup>57</sup>It was pointed out already in [142], that rotating systems in 1+1 d (e.g. [84]) have been noticed to satisfy the generalized MSS bound of [141].

<sup>58</sup>Note we still choose the co-rotating coordinate defined as  $\tilde{\psi} = \psi - \bar{\Omega}t$ , along with the corresponding change in the form basis  $\tilde{\sigma}_3 = d\tilde{\psi} + \cos(\theta)d\phi$ .

Einstein equations which takes the form

$$\left\{ \left[ \cot(\theta)\partial_\theta + \partial_\theta^2 - \csc^2(\theta)k^2 + \csc^2(\theta)\partial_\phi^2 - 2i\cot(\theta)\csc(\theta)k\partial_\phi \right] + \lambda_1 + i\lambda_2k - \lambda_3k^2 \right\} \delta g_{vv}(r_+, \phi, \theta) = 0, \quad (160)$$

where  $\lambda_1$ ,  $\lambda_2$  and  $\lambda_3$  the same constants defined in Eq. (139). As advertised, Eq. (160) is precisely the source-less version of the shockwave equation governing the form of OTOC (137), after a Fourier transform with respect to the  $\psi$  coordinate. The key point is that the metric perturbation  $\delta g_{vv}(r_0, \phi, \theta)$  must either have a specific angular profile on the horizon (i.e. be a non-trivial solution to Eq. (160)) or it must be zero at the horizon. As such, for metric perturbations with a particular angular profile related to the shockwave equation we expect an extra infalling mode, and the pole-skipping phenomenon.

We can go further by recalling that the Wigner D-functions are related to the Wigner d-functions as  $\mathcal{D}_{\mathcal{K}\mathcal{M}}^{\mathcal{J}}(\tilde{\psi}, \theta, \phi) = d_{\mathcal{K}\mathcal{M}}^{\mathcal{J}}(\theta)e^{i\mathcal{K}\tilde{\psi} + i\mathcal{M}\phi}$ . With this in mind we can parameterize  $\delta g_{vv}(r_+, \phi, \theta) = e^{i\mathcal{K}\phi}d_{\mathcal{K}\mathcal{M}}^{\mathcal{J}}(\theta)$ , inserting this into Eq. (160) leads to the statement that at pole-skipping points the quantum numbers  $\mathcal{K}$  and  $\mathcal{J}$  are related by <sup>59</sup>

$$\lambda_1 + i\lambda_2\mathcal{K} - \lambda_3\mathcal{K}^2 = \mathcal{J}(\mathcal{J} + 1). \quad (161)$$

It is worth pointing out that as a result of the equivalence between the horizon equation and shockwave equation, this relationship corresponds exactly to the locations of the poles in the shockwave profile given in Eq. (144).

To compare to Eq. (152) we take the large BH limit  $r_+/\ell \gg 1$  while keeping  $a/\ell \sim \mathcal{O}(1)$ . In this limit the leading order behavior of the constants  $\lambda_1$ ,  $\lambda_2$ ,  $\lambda_3$  is

$$\lambda_1 = \frac{r_+^2}{2\ell^4}(2a^2 - 3\ell^2), \quad \lambda_2 = -\frac{2ar_+}{\ell^2}\sqrt{1 - \frac{a^2}{\ell^2}}, \quad \lambda_3 = -\frac{a^2}{\ell^2}.$$

As we discussed in Sec.4.2, sectors in the MP BH are determined by a choice of the quantum number  $\mathcal{K}$ , here we will consider the class of pole-skipping points where  $\mathcal{K}$  is parallel to the rotation direction i. e. taking its maximal value ( $\mathcal{K} = \mathcal{J}$ ). Further, we recall that in the large BH limit we also choose the momentum to scale with the horizon radius as  $\mathcal{J} \sim r_+/\ell \gg 1$ . Equipped with a behavior of the momentum in the large BH limit we find that Eq. (161) reduces to the following quadratic equation for  $\mathcal{J}$

$$\left(1 - \frac{a^2}{\ell^2}\right) \mathcal{J}^2 + \frac{2iar_+}{\ell^2}\sqrt{1 - \frac{a^2}{\ell^2}}\mathcal{J} + \frac{r_+^2}{2\ell^4}(3\ell^2 - 2a^2) = 0, \quad (162)$$

whose solutions are given by

$$\mathcal{J} = \pm \frac{ir_+}{\ell\sqrt{1 - a^2/\ell^2}} \left( \sqrt{\frac{3}{2}} \mp \frac{a}{\ell} \right) = \pm ik_\pm. \quad (163)$$

---

<sup>59</sup>It is important to understand that for integer and half-integer  $\mathcal{J}$  with  $|\mathcal{M}|, |\mathcal{K}| \leq \mathcal{J}$  there is a unique solution to Eq. (143) that is regular on  $S^3$ . In order to consider pole-skipping, it is necessary to relax the condition that  $\mathcal{M}, \mathcal{K}, \mathcal{J}$  be integers and consider them to be arbitrary complex parameters. This corresponds to considering angular profiles of the metric components that are not necessarily regular on the three-sphere.

Finally, we see these modes exhibit pole-skipping at a frequency  $\omega = i2\pi T$  and at precisely the same wave-vectors  $k_{\pm}$  that appear in the exponential form of the OTOC when the operators lie on a Hopf circles (see Eq. (152)).

So far we have been working in terms of co-rotating coordinates, hence the boundary response is characterized by coordinates  $(t, \tilde{\psi}, \theta, \phi)$ . If, however, we transform these results to the standard coordinates  $(t, \psi, \theta, \phi)$  for the three sphere, then we find that the wave-vectors  $k_{\pm}$  at which pole-skipping occurs are unchanged, while the frequencies are modified to

$$\omega_{\pm} = i(2\pi T \pm k_{\pm} \bar{\Omega}) = \frac{2ir_+}{\ell^2 \sqrt{1 - a^2/\ell^2}} \left( 1 \mp \sqrt{\frac{3}{2}} \frac{a}{\ell} \right). \quad (164)$$

Before closing this section it is worth discussing one of the main conclusions of this section in more detail. Namely, we have seen that the pole-skipping locations uncovered in the near horizon analysis of the Einstein equations match precisely the poles of the summand in the expression for the angular profile of the shockwave geometry (compare Eq. (161) and Eq. (144)). And, furthermore, in the large BH limit, where we can obtain a closed form expression for the OTOC, the pole-skipping points match precisely the wave vector and exponential growth rate of the OTOC (compare Eq. (164) and Eq. (163) to Eq. (153) and Eq. (154)). As already remarked, the form of the OTOC in this limit can be obtained directly from the equivalent calculation in a Schwarzschild black brane by performing a Lorentz transformation. To be concrete, for a non-rotating Schwarzschild AdS black brane geometry it is the pole-skipping points in the scalar channel which precisely match the wave vector and exponential growth rate of the OTOC, these are given by [44]

$$\mathfrak{w} = i, \quad \mathfrak{q} = \pm \sqrt{\frac{3}{2}} i. \quad (165)$$

Therefore, we should expect to see explicitly that the equations of motion for the fluctuations in the scalar channel of the MP BH reduce to those of a boosted Schwarzschild black brane in the large BH limit, and we should be able to numerically verify directly that the mode given by Eq. (165), when boosted appropriately, is contained in the spectrum of fluctuations.

To see these observations we turn to the scalar channel as discussed in Sec.4.2 and take the large BH limit defined in Eq. (112) and (113) keeping only the leading term in  $r_+/\ell$ . From doing this the fluctuations  $(h_{33}, h_{tt}, h_{t3}, h_{+-}, h_{+t}, h_{+3}, h_{++})$  decouple into three channels: scalar  $(h_{33}, h_{tt}, h_{t3}, h_{+-})$ , vector  $(h_{+t}, h_{+3})$ , and tensor  $(h_{++})$ . Again, focusing on the scalar channel, one finds 7 equations, which can be arranged as four dynamical equations and three constraints. Transforming to the coordinate  $u = (r_+/r)^2$  (and setting  $\ell = 1$  for simplicity), an analysis of residual gauge symmetry leads to a master variable  $Z_0(u)$  which can be constructed from the fields  $(h_{33}, h_{tt}, h_{t3}, h_{+-})$  as

$$Z_0(u) = (2(j^2(a^2 - z^4 - 1) - a^2\nu^2(z^4 + 1) - 2aj\nu z^4 + \nu^2)h_{+-}(u) + (a^2 - 1)(j^2 h_{tt}(u) - 4j\nu h_{t3}(u) + 4\nu^2 h_{33}(u))). \quad (166)$$

In terms of this master variable the scalar channel can be reduced to a single equation

$$0 = \frac{(a^2(4u^2 - u\nu^2 - 4) - 2aju\nu - u(j^2 + 4u) + 4)}{a^2 - 1} Z_0(u) + \frac{f(u)}{u} (3u^2 - 5) Z_0'(u) + \frac{f(u)^2}{u^2} Z_0''(u), \quad (167)$$

At this point, as was shown originally in [33], we can demonstrate that the explicit dependence on the rotation parameter  $a$  can be removed by the following Lorentz boost

$$\begin{aligned} \mathfrak{q} &= \frac{a\nu + j}{\sqrt{1 - a^2}}, & \mathfrak{q} &= \frac{k}{2\pi T}, \\ \mathfrak{w} &= \frac{\nu + aj}{\sqrt{1 - a^2}}. & \mathfrak{w} &= \frac{\omega}{2\pi T}, \end{aligned} \quad (168)$$

after which the resulting  $a$ -independent equation is equivalent to the equation for the master field governing (scalar sector) metric perturbations around a Schwarzschild AdS black brane [38]. Hence, (167) is simply the master equation<sup>60</sup> for scalar fluctuations around a boosted black brane, where the momentum of the fluctuations is aligned with the boost direction.

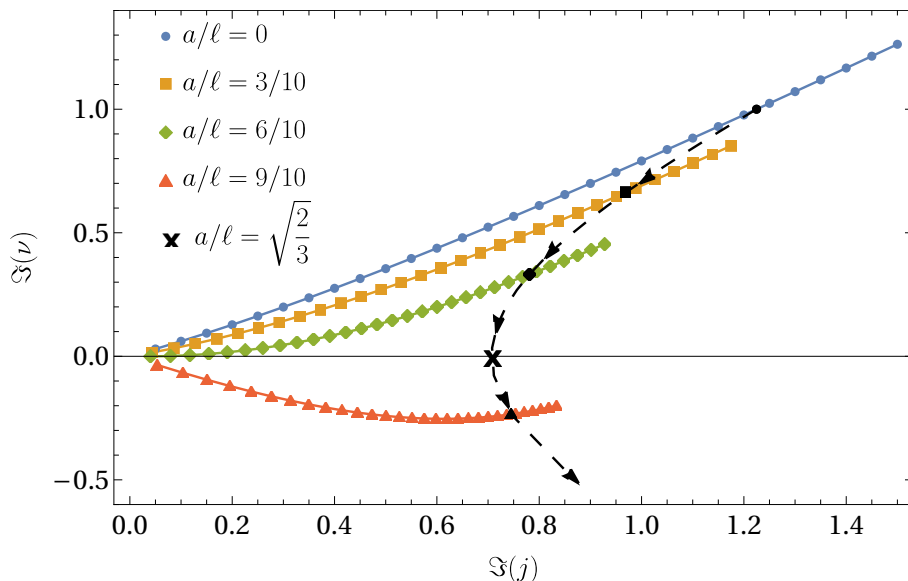


Figure 15: *Chaos in the sound dispersion.* The complex-valued dispersion relation  $\nu(j)$  for the rotating BH in the large BH limit. Displayed is the imaginary part of the frequency parameter  $\Im(\nu)$  of the perturbation as a function of the imaginary part of its angular momentum  $\Im(j)$ . Each color (and different symbol) represents a different value for the angular momentum per mass  $a/\ell$  in incremental steps of  $3/10$ . The black line indicates the trajectory of the pole-skipping location as the angular momentum per mass,  $a/\ell$ , varies. The cross,  $\times$ , highlights the point where one of the pole-skipping points associated to this dispersion relation ceases to be located in the upper half plane, corresponding to  $a/\ell = \sqrt{2/3}$ . Adapted from [33].

Having confirmed explicitly that the fluctuation equations in the large BH limit reduce to those of a boosted Schwarzschild black brane it is then a simple matter to apply Eq. (168) to Eq. 165) to confirm that it gives that the pole-skipping points in Eq. (164) and Eq. 163). Furthermore, in [33] pole-skipping at these locations was verified explicitly by numerically<sup>61</sup> solving for the dispersion relation of the (sound) QNM in the scalar sector

<sup>60</sup>In fact, it was demonstrated in [33] that in all three sectors (scalar, vector, tensor) of the MP BH, expanded in the large BH limit, the metric perturbations be reduced in the same way to fluctuations around a boosted Schwarzschild AdS black brane.

<sup>61</sup>This was done using two independent methods from two independently constructed routines, first, from a static Schwarzschild black brane whose modes were then boosted and second, directly from the large BH limit of the rotating BH (for further details see the Appendix of [33]).

of perturbations for each value of  $a/\ell$ . These numerical results are illustrated in 15. The pole-skipping locations are indicated with black symbols in Fig. 15 for increasing values of rotation  $a/\ell$ . As noted in [33], the rotation parameter  $a/\ell$  affects both the frequency and wave-vector of the pole-skipping points.<sup>62</sup> At the special value  $a/\ell = \sqrt{2/3} = v_B^{(0)}$ , i.e. the boost speed is equivalent to the conformal butterfly velocity, the pole-skipping point associated with  $(\omega, \mathcal{K}) = (\omega_+, ik_+)$  crosses over into the lower half plane of the complex frequency plane (which has been highlighted in the figure with a cross).

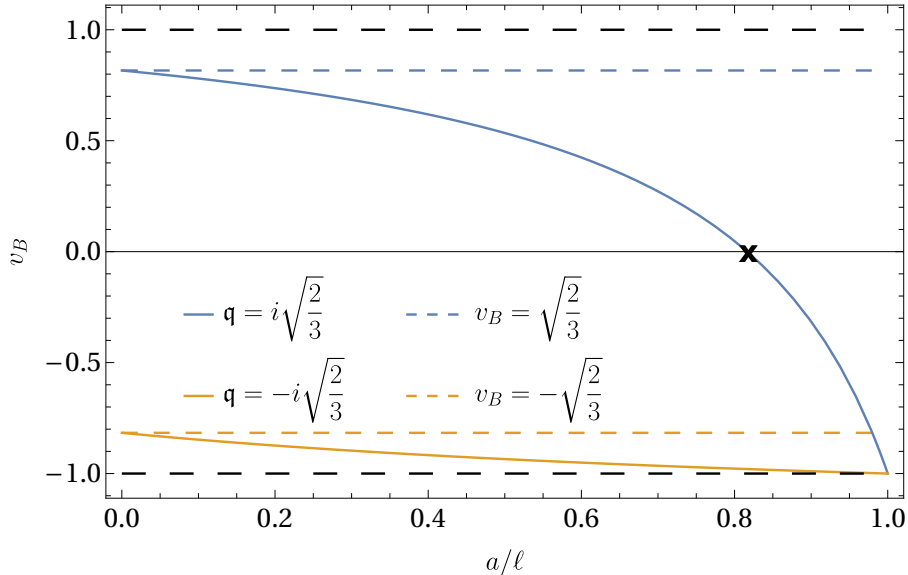


Figure 16: *Butterfly velocity in a rotating plasma.* The butterfly velocities  $v_B^\pm$  given in (169) are displayed as a function of the rotation parameter  $a/\ell$ . The colored dashed lines indicate the conformal value  $v_B^{(0)} = \pm\sqrt{2/3}$  whilst the black dashed lines indicate the speed of light. Notice that the “upstream” butterfly velocity  $v_B^+$  crosses zero at exactly the same value of rotation  $a/\ell = \sqrt{2/3}$  for which the pole-skipping point plotted in Fig. 15 ceases to be located in the upper half complex frequency plane. Adapted from [33].

The fact that the pole-skipping point  $(\omega, \mathcal{K}) = (\omega_+, ik_+)$  enters the lower half complex frequency plane when the boost associated to rotation exceeds  $v_B^{(0)}$  has an interesting implication for the associated butterfly velocity. Extracting a butterfly velocity from the pole-skipping locations (or equivalently through the OTOC profile in Eq. (154) by  $\omega_\pm/k_\pm = v_B^\pm$  we obtain

$$v_B^\pm = \frac{v_B^{(0)} \mp \frac{a}{\ell}}{1 \mp v_B^{(0)} \frac{a}{\ell}}, \quad (169)$$

which, as expected, is nothing but relativistic addition of velocities obtained by applying a boost with speed  $a/\ell$  parallel to  $\pm v_B^{(0)}$ .<sup>63</sup> Eq. (169) shows that the butterfly velocity  $v_B^+$  vanishes at the angular momentum parameter  $a/\ell = v_B^{(0)}$ . At the same value of  $a/\ell$  the

<sup>62</sup>This is in contrast to static planar BHs for which only the wave-vector changes as one varies microscopic parameters at a fixed temperature (e.g. as in the general results of [49, 48] and the Reissner-Nordstrom-AdS geometry of [146])

<sup>63</sup>This was also noted independently by Navid Abbasi in a private communication to some of the authors.

pole-skipping point  $(\omega, \mathcal{K}) = (\omega_+, ik_+)$  passes into the lower half of the complex frequency plane, as is marked in Fig. 16 by the cross.

This phenomenon of vanishing butterfly velocity is quite natural, since a perturbation traveling upstream against a uniform fluid flow in a conformal theory will be experienced by a co-moving observer as sitting still exactly when the perturbation has the speed  $|a/\ell|$ . Thus, a perturbation moving at the conformal butterfly speed  $v_B^{(0)}$  appears to sit still when the fluid streams with velocity  $|a/\ell| = v_B^{(0)}$ . When the fluid flows faster,  $|a/\ell| > v_B^{(0)}$ , this perturbation is dragged downstream.

Although natural, this phenomenon could not be observed in previous studies of OTOCs and pole-skipping in rotating BHs. For instance, in the BTZ BH case [140, 84] the butterfly velocity is equal to the speed of light, while in the Kerr-AdS case [142] the authors were restricted to the slowly rotating limit, a limit in which the rotation speed was parametrically smaller than the corresponding conformal butterfly velocity.

## 5. Summaries, discussion, and outlook

### 5.1. Summary of previously published results

In this article we reviewed [29, 32, 33]. These works made use of the (4+1)-dimensional MP BHs in asymptotically AdS spacetime with two equal angular momenta. These five-dimensional rotating BHs were already discussed as holographic duals for vortical plasmas to compare with heavy ion experiments [36]. With this holographic approach, an analytical vortical fluid flow solving the ideal relativistic fluid dynamics equations of motion was also constructed [36].

*Summary of previous results on QNMs:* In [29] (reviewed in Sec. 4.2.1), the primary subject of analysis was focused on the large temperature (BH) limit. This limit (see Eqs. (112) and (113)) was taken directly on the level of the equations of motion, and was defined by a rescaling of the holographic coordinate and also the frequency and momentum such that only small frequency and momentum (relative to the temperature scale) remained.

In the large temperature limit, there exist analytic results for the hydrodynamic dispersion relations and transport coefficients of the holographic rotating plasma as a function of the values of these transport coefficients in a plasma at rest [29]. Such analytic expressions are provided for the two shear viscosities (Eqs. (114) and (115)), the longitudinal momentum diffusion coefficient (Eq. (117)), two speeds of sound (Eqs. (118) and (116)), and two sound attenuation coefficients (Eq. (119)). The shear viscosity to entropy density ratio varies between zero and  $1/(4\pi)$  depending on the direction of the shear. More generally, in any holographic anisotropic fluid the value of shear viscosity can vary depending on the direction of the shear relative to the anisotropy [121, 122, 123, 29]. There is no lower bound [124] on the shear viscosity to entropy density ratio for the longitudinal shear viscosity. The lack of a bound and the direction-dependence of the shear viscosity can have a strong impact on the QGP physics since the QGP plasma is anisotropic [147]; this strongly anisotropic shear viscosity should be taken into account in hydrodynamic models of the QGP.

At vanishing rotation,  $a = 0$ , the longitudinal shear viscosity  $\eta_{||}$  (along the rotation axis), the longitudinal momentum diffusion coefficient  $D_{||}$ , and the two sound attenuations

$\Gamma_{\pm}$  satisfy the known (Einstein) relations:  $D_{\parallel} \propto \eta_{\parallel}$  and  $\Gamma_{\parallel} \propto \eta_{\parallel}$ . At nonzero rotation,  $a \neq 0$ , known relations between these coefficients are generalized to include dependence on angular momentum.

It is important to note that the results of this section indicate that equal angular momenta MP BHs in the large BH limit are perturbatively stable below the extremal limit  $a = \ell$  for all angular momenta tested.

Thus, the QNMs of rotating MP BHs in the large BH limit were found to behave like hydrodynamic modes of a boosted fluid, and the angular momentum parameter  $a$  acts as boost parameter (see the discussion in Sec. 4.2.6).

*Summary of previous results on critical points:* In [32] (reviewed in Sec. 4.3), the primary subject of analysis was the general behavior of collective excitations around a rotating equilibrium state, and in particular, the extent to which the theory describing these collective (hydrodynamic) excitations remains valid. These excitations are characterized by dispersion relations and here we reviewed the description of these in terms of complex implicit functions referred to as spectral curves. We reviewed the advances made in [39] that allow one to see under what circumstances does a local description of the spectral curves exist, which in general is given by a Puiseux series (which is precisely a dispersion relation). In particular, the radius of convergence of this series expression can be determined by the location of the critical point nearest to the point of expansion. As the interest is in hydrodynamic expressions for which  $\lim_{q \rightarrow 0} w(q) = 0$ , the task is to seek the critical point nearest to the origin of the complex frequency and momentum plane,  $\mathbb{C}^2$ . This technology was applied to the equal angular momenta MP BH, in both the large BH limit and in general.

**Large BH limit** (at large temperature): The sectors which display hydrodynamic behaviors decouple, hence the vector and scalar sectors do not interact with each other nor with the tensor sector. This leads to a simple case of two curves indicated by the hollow square and circle (for the sound and shear diffusion sectors respectively) in Fig. 13 as a function of the angular momentum parameter  $a$ . Here we see a dip in the radius of convergence as the angular momentum is increased before an eventual rise as the extremal limit,  $a = \ell$ , is approached. Importantly, keeping in mind the main lesson discussed in Sec. 2.3.2, in this limit the fluctuations see a uniformly boosted fluid and here the angular momentum parameter  $a$  can be viewed as a velocity of the boost. This is further supported by the fact that one can transform the equations of motion the bulk metric fluctuations satisfy into that of a static black brane (through a boost coordinate transformation).

**General  $r_H^+$**  (general temperature): Away from the large BH limit, the sectors which display hydrodynamic behaviors interact. This is a general effect in MP BH and is due to the eigenfunction decomposition on  $S^3$ . Hence the vector and scalar sectors interact with each other and with the tensor sector also. In particular, the vector or shear diffusion modes interact with the tensor sector. Scalar or sound modes interact with both the shear diffusion sector and the tensor sector. It turns out that this is the effect which most severely limits the radius of convergence. This is displayed by the solid symbols in Fig. 13 (again square and circle for shear diffusion and sound respectively.) The inter-sector coupling leads to the piecewise behavior of the solid-shaped curve. Meanwhile, using the full equations of motion at finite radii has relatively little effect on the locations



of the critical points as displayed in Fig. 14.

Despite differences between the large BH limit and the case of general horizon radius  $r_H^+$ , the main message is clear: the radius of convergence of the linearized hydrodynamic expansion of dispersion relations in  $\mathcal{N} = 4$  SYM remains non-zero under rotation.

*Summary of previous results on pole-skipping:* In [33] (reviewed in Sec. 4.4), the primary subject of analysis was focused on pole-skipping points, defined as points  $(q_*, \omega_*)$  in the complex frequency and momentum space where the Green's function becomes ill defined, as its numerator and denominator vanish simultaneously. In maximally chaotic systems, the location of the pole-skipping points is directly related to the Lyapunov exponent and butterfly velocity which describe the growth of OTOCs. Furthermore, these pole-skipping points exist in the energy-energy correlation functions and hence link the early time chaotic dynamics of the system to the late time hydrodynamic evolution of its conserved charges.

**General  $r_H^+$  (general temperature):** Specifically, OTOCs in the field theory state dual to the equal angular momenta MP black hole are computed by directly calculating gravitational scattering amplitudes for two particles traveling near the event horizon. There, one obtains the eikonal phase associated with two-to-two scattering in terms of the profile characterizing the gravitational backreaction of the particles on the MP BH. Furthermore, one obtains an exact solution for the angular profile of the shockwave in terms of Wigner D-functions. In addition, the linearized fluctuations of the time-time component of the metric were separately computed; these are the relevant metric fluctuation to describe energy-energy correlations of the energy-momentum tensor of associated dual SYM fluid. One finds precisely the same differential equation governs the linearized Einstein equations as that governs the scattering of two particles near the horizon, and thus one expects pole-skipping to occur.

**Large BH limit (at large temperature):** Although an analytic expression for the OTOC was obtained, it was not possible to evaluate the required summations in general. However, in the large BH limit the expression can be approximated by integral representations leading to an exact expression for the shockwave equation. Then the Lyapunov and butterfly velocity were extracted from the exponentially growing behavior. Crucially, these extracted values were compared to the large BH limit of the equation governing the linearized fluctuations of the time-time component of the metric. The locations where this differential equation admits an additional infalling solution (a particular complex value of the momentum and frequency) agrees exactly with the wave vectors of the OTOCs. Furthermore, in the large BH limit, it was also demonstrated numerically that the hydrodynamic dispersion relations (obtained from QNMs) of the scalar channel (associated with energy-energy correlations) pass precisely through the pole-skipping location when evaluated at complex momentum; see Fig. 15. Hence in the large BH limit, one can confidently claim a deep connection between the early time chaotic dynamics and the late time hydrodynamic evolution in  $\mathcal{N} = 4$  SYM evaluated in a rotating state. Finally, as we have emphasized before, in this limit the fluctuations see a uniformly boosted fluid and here the angular momentum parameter  $a$  can be viewed as the velocity of the boost.

Hence, in this limit the butterfly velocity can be extracted, see Fig. 16, and its behavior can be intuitively understood. Interestingly a perturbation traveling upstream against this fluid flow will be experienced by an observer at rest as sitting still exactly when the perturbation has the speed  $|a/\ell|$ . Therefore a perturbation moving at the conformal butterfly speed  $\sqrt{2/3}$  appears to sit still when the fluid streams with velocity  $|a/\ell| = \sqrt{2/3}$ . However if the fluid flows faster, at a speed of  $|a/\ell| > \sqrt{2/3}$ , this perturbation will be dragged downstream.

Precisely the same differential equation governs the linearized Einstein equations as the one that governs the scattering of two particles near the horizon. This statement holds true for a holographic fluid undergoing rotation. In the large BH (large temperature) limit, a pole-skipping point is located on the sound dispersion relation for each value of angular momentum, for the large BH limit see dashed black curve in Fig. 15, providing a link of quantum chaos to hydrodynamics. There exists a special value for the angular momentum,  $a/\ell = \sqrt{2/3}$ , at which the “upstream” butterfly velocity  $v_B^+$  crosses zero and simultaneously the pole-skipping point crosses from the upper to lower half of the complex frequency plane, see Fig. 15.

## 5.2. Summary of new results first presented in this review

In this section we summarize new results and insights obtained in the course of writing this review, which allows us to paint a more complete picture of the fluid dual to the rotating MP BH.

**General  $r_H^+$**  (general temperature):

- Hydrodynamic dispersion relations with modified transport coefficients are a good fit already at small to intermediate temperatures (corresponding to a horizon radius  $r_+/\ell \approx 10^4$ , and possibly even smaller), as can be seen in Fig. 11.
- There is a remarkable window of horizon values in the range of  $1000 \lesssim r_+/\ell \lesssim 10^7$ , in which these holographic rotating fluids display hydrodynamic behavior that is distinct from a boosted fluid. This window is discussed in Sec. 4.2.6.
- Multiple *level crossings* occur between distinct non-hydrodynamic modes, as illustrated in Fig. 7.
- At small temperature corresponding to horizon radius  $r_+/\ell = 10$ , the lowest few hydrodynamic and non-hydrodynamic modes are computed for the tensor (Fig. 6), vector (Fig. 8), and scalar (Fig. 9) sectors.
- At *extremality* when the inner and outer horizons coincide, the surface gravity, and hence the Hawking temperature vanish, and the holographic fluids we consider display a similarity with charged fluids. Consider a state of fixed energy comprised of rotational and thermal energy. When all the energy is rotational and the temperature vanishes, the zero momentum eigenmodes appear to coalesce, forming a branch cut along the imaginary axis similar to what is observed in charged holographic fluids [130, 131, 128]; see bottom graphs ( $a/\ell = 0.9$ ) in Figs. 6, 8, and 9.

- At small temperature corresponding to horizon radius  $r_+ = \ell$ , the fluid becomes unstable at smaller angular momentum, as superradiance occurs below extremality (i.e. below rotational parameter  $a = \ell$ ) at  $a/a_{\text{ext}} \sim 0.916$  as displayed in Fig. 12.

**Large BH limit** (at large temperature):

- Fluid is nontrivially rotating, low-energy (hydrodynamic) excitations *see* it as a fluid boosted with velocity  $a$ , this is discussed in Sec. 4.2.1.
- Hydrodynamic dispersion relations with boosted fluid transport coefficients are given by eqs. (114) to (121).
- Eikonal limit (large momentum limit): eigenfrequencies scale with the momentum as expected, as displayed in Fig. 5.
- Superradiance instabilities occur only at extremality,  $a = \ell$ , while the fluid is stable (according to our numerical checks) against all fluctuations at  $a < \ell$ .

Hydrodynamic behavior emerges in the holographic rotating fluids already at moderate temperatures (intermediate sized black holes,  $r_+ \approx 10^2$ ) as noted before [29]; see Sec. 4.2.6 for the details on our novel results first presented in this review.

Fluctuations of the hydrodynamic fields (temperature, fluid velocity) were holographically computed and their spectrum of eigenmodes was determined. Already at fairly low temperatures, the spectrum of this fluid contains modes which have vanishing frequency in the limit of vanishing momentum eigenvalue, a defining property of hydrodynamic modes. Furthermore, the frequencies of these candidate hydrodynamic mode scale with the (angular) momentum of the fluctuations either linearly or quadratically, closely resembling the linear scaling of sound modes with the speed of sound and the quadratic damping of diffusion modes. Notably, the momentum of the fluctuations is now a discrete angular momentum eigenvalue because the rotating fluid enforces an expansion into eigenmodes that resemble spherical harmonics, which have discrete angular momentum eigenvalues labelled by  $\mathcal{J}$ .

Our analysis here goes beyond [29] in that we present non-hydrodynamic modes along with hydrodynamic modes. Extending [29] even further, we present results at moderate to low temperatures (corresponding to medium to small BH horizon radii). At such low temperatures, even the lowest energy eigenmodes may not behave hydrodynamically, in that their dispersion relations deviate from hydrodynamic scaling. These results demonstrate how the hydrodynamic scaling of the lowest lying eigenfrequencies with angular momentum emerges as the temperature increases.<sup>64</sup> Furthermore, non-hydrodynamic modes are responding strongly to the coupling of modes in the scalar and vector sectors. This is seen in the level crossing in Fig. 7.

We studied the regime of large momentum values  $\mathcal{J}$  and large frequencies  $\nu$ , beyond the naive regime of validity of hydrodynamics, and found that the hydrodynamic momentum diffusion mode dominating the low energy dynamics in the entire range of momentum

---

<sup>64</sup>For a similar analysis of the validity of hydrodynamics in a holographic system subject to a strong magnetic field, see [148].

$j = 0, \dots, 10$  for all values of  $a$  scanned. As can be seen in Fig. 8, it is obvious that the diffusion mode originating at zero frequency  $\nu = 0$  with momentum  $\mathcal{J} = 0$  (marked by triangle) always has the smallest imaginary part, i.e. the smallest damping, and thus it is the longest lived mode dominating the late time low energy dynamics. In the case of the two sound modes, the behavior is more complicated, as displayed in Fig. 9. However, at least one of the two sound modes is dominating the low energy late time dynamics for all values of  $a$  and  $\mathcal{J}$  scanned (very similar to the diffusion mode described above). The other sound mode becomes, at a specific momentum value  $\mathcal{J}$ , more damped than the lowest-lying non-hydrodynamic modes, leading to a change in the late-time transport properties of the fluid, as seen also at vanishing rotation. There is a third hydrodynamic mode appearing in Fig. 9 marked by the triangle at  $\mathcal{J} = 0, \nu = 0$ . This is the momentum diffusion mode that mixes with the sound modes at finite values of the horizon radius  $r_+$  (moderate to small temperatures).

It has been suggested in [98] that the relative angular velocities of the BH to that of the boundary are conjugate to the angular momenta of the dual boundary fluid. In this context, angular velocity can be considered as a gauge field, with the physical angular momentum being the difference in angular velocity between the boundary and the horizon (see Eq. (19) in Sec. 3.1 for a concrete example). Thus, holographic angular velocity is analogous to a  $U(1)$ -charge chemical potential, which is defined as the difference of the time-component of the gauge field at the boundary minus its value at the BH horizon,  $\mu = \int_{r_{\text{horizon}}}^{r_{\text{boundary}}} dr A_t'(r)$ , with the radial AdS-direction  $r$ . We point out that there are various similarities between the QNM spectra of rotating MP BHs studied in the present article and the QNM spectra charged Reissner-Nordström black branes studied in [128]. Most striking is the occurrence of a set of “purely imaginary QNMs” at nonzero rotation or charge parameter, respectively. These modes at large rotation or charge parameter coalesce and appear to form a branch cut along the negative imaginary frequency axis as the BHs approach extremality, as studied in the lower dimensional  $AdS_4$  Reissner-Nordström case [130, 131].

### 5.3. Discussion and implications

Holography has proven itself a fertile ground for the investigation, and construction of effective descriptions for quantum many-body systems. The most famous example of the correspondence, between the strong coupling regime of  $\mathcal{N} = 4$  SYM theory and Einstein gravity in  $AdS_5 \times S^5$ , in particular has generated a significant body of literature devoted to furthering the understanding strongly coupled QFT. These endeavours have often aided understanding in both nuclear physics and heavy ion collisions by providing microscopic inputs, such as transport coefficients, unattainable by other means. Yet despite this extensive literature, rotational phases of  $\mathcal{N} = 4$  SYM have received scant notice. In this article we have reviewed recent progress in the direction of understanding the behavior of  $\mathcal{N} = 4$  SYM theory in rotating states. Considering the equal angular momenta limit of the simplest dual description, the MP BH, the works we have reviewed provide a new foothold into studying the collective excitations around thermal equilibrium of rotating, strongly-coupled  $\mathcal{N} = 4$  SYM fluids. The most important lesson learned from the analysis is perhaps simple in retrospect:

Collective excitations around rotating states whose frequency and momentum are small relative to the temperature and angular momentum scale perceive the rotating fluid at their relative scales as a boosted fluid. Corrections to this behavior are suppressed by powers of the temperature.

That is, the collective excitations behave ultra-locally [50] and, barring any non-trivial solitonic field configurations, the ultra-local behavior of any fluid flow is uniform motion. This result is vividly demonstrated in not only the hydrodynamic modes obtained here (see Secs. 3.3.2, 4.2.1 and 4.3) but in the ballistic growth of local operators characterized by the Lyanpunov exponents and butterfly velocities of Sec. 4.4.2.

More generally, this result that rotating systems such as the QGP generated in heavy-ion collisions may at intermediate to high temperatures be well approximated by models of boosted fluids. However, caution should be used, as this review discussed holographic fluids (not QCD plasma) dual to a particular geometry (rotating MP BHs with two equal angular momenta) and then stereographically projected onto flat Minkowski space. The MP BHs with equal angular momenta,  $a = b$  are peculiar for several reasons. One striking example of such peculiarities is that there is no axis of rotation. This can be seen by calculating the integral curves of the axial angular momentum Killing vector field. The resulting flow lines for an embedding in  $\mathbb{R}^3$  lie on a torus. On the dual field theory side, the induced rotation also lacks an axis.

The lowest critical points diverging to infinity is in agreement with the “unreasonable success of viscous hydrodynamics” in applications of QPG transport [64]. The more vorticity is added to a strongly coupled fluid, the larger the momentum the hydrodynamic expansion can reach. This could have implications for regimes of validity of effective field theories in experiments to probe fundamental physics, which require large momenta to probe. Other than QGP, this enhancement of hydrodynamics could be applied to other extreme rotating scenarios like neutron stars, stellar objects, and astrophysical black holes.

The analytically known vortical fluid flow (102) (BIR flow) [36] can certainly serve as an analytical model for rotating QGP, similar to how Bjorken flow or Gubser flow are used. Furthermore, the MP BHs discussed in this review that are dual to this vortical fluid flow, can serve as the dual gravitational description of such rotating states. It would be useful to use this holographic model and the analytic BIR flow as checks for hydrodynamic codes and other numerical or analytical descriptions of rotating fluids.

#### 5.4. Outlook

The results discussed above suggest that there is much more to learn for hydrodynamics in rotating systems, and for gravity from the rotating five-dimensional BH solution to the Einstein equations. Here we discuss some future directions; the list is of course not exhaustive.

1. The general case with unequal angular momenta  $J_\phi \neq J_\psi$  ( $a \neq b$ ) or the singly spinning configurations  $J_\phi \neq 0, J_\psi = 0$  and  $J_\phi = 0, J_\psi \neq 0$  could be explored.
  - (i) The singly spinning case contains an axis of rotation, so large temperature expansions around such a state would be interesting.
  - (ii) Both cases involve solving 2D partial differential equations in order to find the QNMs.

2. Explore the intermediate horizon radius regime around  $10^3 < r_+ < 10^7$  in which nontrivial hydrodynamic transport is expected (which is not simply that of a boosted fluid, as argued in Sec. 4.2.6).
3. What is the physical relevance of the level crossings between non-hydrodynamic modes as seen in Fig. 7? Are these crossing points related to the level crossings and mode collisions determining critical points at complexified momentum [39, 149]?
4. Only a subset of fluctuations was explored in this article, namely the ones that reduce in the large BH limit to the fluctuations with linear momentum aligned with the anisotropy created in the fluid due to its rotation. More general fluctuations should be considered, which would for example allow one to compute the perpendicular diffusion coefficient  $\mathcal{D}_\perp$ .
5. The presence of a linear instability in global AdS Kerr begs the question of what the dual field theoretic interpretation to this instability is.
6. An implementation of rotation, polarization and spin in hydrodynamic codes is desirable for various applications ranging from modelling heavy-ion collisions [64], modelling mergers of BHs and neutron stars [150, 151], and fluids in the context of condensed matter physics, e.g. [152, 153, 154, 155]. The holographic fluid presented in this article (as well as the analytic BIR flow [36]) can serve as a testing ground for such hydrodynamic codes.
7. A version of hydrodynamics around a rotating equilibrium state can be systematically constructed. This state breaks rotation invariance and thus involves a new vector, the unit vector pointing in the symmetry direction, similar to anisotropic hydrodynamics [125, 126, 156]). The fluid/gravity correspondence [50] can be used to systematically derive and test such a description. It can be used to extend the rotating BH solutions (31) into metric solutions which have temperature and angular momentum depending on the transverse coordinates and time. This leads to a gradient expansion in the dual field theory, locally correcting the rotating equilibrium state by gradients of temperature and angular momentum, likely modifying the hydrodynamic dispersion relations significantly.

It is worthwhile to point out the possibility that the QGP generated in heavy-ion collisions does *not* actually carry any significant vorticity or angular momentum. A recent numerical study of a holographic fluid created in the collision of localized, lumpy shocks (modeling a granular nuclear structure) has found that most of the angular momentum after the collision resides in the periphery, while only a small fraction of the total angular momentum is present in the region occupied by the holographic QGP [157]. If the same proves to be true for QGP generated at RHIC and LHC, then the hyperon polarization would have no explanation from the QGP containing a significant amount of vorticity or angular momentum, and new theoretical understanding has to be found.

## Acknowledgement

C.C., M.A. and M.K. acknowledge the excellent discussions and collaborations with Jorge Noronha, Enrico Speranza, Mike Blake and Anthony Thompson, on which part of this work is based. This work was supported, in part, by the U.S. Department of Energy grant DE-SC0012447. C.C. was supported in part, by the Netherlands Organisation for Scientific Research (NWO) under the VICI grant VI.C.202.104. M.A. was supported by Henan University's Postdoctoral Program and by the *Japan Society for the Promotion*

of Science Postdoctoral Fellowship for Research in Japan (Short-term) in the creation of this work.

## Appendix A. Energy-Momentum tensor

In this appendix we display the full form of the energy-momentum tensor for the MP BH with  $a \neq b$ :

$$8\pi G_5 \langle T_{tt} \rangle = \frac{1}{64\ell^3} \left[ 13a^4 + 15(a^2 - b^2)^2 \cos(4\theta_{FG}) \right. \\ \left. + 4(a^2 - b^2) \cos(2\theta_{FG}) (a^2 + b^2 - 14\ell^2) \right. \\ \left. - 34a^2b^2 - 8a^2\ell^2 + 13b^4 - 8b^2\ell^2 + 192M\ell^2 + 24\ell^4 \right] \quad (\text{A.1})$$

$$8\pi G_5 \langle T_{t\phi} \rangle = -\frac{a \sin(\theta_{FG})^2}{8\ell(\ell^2 - a^2)} \left[ 3a^4 + 7(a^2 - b^2)^2 \cos^4(\theta_{FG}) \right. \\ \left. - 2(a^2 - b^2) \cos(\theta_{FG})^2 (5a^2 - 6b^2 + \ell^2) \right. \\ \left. + a^2(2\ell^2 - 8b^2) + 4b^4 + 24M\ell^2 - \ell^4 \right] \quad (\text{A.2})$$

$$8\pi G_5 \langle T_{t\psi} \rangle = -\frac{b \cos^2(\theta_{FG})}{8\ell(\ell^2 - b^2)} \left[ -a^4 + 7(a^2 - b^2)^2 \cos^4(\theta_{FG}) \right. \\ \left. - 2(a^2 - b^2) \cos^2(\theta_{FG}) (a^2 - 2b^2 + \ell^2) \right. \\ \left. + 2a^2\ell^2 + 24M\ell^2 - \ell^4 \right] \quad (\text{A.3})$$

$$8\pi G_5 \langle T_{\theta_{FG}\theta_{FG}} \rangle = \frac{1}{8\Delta_\theta \ell} \left[ a^4 - 3(a^2 - b^2)^2 \cos(\theta_{FG})^4 \right. \\ \left. + 2(a^2 - b^2)(a^2 - 2b^2 + \ell^2) \cos(\theta_{FG})^2 - 2\ell^2(a^2 - 4M) + \ell^4 \right] \quad (\text{A.4})$$

$$8\pi G_5 \langle T_{\phi\phi} \rangle = \frac{\ell \sin^2(\theta_{FG})}{8(a^2 - \ell^2)^2} \left\{ 3a^6 - a^4(8b^2 + \ell^2) + a^2(4b^4 + 8\ell^2(b^2 + 3M) - 3\ell^4) \right. \\ \left. - 2\cos(\theta_{FG})^2 [5a^6 - 11a^4b^2 + 6a^2b^4 + \ell^4(b^2 - a^2) \right. \\ \left. + 2\ell^2(-2a^4 + a^2(5b^2 + 8M) - 3b^4)] \right. \\ \left. + 7(a^2 - b^2)^2(a^2 - \ell^2) \cos(\theta_{FG})^4 - 4b^4\ell^2 + 8M\ell^4 + \ell^6 \right\} \quad (\text{A.5})$$

$$8\pi G_5 \langle T_{\phi\psi} \rangle = \frac{abM\ell^3 \sin^2(2\theta_{FG})}{(a^2 - \ell^2)(b^2 - \ell^2)} \quad (\text{A.6})$$

$$8\pi G_5 \langle T_{\psi\psi} \rangle = \frac{\ell \cos(\theta_{FG})^2}{8(b^2 - \ell^2)^2} \left\{ 2\cos(\theta_{FG})^2 \left[ \ell^2(a^4 - 4a^2b^2 + 3b^4 + 16b^2M) \right. \right. \\ \left. \left. - b^2(a^4 - 3a^2b^2 + 2b^4) + \ell^4(a^2 - b^2) \right] \right. \\ \left. - (b^2 - \ell^2)(a^4 - 2\ell^2(a^2 - 4M) + \ell^4) \right. \\ \left. + 7(a^2 - b^2)^4(b^2 - \ell^2) \cos(\theta_{FG})^4 \right\} \quad (\text{A.7})$$

Note that all other elements of the energy-momentum tensor which are not shown, and are not given by symmetry, vanish.

## Appendix B. Quasinormal mode data

For convenience we include the six modes closest to the line  $\Im(\nu) = 0$  in the three sectors discussed in Sec.4.2 for  $a/\ell = 0, 1/2, 9/10$ . In each table we fix a value of  $\mathcal{J} = 0, 1/2, 1$  and  $r_+ = 10$ , the remaining data can be found in the supplementary material.

### Appendix B.1. Tensor sector

n	$a/\ell = 0$		$a/\ell = 1/2$		$a/\ell = 9/10$	
	$\Re(\nu)$	$\Im(\nu)$	$\Re(\nu)$	$\Im(\nu)$	$\Re(\nu)$	$\Im(\nu)$
1	1.57792	-1.36943	1.83839	-1.73479	-0.214354	-0.529707
2	-1.57792	-1.36943	-1.63407	-1.73893	-0.223526	-1.00114
3	2.60488	-2.37904	-0.471547	-1.94296	-0.231857	-1.4879
4	-2.60488	-2.37904	-2.90868	-2.98463	-0.239585	-1.98766
5	-3.61756	-3.38252	3.08986	-2.98592	-0.246234	-2.49843
6	3.61756	-3.38252	-4.14395	-4.21689	2.84375	-2.73946

Table B.1:  $\mathcal{J} = 0$  tensor modes.  $n$  indicates the  $n$ th furthest mode from the  $\Im(\nu) = 0$  axis.

n	$a/\ell = 0$		$a/\ell = 1/2$		$a/\ell = 9/10$	
	$\Re(\nu)$	$\Im(\nu)$	$\Re(\nu)$	$\Im(\nu)$	$\Re(\nu)$	$\Im(\nu)$
1	-1.58609	-1.36696	1.86324	-1.73367	-0.267892	-0.52861
2	1.58609	-1.36696	-1.6031	-1.74128	-0.279378	-1.00015
3	2.6107	-2.3774	-0.594678	-1.92682	-0.289814	-1.48695
4	-2.6107	-2.3774	-2.88713	-2.98347	-0.299508	-1.98678
5	3.62224	-3.38124	3.1134	-2.98514	-0.307855	-2.49776
6	-3.62224	-3.38124	-4.12207	-4.21626	-2.62293	-2.73856

Table B.2:  $\mathcal{J} = 1/2$  tensor modes.  $n$  indicates the  $n$ th furthest mode from the  $\Im(\nu) = 0$  axis.

n	$a/\ell = 0$		$a/\ell = 1/2$		$a/\ell = 9/10$	
	$\Re(\nu)$	$\Im(\nu)$	$\Re(\nu)$	$\Im(\nu)$	$\Re(\nu)$	$\Im(\nu)$
1	-1.5965	-1.36383	1.88859	-1.73202	-0.321408	-0.527454
2	1.5965	-1.36383	-1.56789	-1.74515	-0.335217	-0.999071
3	2.61814	-2.37531	-0.722979	-1.90682	-0.347771	-1.48588
4	-2.61814	-2.37531	-2.86612	-2.98187	-0.359452	-1.9858
5	-3.62822	-3.37959	3.13731	-2.984	-0.369518	-2.49702
6	3.62822	-3.37959	-4.10043	-4.21535	-2.59952	-2.73727

Table B.3:  $\mathcal{J} = 1$  tensor modes.  $n$  indicates the  $n$ th furthest mode from the  $\Im(\nu) = 0$  axis.



Appendix B.2. Vector sector

n	$a/\ell = 0$		$a/\ell = 1/2$		$a/\ell = 9/10$	
	$\Re(v)$	$\Im(v)$	$\Re(v)$	$\Im(v)$	$\Re(v)$	$\Im(v)$
1	1.57792	-1.36943	1.83839	-1.73479	-0.214354	-0.529707
2	-1.57792	-1.36943	-1.63407	-1.73893	-0.223526	-1.00114
3	2.60488	-2.37904	-0.471547	-1.94296	-0.231857	-1.4879
4	-2.60488	-2.37904	-2.90868	-2.98463	-0.239585	-1.98766
5	-3.61756	-3.38252	3.08986	-2.98592	-0.246234	-2.49843
6	3.61756	-3.38252	-4.14395	-4.21689	2.84375	-2.73946

Table B.4:  $\mathcal{J} = 0$  vector modes.  $n$  indicates the  $n$ th furthest mode from the  $\Im(\nu) = 0$  axis.

n	$a/\ell = 0$		$a/\ell = 1/2$		$a/\ell = 9/10$	
	$\Re(v)$	$\Im(v)$	$\Re(v)$	$\Im(v)$	$\Re(v)$	$\Im(v)$
1	$-9.77489 \times 10^{-85}$	-0.00626198	-0.0252699	-0.00514204	-0.045346	-0.00226457
2	-1.58609	-1.36696	-1.46214	-1.42053	-0.160298	-0.532138
3	1.58609	-1.36696	1.59728	-1.4975	-0.241578	-0.716389
4	-1.57145	-1.37138	1.81681	-1.7323	-0.167453	-1.00312
5	1.57145	-1.37138	-1.66563	-1.73445	-0.202738	-1.2898
6	-2.6107	-2.3774	-0.350175	-1.96503	-0.173784	-1.48965

Table B.5:  $\mathcal{J} = 1/2$  vector modes.  $n$  indicates the  $n$ th furthest mode from the  $\Im(\nu) = 0$  axis.

n	$a/\ell = 0$		$a/\ell = 1/2$		$a/\ell = 9/10$	
	$\Re(v)$	$\Im(v)$	$\Re(v)$	$\Im(v)$	$\Re(v)$	$\Im(v)$
1	$-6.3260 \times 10^{-94}$	-0.0150693	-0.0508062	-0.0119096	-0.090775	-0.00472503
2	-1.5965	-1.36383	-1.45984	-1.4059	-0.213379	-0.532508
3	1.5965	-1.36383	1.6058	-1.49884	-0.297615	-0.713923
4	-1.57556	-1.37012	1.84404	-1.729	-0.223126	-1.00332
5	1.57556	-1.37012	-1.64015	-1.73249	-0.262902	-1.28889
6	2.61814	-2.37531	-0.468888	-1.96172	-0.23164	-1.48972

Table B.6:  $\mathcal{J} = 1$  vector modes.  $n$  indicates the  $n$ th furthest mode from the  $\Im(\nu) = 0$  axis.

Appendix B.3. Scalar sector

n	$a/\ell = 0$		$a/\ell = 1/2$		$a/\ell = 9/10$	
	$\Re(v)$	$\Im(v)$	$\Re(v)$	$\Im(v)$	$\Re(v)$	$\Im(v)$
1	-1.5779	-1.3694	-1.4252	-1.3411	-0.0010668	-0.55268
2	1.5779	-1.3694	1.4252	-1.3411	-0.074684	-0.75314
3	-1.5685	-1.3723	-1.4809	-1.4504	0.0	-0.86704
4	1.5685	-1.3723	1.5765	-1.4824	0.0	-0.86704
5	-1.5661	-1.3730	-1.7330	-1.7340	-0.00047209	-1.0449
6	1.5661	-1.3730	1.7332	-1.7366	-1.2191	-1.2125

Table B.7:  $\mathcal{J} = 0$  scalar modes.  $n$  indicates the  $n$ th furthest mode from the  $\Im(v) = 0$  axis.

n	$a/\ell = 0$		$a/\ell = 1/2$		$a/\ell = 9/10$	
	$\Re(v)$	$\Im(v)$	$\Re(v)$	$\Im(v)$	$\Re(v)$	$\Im(v)$
1	0.0	-0.0062620	-0.011386	-0.0060167	-0.036860	-0.0035422
2	-1.5861	-1.3670	-1.4396	-1.3341	-0.053926	-0.55468
3	1.5861	-1.3670	1.4124	-1.3472	-0.13133	-0.75273
4	-1.5714	-1.3714	-1.4762	-1.4403	-0.045112	-0.86704
5	1.5714	-1.3714	1.5848	-1.4869	-0.045112	-0.86704
6	-1.5673	-1.3726	-1.7121	-1.7305	-0.045112	-0.86704

Table B.8:  $\mathcal{J} = 1/2$  scalar modes.  $n$  indicates the  $n$ th furthest mode from the  $\Im(v) = 0$  axis.

n	$a/\ell = 0$		$a/\ell = 1/2$		$a/\ell = 9/10$	
	$\Re(v)$	$\Im(v)$	$\Re(v)$	$\Im(v)$	$\Re(v)$	$\Im(v)$
1	-0.081988	-0.0041527	-0.095984	-0.0014583	-0.099872	-0.00014121
2	0.081988	-0.0041527	0.051356	-0.0070246	0.010573	-0.0044887
3	0.0	-0.015069	-0.028210	-0.014144	-0.074679	-0.0080336
4	-1.5965	-1.3638	-1.4545	-1.3266	-0.10681	-0.55665
5	1.5965	-1.3638	1.3998	-1.3526	-0.18799	-0.75219
6	-1.5756	-1.3701	-1.4733	-1.4284	-0.090225	-0.86704

Table B.9:  $\mathcal{J} = 1$  scalar modes.  $n$  indicates the  $n$ th furthest mode from the  $\Im(v) = 0$  axis.

## Appendix C. Numerical methods

In general, the linearized equations of motion of the fluctuations give rise to what is known as a non-linear eigenvalue problem that takes the form

$$M(\omega, q)\Psi_0 = \left( \sum_{n=0}^R M_n \omega^n \right) \Psi_0 = 0, \quad (\text{C.1})$$

where  $M_n$  are  $\omega$ -independent differential operators,  $\Psi_0$  are the fields of interest in a given sector, and  $R$  is the order of  $\omega$  appearing in the equations of motion. Note  $R$  is at most two because Eq. (24) has second order time derivatives. If more than one field makes up a given sector, say  $m$  of them, then  $M_n$  are  $m \times m$  matrices acting on a column vector of  $m$  fields represented by  $\Psi_0$ . It is well-known how to linearize such a non-linear eigenvalue problem by introducing auxiliary variables,  $\Psi_i = \omega \Psi_{i-1}$ , for  $i = 1, \dots, R-1$ . The original equation, Eq. (C.1), then becomes a set of linear equations

$$\omega \left( \sum_{n=1}^R M_n \Psi_{n-1} \right) = -M_0 \Psi_0, \quad \Psi_i = \omega \Psi_{i-1}, \quad i = 1, \dots, R-1, \quad (\text{C.2})$$

which is now a linear generalized eigenvalue problem. To avoid non-regular behavior of the fields at the horizon, we shall work in the null coordinates discussed in Appendix D.

To proceed, we discretize the resulting equations of motion by decomposing the fields in a truncated Chebyshev basis on a pseudo-spectral grid. Fields in the equations of motion are replaced with vectors of these fields evaluated at the grid points, the coefficients of these fields in the equations of motion become diagonal matrices with diagonal elements the coefficients evaluated at the grid points, and the partial derivatives turn into pseudo-spectral differentiation matrices. Appropriate boundary conditions also have to be imposed, whereby the dynamical equations are required to be regular at the horizon (null coordinates ensure this for us) and are not sourced at the conformal boundary. Finally we can solve the resulting (generically) non-linear eigenvalue problem defined on the pseudo-spectral grid using the **Eigenvalues** function in Mathematica, and these give the frequencies of QNMs.

To ensure convergence, comparison over several orders of grid points should be performed to filter out spurious modes introduced in the spectrum due to the discretization scheme. Physical modes will move only slightly when changing the number of grid points used in the scheme unlike spurious modes. Moreover, the equations of motion contain additional unused equations. Although they are unused, they must also be satisfied by solutions to the equations of motion, hence they act as constraints. By using the **Eigen-system** function in Mathematica, eigenvalues and the corresponding eigenvectors can be obtained in one go. The eigenvectors represent the values of the fields at each of the grid points for a given QNM frequency. Inserting the eigenvector and eigenvalue back into the constraint equations gives a measure of the success of the method. We use the following conservative measure:

Let  $S_i^j$ ,  $i = 1, \dots, c$ , represent the  $c$  constraint equations at each grid point  $j$ . Using a Gauss-Lobatto grid of  $N$  points, we compute (recall there are  $m$  fields)

$$\varsigma = \frac{1}{mN} \sum_{i=1}^c \sum_{j=1}^N |S_i^j|. \quad (\text{C.3})$$

What  $\varsigma$  measures is how much all the constraint equations in sum differ from zero as an average over all grid points. For the tensor sector, there is no constraint, and we can verify that the QNM problem is solved at least to the level of  $10^{-15}$  by directly putting the solution back into the equation. For the vector sector we keep only modes for which  $\varsigma < 10^{-12}$ . The scalar sector is more challenging. There, we are able to find solutions for which  $\varsigma \lesssim 10^{-4}$  for  $r_+ = 10$ ,  $\mathcal{J} = 25$ ,  $a/\ell = 1/2$  and  $N = 20$ . At smaller  $a$  or  $J$ , or near the large BH limit the convergence improves significantly.<sup>65</sup> Work to improve this is underway.

## Appendix D. Null coordinates

### Appendix D.1. Infalling Eddington-Finkelstein coordinates

The calculation of the QNM displayed in Sec.4.2 can be done in any coordinate system. However, a particularly useful coordinate system to choose is one based on a null slicing of the spacetime in which the coordinate induced singularity at the outer horizon radius is removed. The infalling Eddington–Finkelstein like coordinates used in the calculations are defined as follows

$$d\hat{t} = dt + \frac{\sqrt{\beta(r)}}{G(r)} dr, \quad (\text{D.1})$$

$$d\hat{\psi} = d\psi + \frac{2h(r)\sqrt{\beta(r)}}{G(r)} dr, \quad (\text{D.2})$$

$$d\hat{r} = dr, \quad (\text{D.3})$$

where

$$\beta(r) = 1 - \frac{a^2 r_+^4 (r_+^2 + \ell^2)}{r^4 (a^2 r_+^2 + a^2 \ell^2 - r_+^2 \ell^2)}, \quad (\text{D.4})$$

$$h(r) = \frac{a r_+^4 (r_+^2 + \ell^2)}{a^2 (r_+^2 + \ell^2) (r_+^4 - r^4) + r^4 r_+^2 \ell^2}. \quad (\text{D.5})$$

For convenience, we will suppress the hat on  $r$  unless necessary. Making this transformation of coordinates induces a frame transformation

$$\hat{\sigma}^3 = \sigma^3 + \frac{2h(r)\sqrt{\beta(r)}}{G(r)} dr. \quad (\text{D.6})$$

Expressed in terms of the null coordinates and the new frame, the metric given in Eq. (31) now takes the form

$$ds^2 = -\frac{G(r)}{\beta(r)} d\hat{t}^2 + \frac{d\hat{t}dr}{\sqrt{\beta(r)}} + \frac{r^2}{4} ((\sigma^1)^2 + (\sigma^2)^2) + \frac{r^2}{4} \beta(r) (\hat{\sigma}^3 - 2h(r)d\hat{t})^2 \quad (\text{D.7})$$

---

<sup>65</sup>Two independent codes were constructed for the purpose of computing QNMs in this work. One was initially created for the study [29] and did not feature a verification of the constraint violation. The second was created independently by another author of the present work during the preparation of [33, 32], and it was later improved to measure constraint violation. In this work, primary results were obtained using the first code and then independently verified using the second code.

From Eq. D.1 one can construct the dual vectors as the following

$$\begin{aligned}\frac{\partial}{\partial \hat{t}} &= \frac{\partial}{\partial t} \\ \frac{\partial}{\partial \hat{\psi}} &= \frac{\partial}{\partial \psi} \\ \frac{\partial}{\partial \hat{r}} &= \frac{\partial}{\partial r} - \frac{\sqrt{\beta(r)}}{G(r)} \left( \frac{\partial}{\partial t} + 2h(r) \frac{\partial}{\partial \psi} \right)\end{aligned}\tag{D.8}$$

Hence the notation  $d\hat{t}$  and  $d\hat{\psi}$  is justified because their associated vectors' Lie brackets still vanish. Furthermore, the commutation relations in Eq. (44) are preserved.

#### Appendix D.2. Kruskal coordinates

A further set of null coordinates is necessary for the study of the gravitational shock-waves in Sec.4.4, the analogue of Kruskal coordinates. We review the transformation to this coordinate system, the full details can be found in [33]. We begin moving to the co-rotating angular coordinate  $\tilde{\psi}$  and the associated one form  $\tilde{\sigma}_3$  by

$$\tilde{\psi} = \psi - \bar{\Omega}t, \quad \tilde{\sigma}^3 = d\tilde{\psi} + \cos(\theta)d\phi,\tag{D.9}$$

with  $\bar{\Omega} = -2\tilde{\Omega}$  for  $\tilde{\Omega}$  defined in Eq. (39). In the co-rotating coordinates  $(t, r, \tilde{\psi}, \phi, \theta)$  the radial and temporal coordinates  $(t, r)$  take the form

$$ds_{(t,r)}^2 = -F(r)dt^2 + \frac{dr^2}{G(r)},\tag{D.10}$$

where  $F(r)$  is given as

$$F(r) = 1 + \frac{r^2}{\ell^2} - \frac{r_+^2}{r^2} \left( 1 + \frac{r_+^2}{\ell^2} \right) - \frac{a^2 \Sigma^2 (r^4 - r_+^4)}{\ell^4 r^2 r_+^4},\tag{D.11}$$

which vanishes at  $r = r_+$  as expected in co-rotating coordinates. In Eq. (D.11) we have introduced a new parameter  $\Sigma$  defined as

$$\Sigma = \ell^2 + r_+^2.\tag{D.12}$$

As is familiar we can introduce the infalling ( $v$ ) and outgoing ( $u$ ) Eddington=Finkelstein coordinates by

$$dv = dt + \frac{dr}{\sqrt{F(r)G(r)}},\tag{D.13a}$$

$$du = dt - \frac{dr}{\sqrt{F(r)G(r)}}.\tag{D.13b}$$

Finally, define the Kruskal-like coordinates,  $U$  and  $V$

$$U = -e^{-\alpha u}, \quad V = e^{\alpha v},\tag{D.14}$$

where  $\alpha = 2\pi T$ , for which the metric is then given by

$$ds^2 = A(UV)dUdV + B(UV)(UdV - VdU)\tilde{\sigma}^3 + \frac{r^2}{4}((\sigma^1)^2 + (\sigma^2)^2 + (\tilde{\sigma}^3)^2) + \frac{\mu a^2}{2r^2}(\tilde{\sigma}^3)^2.\tag{D.15}$$

The function  $r = r(UV)$  is defined implicitly through (D.14) and

$$A(UV) = \frac{F(r)}{\alpha^2 UV}, \quad B(UV) = \frac{a}{2\alpha UV} \frac{\Sigma(r_+^4 - r^4)}{\ell^2 r^2 r_+^2}. \quad (\text{D.16})$$

The metric (D.15) is manifestly smooth at both the  $U = 0$  and  $V = 0$  horizons at which  $r(0) = r_+$ .

## Appendix E. Hydrodynamic dispersion relations and conventions

In this appendix, the hydrodynamic dispersion relation conventions, expected values for transport coefficients and expected scaling powers are presented in the example of the momentum diffusion channel. At vanishing rotation, in the momentum diffusion channel the lowest of the eigenmodes is the hydrodynamic diffusion mode with the dispersion

$$\omega = -i\mathcal{D}q^2, \quad (\text{E.1})$$

where the frequency  $\omega$  and momentum  $q$  are chosen to agree with the definitions from [38]. In this case,  $\mathcal{N} = 4$  SYM theory has been shown to have  $\mathcal{D} = 1/(4\pi T)$  [120, 124]. This diffusion coefficient is furthermore related to the shear viscosity over entropy ratio as follows (via an Einstein relation):  $\mathcal{D} = \eta/(\epsilon + P) = \frac{1}{T} \frac{\eta}{s} = \frac{1}{T} \frac{1}{4\pi}$ , where we used that  $\mathcal{N} = 4$  SYM has  $\eta/s = 1/(4\pi)$  and that  $\epsilon + P = sT$ .

In this article, we consider different frequency  $\nu = \omega/(2\pi T\ell)$  and momentum  $j = q/(2\pi T\ell)$ . For the rest of this appendix, we assume  $\ell = 1$ , as is done in the main text unless stated otherwise. We also consider rotating states, which will modify the dispersion of the diffusion mode, so for the longitudinal diffusion mode we write

$$\nu = v_{\parallel} j - i\mathcal{D}_{\parallel} j^2 + \mathcal{O}(j^3), \quad (\text{E.2})$$

with the longitudinal speed  $v_{\parallel}$  of this former diffusion mode and its modified diffusion coefficient  $\mathcal{D}_{\parallel}$ . The temperature at vanishing angular momentum  $a = 0$  takes the value  $T = r_+/\pi$ . Therefore, at  $a = 0$ , we expect

$$\mathcal{D}_{\parallel}(a = 0) = 2\pi T\mathcal{D} = \frac{1}{2}. \quad (\text{E.3})$$

Let us rewrite the dispersion relation in different frequency and momentum variables:

$$\omega = -i\mathcal{D}q^2, \quad (\text{E.4})$$

$$\Leftrightarrow 2\pi T\nu = -i\mathcal{D}(2\pi Tj)^2, \quad (\text{E.5})$$

$$\Leftrightarrow \nu = -i \underbrace{\mathcal{D}(2\pi T)}_{\mathcal{D}_{\parallel}} j^2. \quad (\text{E.6})$$

Now, let us write the dispersion relation in terms of the variables  $\omega$  and  $\mathcal{J}$ , which appear in the ansatz (60) for the metric fluctuations:

$$\omega = -iD\mathcal{J}^2, \quad (\text{E.7})$$

$$\Leftrightarrow \omega = -iD(\pi Tj)^2, \quad (\text{E.8})$$

$$\Leftrightarrow \omega = -iD(\pi T)^2 \left(\frac{q}{2\pi T}\right)^2 = -i \underbrace{\frac{D}{4}}_{\mathcal{D}} q^2, \quad (\text{E.9})$$

$a$	$v(a)$	$r_+ D(a)$
0	0	1
0.5	1	0.64952
0.9	1.8	0.08282

Table E.10: Example values expected for the diffusion coefficient  $D$  (multiplied by the horizon radius  $r_+$ ) and the velocity  $v$  in the large BH limit  $r_+ \rightarrow \infty$  (more precisely (112) and (113)) at distinct values of angular momentum  $a$ .

such that we expect  $D = 1/(\pi T) = 1/r_+$ .

Moving on to the case of  $a \neq 0$ , we write

$$\omega = v\mathcal{J} - iD\mathcal{J}^2, \quad (\text{E.10})$$

$$\Leftrightarrow \omega = -iD(\pi T j)^2, \quad (\text{E.11})$$

$$\Leftrightarrow \omega = -iD(\pi T)^2 \underbrace{\left(\frac{q}{2\pi T}\right)^2}_{\mathcal{D}} = -i \frac{D}{4} q^2, \quad (\text{E.12})$$

where  $D$  and  $v$  now depend on the angular momentum parameter  $a$ . In the large BH limit  $r_+ \rightarrow \infty$  (more precisely (112) and (113)), we expect  $D(a) = 2\frac{\mathcal{D}_{||}}{\pi T} = \frac{1}{r_+}(1 - a^2)^{3/2}$  and  $v = 2v_{||} = 2a$  [29], which are the values expected for a fluid boosted with boost parameter  $a$  [65, 66]. Thus, for example, the values given in Table E.10 are expected in this limit. This form (E.10) in terms of  $\omega$  and  $\mathcal{J}$  and allowing general exponents,  $\omega = v\mathcal{J}^\beta - iD\mathcal{J}^\alpha$ , was used to fit  $D$ ,  $v$ ,  $\alpha$  and  $\beta$  and the result of that fit is displayed in Fig. 11.

## Appendix F. Limits of the Wigner D function

An important consideration which has not yet been discussed is the relation of the Wigner d functions to Fourier transformations. To begin, we consider the decomposition of the Wigner- $D$  functions in terms of the Wigner- $d$  functions<sup>66</sup>.

$$D_{mk}^J(\theta, \phi, \psi) = e^{-i(k\phi + m\psi)} d_{mk}^J(\theta) \quad (\text{F.1})$$

The explicit form of the Wigner- $d$  functions can be written using the Wigner formula [158, 159],

$$d_{mk}^J(\theta) = \sum_n (-1)^n w_n^{Jmk} \cos(\theta/2)^{2J+k-m-2n} (-\sin(\theta/2))^{m-k-2n} \quad (\text{F.2})$$

where the coefficients  $w$  can be expressed in terms of a complicated fraction of factorials of its indices. Although this expression is complicated, an important observation is that one can reduce this formula for each value of the indices by repeated operation of the power reduction trigonometric identities to  $\cos(\nu\theta)$  ( $\sin(\nu\theta)$ ), such that,

$$d_{mk}^J(\theta) = \sum_{\nu=\nu_{min}}^{\nu_{max}=J} t_\nu^{Jmk} f(\nu\theta), \quad (\text{F.3})$$

where,

$$f = \begin{cases} \cos, & m - k \text{ even} \\ \sin, & m - k \text{ odd} \end{cases} \quad (\text{F.4})$$

<sup>66</sup>In this appendix we drop the notation  $(\mathcal{J}, \mathcal{K}, \mathcal{M})$  in favor of  $(J, m, k)$

Hence we see that expansion for the  $d$  function is in terms of  $\cos$  if  $J - k$  is even and  $\sin$  if  $J - k$  is odd. Recalling the large BH limit studied in [29, 32, 33] in Eq. (112) and Eq. (113) (repeated here for ease of presentation)

$$J = jr_+/\ell, \quad \omega = 2\nu r_+/\ell, \quad r \rightarrow \alpha r \quad r_+ \rightarrow \alpha r_+ \quad (\text{F.5})$$

around  $\alpha \rightarrow \infty$  along with the fact that sectors are distinguished by choices of  $m$  in terms of  $J$ , in the large BH limit  $J \approx m$ . In the actual calculation all  $k$  dependence of the field equations drops out and hence we are left with a freedom. Here we fix this freedom by assuming  $k$  even and  $J \in \mathbb{Z}$  and hence,

$$d_{mk}^J(\theta) = \sum_{\mu=0}^{\mu_{max}=J} t_{\mu}^{Jmk} \cos(\mu\theta) \quad (\text{F.6})$$

From orthogonality,

$$t_{\mu}^{Jmk} = \frac{1}{2\pi(1 + \delta_{\mu 0})} \int_0^{4\pi} d\theta d_{mk}^J(\theta) f(\mu\theta), \quad \delta_{\mu 0} = \begin{cases} 1 & \text{for } \mu = 0 \\ 0 & \text{else} \end{cases} \quad (\text{F.7})$$

one sees that  $t_{\mu}^{Jmk} = t_{-\mu}^{Jmk}$  and hence one can rewrite Eq. (F.6) as,

$$d_{mk}^J(\theta) = \frac{1}{2} \sum_{\mu=-J}^J t_{\mu}^{Jmk} e^{I\mu\theta} \quad (\text{F.8})$$

Therefore, the Wigner  $d$  functions can be written as Fourier sine and cosine series [159].

Now, let us diverge from [159] and investigate briefly what happens to this Fourier representation in the large BH limit, keeping mind that in this limit  $J \approx m$ . We have the following expression,

$$d_{\frac{j\alpha r_+}{\ell} k}^{\frac{j\alpha r_+}{\ell}}(\theta) = \frac{1}{2} \sum_{\mu=-\frac{j\alpha r_+}{\ell}}^{\frac{j\alpha r_+}{\ell}} \frac{\Delta\mu}{2\pi} \frac{2\pi}{\Delta\mu} t_{\mu}^{\frac{j\alpha r_+}{\ell} \frac{j\alpha r_+}{\ell} k} e^{I\mu\theta} \quad (\text{F.9})$$

where we have cleverly inserted a factor of 1 in the summand. If we formally extend the range of  $\theta$  to  $(-\infty, \infty)$  and define,

$$T_k(\mu) = \lim_{\Delta\mu \rightarrow 0} \lim_{\alpha \rightarrow \infty} \frac{2\pi}{\Delta\mu} t_{\mu}^{\frac{j\alpha r_+}{\ell} \frac{j\alpha r_+}{\ell} k} \quad (\text{F.10})$$

while using the definition from calculus that,

$$\lim_{\Delta\mu \rightarrow 0} \lim_{\alpha \rightarrow \infty} \sum_{\mu=-\frac{j\alpha r_+}{\ell}}^{\frac{j\alpha r_+}{\ell}} \frac{\Delta\mu}{2\pi} = \frac{1}{2\pi} \int_{-\infty}^{\infty} d\mu \quad (\text{F.11})$$

we find,

$$\lim_{\Delta\mu \rightarrow 0} \lim_{\alpha \rightarrow \infty} d_{\frac{j\alpha r_+}{\ell} k}^{\frac{j\alpha r_+}{\ell}}(\theta) = \frac{1}{4\pi} \int_{-\infty}^{\infty} d\mu T_k(\mu) e^{I\mu\theta} \quad (\text{F.12})$$

and hence the Wigner  $d$  function can be interpreted as a Fourier transformation. In these equations  $\theta$  should now be thought of as a coordinate along the real line  $\mathbb{R}$ .



## References

- [1] L. Adamczyk, et al., Global  $\Lambda$  hyperon polarization in nuclear collisions: evidence for the most vortical fluid, *Nature* 548 (2017) 62–65. [arXiv:1701.06657](#), [doi:10.1038/nature23004](#).
- [2] I. Karpenko, F. Becattini, Study of  $\Lambda$  polarization in relativistic nuclear collisions at  $\sqrt{s_{\text{NN}}} = 7.7 - 200$  GeV, *Eur. Phys. J. C* 77 (4) (2017) 213. [arXiv:1610.04717](#), [doi:10.1140/epjc/s10052-017-4765-1](#).
- [3] F. Becattini, I. Karpenko, Collective Longitudinal Polarization in Relativistic Heavy-Ion Collisions at Very High Energy, *Phys. Rev. Lett.* 120 (1) (2018) 012302. [arXiv:1707.07984](#), [doi:10.1103/PhysRevLett.120.012302](#).
- [4] W. Florkowski, B. Friman, A. Jaiswal, E. Speranza, Relativistic fluid dynamics with spin, *Phys. Rev. C* 97 (4) (2018) 041901. [arXiv:1705.00587](#), [doi:10.1103/PhysRevC.97.041901](#).
- [5] D. Montenegro, G. Torrieri, Linear response theory and effective action of relativistic hydrodynamics with spin, *Phys. Rev. D* 102 (3) (2020) 036007. [arXiv:2004.10195](#), [doi:10.1103/PhysRevD.102.036007](#).
- [6] S. Bhadury, W. Florkowski, A. Jaiswal, A. Kumar, R. Ryblewski, Dissipative Spin Dynamics in Relativistic Matter, *Phys. Rev. D* 103 (1) (2021) 014030. [arXiv:2008.10976](#), [doi:10.1103/PhysRevD.103.014030](#).
- [7] N. Weickgenannt, E. Speranza, X.-l. Sheng, Q. Wang, D. H. Rischke, Generating Spin Polarization from Vorticity through Nonlocal Collisions, *Phys. Rev. Lett.* 127 (5) (2021) 052301. [arXiv:2005.01506](#), [doi:10.1103/PhysRevLett.127.052301](#).
- [8] K. Fukushima, S. Pu, Spin hydrodynamics and symmetric energy-momentum tensors – A current induced by the spin vorticity –, *Phys. Lett. B* 817 (2021) 136346. [arXiv:2010.01608](#), [doi:10.1016/j.physletb.2021.136346](#).
- [9] S. Li, M. A. Stephanov, H.-U. Yee, Nondissipative Second-Order Transport, Spin, and Pseudogauge Transformations in Hydrodynamics, *Phys. Rev. Lett.* 127 (8) (2021) 082302. [arXiv:2011.12318](#), [doi:10.1103/PhysRevLett.127.082302](#).
- [10] F. Becattini, M. Buzzegoli, G. Inghirami, I. Karpenko, A. Palermo, Local Polarization and Isothermal Local Equilibrium in Relativistic Heavy Ion Collisions, *Phys. Rev. Lett.* 127 (27) (2021) 272302. [arXiv:2103.14621](#), [doi:10.1103/PhysRevLett.127.272302](#).
- [11] A. D. Gallegos, U. Gürsoy, A. Yarom, Hydrodynamics of spin currents, *SciPost Phys.* 11 (2021) 041. [arXiv:2101.04759](#), [doi:10.21468/SciPostPhys.11.2.041](#).
- [12] M. Hongo, X.-G. Huang, M. Kaminski, M. Stephanov, H.-U. Yee, Relativistic spin hydrodynamics with torsion and linear response theory for spin relaxation, *JHEP* 11 (2021) 150. [arXiv:2107.14231](#), [doi:10.1007/JHEP11\(2021\)150](#).
- [13] A. D. Gallegos, U. Gürsoy, A. Yarom, Hydrodynamics, spin currents and torsion, *JHEP* 05 (2023) 139. [arXiv:2203.05044](#), [doi:10.1007/JHEP05\(2023\)139](#).

- [14] D.-L. Wang, X.-Q. Xie, S. Fang, S. Pu, Analytic solutions of relativistic dissipative spin hydrodynamics with radial expansion in Gubser flow, *Phys. Rev. D* 105 (11) (2022) 114050. [arXiv:2112.15535](#), [doi:10.1103/PhysRevD.105.114050](#).
- [15] N. Weickgenannt, D. Wagner, E. Speranza, D. H. Rischke, Relativistic second-order dissipative spin hydrodynamics from the method of moments, *Phys. Rev. D* 106 (9) (2022) 096014. [arXiv:2203.04766](#), [doi:10.1103/PhysRevD.106.096014](#).
- [16] N. Weickgenannt, D. Wagner, E. Speranza, D. H. Rischke, Relativistic dissipative spin hydrodynamics from kinetic theory with a nonlocal collision term, *Phys. Rev. D* 106 (9) (2022) L091901. [arXiv:2208.01955](#), [doi:10.1103/PhysRevD.106.L091901](#).
- [17] B. Carter, Hamilton-Jacobi and Schrodinger separable solutions of Einstein's equations, *Commun. Math. Phys.* 10 (4) (1968) 280–310. [doi:10.1007/BF03399503](#).
- [18] R. C. Myers, M. Perry, Black Holes in Higher Dimensional Space-Times, *Annals Phys.* 172 (1986) 304. [doi:10.1016/0003-4916\(86\)90186-7](#).
- [19] S. W. Hawking, C. J. Hunter, M. Taylor, Rotation and the AdS / CFT correspondence, *Phys. Rev. D* 59 (1999) 064005. [arXiv:hep-th/9811056](#), [doi:10.1103/PhysRevD.59.064005](#).
- [20] S. W. Hawking, H. S. Reall, Charged and rotating AdS black holes and their CFT duals, *Phys. Rev. D* 61 (2000) 024014. [arXiv:hep-th/9908109](#), [doi:10.1103/PhysRevD.61.024014](#).
- [21] G. W. Gibbons, M. J. Perry, C. N. Pope, The First law of thermodynamics for Kerr-anti-de Sitter black holes, *Class. Quant. Grav.* 22 (2005) 1503–1526. [arXiv:hep-th/0408217](#), [doi:10.1088/0264-9381/22/9/002](#).
- [22] G. W. Gibbons, H. Lu, D. N. Page, C. N. Pope, Rotating black holes in higher dimensions with a cosmological constant, *Phys. Rev. Lett.* 93 (2004) 171102. [arXiv:hep-th/0409155](#), [doi:10.1103/PhysRevLett.93.171102](#).
- [23] K. Murata, J. Soda, A Note on separability of field equations in Myers-Perry spacetimes, *Class. Quant. Grav.* 25 (2008) 035006. [arXiv:0710.0221](#), [doi:10.1088/0264-9381/25/3/035006](#).
- [24] K. Murata, Instabilities of Kerr-AdS<sub>5</sub> × S<sup>5</sup> Spacetime, *Prog. Theor. Phys.* 121 (2009) 1099–1124. [arXiv:0812.0718](#), [doi:10.1143/PTP.121.1099](#).
- [25] K. Murata, J. Soda, Stability of Five-dimensional Myers-Perry Black Holes with Equal Angular Momenta, *Prog. Theor. Phys.* 120 (2008) 561–579. [arXiv:0803.1371](#), [doi:10.1143/PTP.120.561](#).
- [26] V. Cardoso, O. J. C. Dias, G. S. Hartnett, L. Lehner, J. E. Santos, Holographic thermalization, quasinormal modes and superradiance in Kerr-AdS, *JHEP* 04 (2014) 183. [arXiv:1312.5323](#), [doi:10.1007/JHEP04\(2014\)183](#).
- [27] R. Gregory, D. Kubiznak, D. Wills, Rotating black hole hair, *JHEP* 06 (2013) 023. [arXiv:1303.0519](#), [doi:10.1007/JHEP06\(2013\)023](#).

- [28] T. Ishii, K. Murata, Photonic black resonators and photon stars in AdS<sub>5</sub>, *Class. Quant. Grav.* 37 (7) (2020) 075009. [arXiv:1910.03234](#), [doi:10.1088/1361-6382/ab7418](#).
- [29] M. Garbiso, M. Kaminski, Hydrodynamics of simply spinning black holes & hydrodynamics for spinning quantum fluids, *JHEP* 12 (2020) 112. [arXiv:2007.04345](#), [doi:10.1007/JHEP12\(2020\)112](#).
- [30] C. Cartwright, B. Harms, M. Kaminski, Topological or rotational non-Abelian gauge fields from Einstein-Skyrme holography, *JHEP* 03 (2021) 229. [arXiv:2010.03578](#), [doi:10.1007/JHEP03\(2021\)229](#).
- [31] T. Ishii, K. Murata, J. E. Santos, B. Way, Multioscillating black holes, *JHEP* 05 (2021) 011. [arXiv:2101.06325](#), [doi:10.1007/JHEP05\(2021\)011](#).
- [32] C. Cartwright, M. G. Amano, M. Kaminski, J. Noronha, E. Speranza, Convergence of hydrodynamics in a rotating strongly coupled plasma, *Phys. Rev. D* 108 (4) (2023) 046014. [arXiv:2112.10781](#), [doi:10.1103/PhysRevD.108.046014](#).
- [33] M. A. G. Amano, M. Blake, C. Cartwright, M. Kaminski, A. P. Thompson, Chaos and pole-skipping in a simply spinning plasma, *JHEP* 02 (2023) 253. [arXiv:2211.00016](#), [doi:10.1007/JHEP02\(2023\)253](#).
- [34] J. Erdmenger, M. Haack, M. Kaminski, A. Yarom, Fluid dynamics of R-charged black holes, *JHEP* 01 (2009) 055. [arXiv:0809.2488](#), [doi:10.1088/1126-6708/2009/01/055](#).
- [35] M. Ammon, S. Griener, J. Hernandez, M. Kaminski, R. Koirala, J. Leiber, J. Wu, Chiral hydrodynamics in strong external magnetic fields, *JHEP* 04 (2021) 078. [arXiv:2012.09183](#), [doi:10.1007/JHEP04\(2021\)078](#).
- [36] H. Bantilan, T. Ishii, P. Romatschke, Holographic heavy-ion collisions: Analytic solutions with longitudinal flow, elliptic flow and vorticity, *Phys. Lett. B* 785 (2018) 201–206. [arXiv:1803.10774](#), [doi:10.1016/j.physletb.2018.08.038](#).
- [37] G. W. Gibbons, H. Lu, D. N. Page, C. N. Pope, The General Kerr-de Sitter metrics in all dimensions, *J. Geom. Phys.* 53 (2005) 49–73. [arXiv:hep-th/0404008](#), [doi:10.1016/j.geomphys.2004.05.001](#).
- [38] P. K. Kovtun, A. O. Starinets, Quasinormal modes and holography, *Phys. Rev. D* 72 (2005) 086009. [arXiv:hep-th/0506184](#), [doi:10.1103/PhysRevD.72.086009](#).
- [39] S. Grozdanov, P. K. Kovtun, A. O. Starinets, P. Tadić, The complex life of hydrodynamic modes, *JHEP* 11 (2019) 097. [arXiv:1904.12862](#), [doi:10.1007/JHEP11\(2019\)097](#).
- [40] M. P. Heller, A. Serantes, M. Spaliński, V. Svensson, B. Withers, Convergence of hydrodynamic modes: insights from kinetic theory and holography, *SciPost Phys.* 10 (6) (2021) 123. [arXiv:2012.15393](#), [doi:10.21468/SciPostPhys.10.6.123](#).
- [41] M. P. Heller, A. Serantes, M. Spaliński, V. Svensson, B. Withers, Hydrodynamic gradient expansion in linear response theory, *Phys. Rev. D* 104 (6) (2021) 066002. [arXiv:2007.05524](#), [doi:10.1103/PhysRevD.104.066002](#).

- [42] S. Grozdanov, K. Schalm, V. Scopelliti, Black hole scrambling from hydrodynamics, *Phys. Rev. Lett.* 120 (23) (2018) 231601. [arXiv:1710.00921](#), [doi:10.1103/PhysRevLett.120.231601](#).
- [43] S. H. Shenker, D. Stanford, Black holes and the butterfly effect, *JHEP* 03 (2014) 067. [arXiv:1306.0622](#), [doi:10.1007/JHEP03\(2014\)067](#).
- [44] S. H. Shenker, D. Stanford, Stringy effects in scrambling, *JHEP* 05 (2015) 132. [arXiv:1412.6087](#), [doi:10.1007/JHEP05\(2015\)132](#).
- [45] P. C. Aichelburg, R. U. Sexl, On the Gravitational field of a massless particle, *Gen. Rel. Grav.* 2 (1971) 303–312. [doi:10.1007/BF00758149](#).
- [46] T. Dray, G. 't Hooft, The Gravitational Shock Wave of a Massless Particle, *Nucl. Phys. B* 253 (1985) 173–188. [doi:10.1016/0550-3213\(85\)90525-5](#).
- [47] K. Sfetsos, On gravitational shock waves in curved space-times, *Nucl. Phys. B* 436 (1995) 721–745. [arXiv:hep-th/9408169](#), [doi:10.1016/0550-3213\(94\)00573-W](#).
- [48] M. Blake, H. Lee, H. Liu, A quantum hydrodynamical description for scrambling and many-body chaos, *JHEP* 10 (2018) 127. [arXiv:1801.00010](#), [doi:10.1007/JHEP10\(2018\)127](#).
- [49] M. Blake, R. A. Davison, S. Grozdanov, H. Liu, Many-body chaos and energy dynamics in holography, *JHEP* 10 (2018) 035. [arXiv:1809.01169](#), [doi:10.1007/JHEP10\(2018\)035](#).
- [50] S. Bhattacharyya, V. E. Hubeny, S. Minwalla, M. Rangamani, Nonlinear Fluid Dynamics from Gravity, *JHEP* 02 (2008) 045. [arXiv:0712.2456](#), [doi:10.1088/1126-6708/2008/02/045](#).
- [51] A. N. Aliev, O. Delice, Superradiant Instability of Five-Dimensional Rotating Charged AdS Black Holes, *Phys. Rev. D* 79 (2009) 024013. [arXiv:0808.0280](#), [doi:10.1103/PhysRevD.79.024013](#).
- [52] R. Monteiro, M. J. Perry, J. E. Santos, Thermodynamic instability of rotating black holes, *Phys. Rev. D* 80 (2009) 024041. [arXiv:0903.3256](#), [doi:10.1103/PhysRevD.80.024041](#).
- [53] B. I. Abelev, et al., Global polarization measurement in Au+Au collisions, *Phys. Rev. C* 76 (2007) 024915, [Erratum: *Phys.Rev.C* 95, 039906 (2017)]. [arXiv:0705.1691](#), [doi:10.1103/PhysRevC.76.024915](#).
- [54] Z.-T. Liang, X.-N. Wang, Globally polarized quark-gluon plasma in non-central A+A collisions, *Phys. Rev. Lett.* 94 (2005) 102301, [Erratum: *Phys.Rev.Lett.* 96, 039901 (2006)]. [arXiv:nucl-th/0410079](#), [doi:10.1103/PhysRevLett.94.102301](#).
- [55] F. Becattini, F. Piccinini, J. Rizzo, Angular momentum conservation in heavy ion collisions at very high energy, *Phys. Rev. C* 77 (2008) 024906. [arXiv:0711.1253](#), [doi:10.1103/PhysRevC.77.024906](#).

- [56] F. Becattini, L. Csernai, D. J. Wang,  $\Lambda$  polarization in peripheral heavy ion collisions, *Phys. Rev. C* 88 (3) (2013) 034905, [Erratum: *Phys.Rev.C* 93, 069901 (2016)]. [arXiv:1304.4427](#), [doi:10.1103/PhysRevC.88.034905](#).
- [57] D. E. Kharzeev, J. Liao, S. A. Voloshin, G. Wang, Chiral magnetic and vortical effects in high-energy nuclear collisions—A status report, *Prog. Part. Nucl. Phys.* 88 (2016) 1–28. [arXiv:1511.04050](#), [doi:10.1016/j.pnpnp.2016.01.001](#).
- [58] L.-G. Pang, H. Petersen, Q. Wang, X.-N. Wang, Vortical Fluid and  $\Lambda$  Spin Correlations in High-Energy Heavy-Ion Collisions, *Phys. Rev. Lett.* 117 (19) (2016) 192301. [arXiv:1605.04024](#), [doi:10.1103/PhysRevLett.117.192301](#).
- [59] J. Adam, et al., Global polarization of  $\Lambda$  hyperons in Au+Au collisions at  $\sqrt{s_{NN}} = 200$  GeV, *Phys. Rev. C* 98 (2018) 014910. [arXiv:1805.04400](#), [doi:10.1103/PhysRevC.98.014910](#).
- [60] S. Acharya, et al., Global polarization of  $\Lambda\bar{\Lambda}$  hyperons in Pb-Pb collisions at  $\sqrt{s_{NN}} = 2.76$  and 5.02 TeV, *Phys. Rev. C* 101 (4) (2020) 044611, [Erratum: *Phys.Rev.C* 105, 029902 (2022)]. [arXiv:1909.01281](#), [doi:10.1103/PhysRevC.101.044611](#).
- [61] J. Adam, et al., Polarization of  $\Lambda$  ( $\bar{\Lambda}$ ) hyperons along the beam direction in Au+Au collisions at  $\sqrt{s_{NN}} = 200$  GeV, *Phys. Rev. Lett.* 123 (13) (2019) 132301. [arXiv:1905.11917](#), [doi:10.1103/PhysRevLett.123.132301](#).
- [62] S. Acharya, et al., Polarization of  $\Lambda$  and  $\bar{\Lambda}$  Hyperons along the Beam Direction in Pb-Pb Collisions at  $\sqrt{s_{NN}}=5.02$  TeV, *Phys. Rev. Lett.* 128 (17) (2022) 172005. [arXiv:2107.11183](#), [doi:10.1103/PhysRevLett.128.172005](#).
- [63] M. Hongo, X.-G. Huang, M. Kaminski, M. Stephanov, H.-U. Yee, Spin relaxation rate for heavy quarks in weakly coupled QCD plasma, *JHEP* 08 (2022) 263. [arXiv:2201.12390](#), [doi:10.1007/JHEP08\(2022\)263](#).
- [64] P. Romatschke, U. Romatschke, *Relativistic Fluid Dynamics In and Out of Equilibrium*, Cambridge Monographs on Mathematical Physics, Cambridge University Press, 2019. [arXiv:1712.05815](#), [doi:10.1017/9781108651998](#).
- [65] P. Kovtun, First-order relativistic hydrodynamics is stable, *JHEP* 10 (2019) 034. [arXiv:1907.08191](#), [doi:10.1007/JHEP10\(2019\)034](#).
- [66] R. E. Houtt, P. Kovtun, Stable and causal relativistic Navier-Stokes equations, *JHEP* 06 (2020) 067. [arXiv:2004.04102](#), [doi:10.1007/JHEP06\(2020\)067](#).
- [67] S. Bhattacharyya, S. Lahiri, R. Loganayagam, S. Minwalla, Large rotating AdS black holes from fluid mechanics, *JHEP* 09 (2008) 054. [arXiv:0708.1770](#), [doi:10.1088/1126-6708/2008/09/054](#).
- [68] E. Witten, (2+1)-Dimensional Gravity as an Exactly Soluble System, *Nucl. Phys. B* 311 (1988) 46. [doi:10.1016/0550-3213\(88\)90143-5](#).
- [69] S. Carlip, Lectures on (2+1) dimensional gravity, *J. Korean Phys. Soc.* 28 (1995) S447–S467. [arXiv:gr-qc/9503024](#).

- [70] M. Banados, C. Teitelboim, J. Zanelli, The Black hole in three-dimensional space-time, *Phys. Rev. Lett.* 69 (1992) 1849–1851. [arXiv:hep-th/9204099](#), [doi:10.1103/PhysRevLett.69.1849](#).
- [71] S. Carlip, The (2+1)-Dimensional black hole, *Class. Quant. Grav.* 12 (1995) 2853–2880. [arXiv:gr-qc/9506079](#), [doi:10.1088/0264-9381/12/12/005](#).
- [72] M. Kamata, T. Koikawa, The Electrically charged BTZ black hole with self (anti-self) dual Maxwell field, *Phys. Lett. B* 353 (1995) 196–200. [arXiv:hep-th/9505037](#), [doi:10.1016/0370-2693\(95\)00583-7](#).
- [73] S. Fernando, F. Mansouri, Rotating charged solutions to einstein maxwell chern-simons theory in (2+1)-dimensions (5 1997). [arXiv:gr-qc/9705016](#).
- [74] M. Cataldo, P. Salgado, Three dimensional extreme black hole with self (anti-self) dual Maxwell field, *Phys. Lett. B* 448 (1999) 20–25. [doi:10.1016/S0370-2693\(99\)00035-0](#).
- [75] N. V. Mitskievich, A. A. Garcia, Anti-de Sitter type (2+1)-space-time of a charged rotating mass (1 2001). [arXiv:gr-qc/0101029](#).
- [76] G. Clement, Classical solutions in three-dimensional Einstein-Maxwell cosmological gravity, *Class. Quant. Grav.* 10 (1993) L49–L54. [doi:10.1088/0264-9381/10/5/002](#).
- [77] C. Martinez, C. Teitelboim, J. Zanelli, Charged rotating black hole in three space-time dimensions, *Phys. Rev. D* 61 (2000) 104013. [arXiv:hep-th/9912259](#), [doi:10.1103/PhysRevD.61.104013](#).
- [78] J. D. Brown, M. Henneaux, Central Charges in the Canonical Realization of Asymptotic Symmetries: An Example from Three-Dimensional Gravity, *Commun. Math. Phys.* 104 (1986) 207–226. [doi:10.1007/BF01211590](#).
- [79] A. Strominger, Black hole entropy from near horizon microstates, *JHEP* 02 (1998) 009. [arXiv:hep-th/9712251](#), [doi:10.1088/1126-6708/1998/02/009](#).
- [80] E. Keski-Vakkuri, Bulk and boundary dynamics in BTZ black holes, *Phys. Rev. D* 59 (1999) 104001. [arXiv:hep-th/9808037](#), [doi:10.1103/PhysRevD.59.104001](#).
- [81] V. Balasubramanian, P. Kraus, A. E. Lawrence, S. P. Trivedi, Holographic probes of anti-de Sitter space-times, *Phys. Rev. D* 59 (1999) 104021. [arXiv:hep-th/9808017](#), [doi:10.1103/PhysRevD.59.104021](#).
- [82] V. Balasubramanian, S. F. Ross, Holographic particle detection, *Phys. Rev. D* 61 (2000) 044007. [arXiv:hep-th/9906226](#), [doi:10.1103/PhysRevD.61.044007](#).
- [83] D. A. Roberts, D. Stanford, L. Susskind, Localized shocks, *JHEP* 03 (2015) 051. [arXiv:1409.8180](#), [doi:10.1007/JHEP03\(2015\)051](#).
- [84] V. Jahnke, K.-Y. Kim, J. Yoon, On the chaos bound in rotating black holes, *JHEP* 05 (2019) 037. [arXiv:1903.09086](#), [doi:10.1007/JHEP05\(2019\)037](#).

- [85] B. Craps, S. Khetrpal, C. Rabideau, Chaos in CFT dual to rotating BTZ, JHEP 11 (2021) 105. [arXiv:2107.13874](#), [doi:10.1007/JHEP11\(2021\)105](#).
- [86] S. A. Teukolsky, The Kerr Metric, *Class. Quant. Grav.* 32 (12) (2015) 124006. [arXiv:1410.2130](#), [doi:10.1088/0264-9381/32/12/124006](#).
- [87] M. M. Caldarelli, R. Emparan, M. J. Rodriguez, Black Rings in (Anti)-deSitter space, JHEP 11 (2008) 011. [arXiv:0806.1954](#), [doi:10.1088/1126-6708/2008/11/011](#).
- [88] R. Emparan, H. S. Reall, A Rotating black ring solution in five-dimensions, *Phys. Rev. Lett.* 88 (2002) 101101. [arXiv:hep-th/0110260](#), [doi:10.1103/PhysRevLett.88.101101](#).
- [89] R. Emparan, H. S. Reall, Black Holes in Higher Dimensions, *Living Rev. Rel.* 11 (2008) 6. [arXiv:0801.3471](#), [doi:10.12942/lrr-2008-6](#).
- [90] R. P. Kerr, Gravitational field of a spinning mass as an example of algebraically special metrics, *Phys. Rev. Lett.* 11 (1963) 237–238. [doi:10.1103/PhysRevLett.11.237](#).  
URL <https://link.aps.org/doi/10.1103/PhysRevLett.11.237>
- [91] J. E. Avron, R. Seiler, P. G. Zograf, Viscosity of quantum Hall fluids, *Phys. Rev. Lett.* 75 (1995) 697–700. [arXiv:cond-mat/9502011](#), [doi:10.1103/PhysRevLett.75.697](#).
- [92] K. Jensen, M. Kaminski, P. Kovtun, R. Meyer, A. Ritz, A. Yarom, Parity-Violating Hydrodynamics in 2+1 Dimensions, JHEP 05 (2012) 102. [arXiv:1112.4498](#), [doi:10.1007/JHEP05\(2012\)102](#).
- [93] K. Jensen, M. Kaminski, P. Kovtun, R. Meyer, A. Ritz, A. Yarom, Towards hydrodynamics without an entropy current, *Phys. Rev. Lett.* 109 (2012) 101601. [arXiv:1203.3556](#), [doi:10.1103/PhysRevLett.109.101601](#).
- [94] B. McNnes, Angular Momentum in QGP Holography, *Nucl. Phys. B* 887 (2014) 246–264. [arXiv:1403.3258](#), [doi:10.1016/j.nuclphysb.2014.08.011](#).
- [95] B. McNnes, A rotation/magnetism analogy for the quark–gluon plasma, *Nucl. Phys. B* 911 (2016) 173–190. [arXiv:1604.03669](#), [doi:10.1016/j.nuclphysb.2016.08.001](#).
- [96] B. McNnes, Jet Quenching in The Most Vortical Fluid: A Holographic Approach (10 2017). [arXiv:1710.07442](#).
- [97] X. Chen, L. Zhang, D. Li, D. Hou, M. Huang, Gluodynamics and deconfinement phase transition under rotation from holography, JHEP 07 (2021) 132. [arXiv:2010.14478](#), [doi:10.1007/JHEP07\(2021\)132](#).
- [98] I. Papadimitriou, K. Skenderis, Thermodynamics of asymptotically locally AdS spacetimes, JHEP 08 (2005) 004. [arXiv:hep-th/0505190](#), [doi:10.1088/1126-6708/2005/08/004](#).

- [99] H. Elvang, P. Figueras, Black Saturn, JHEP 05 (2007) 050. [arXiv:hep-th/0701035](#), [doi:10.1088/1126-6708/2007/05/050](#).
- [100] R. M. Wald, General Relativity, Chicago Univ. Pr., Chicago, USA, 1984. [doi:10.7208/chicago/9780226870373.001.0001](#).
- [101] H. K. Kunduri, J. Lucietti, H. S. Reall, Gravitational perturbations of higher dimensional rotating black holes: Tensor perturbations, Phys. Rev. D 74 (2006) 084021. [arXiv:hep-th/0606076](#), [doi:10.1103/PhysRevD.74.084021](#).
- [102] M. Nakahara, Geometry, Topology and Physics, 2nd Edition, CRC Press, 2003.
- [103] C. Chevalley, Theory of Lie Groups (PMS-8), Princeton University Press, 1946. URL <http://www.jstor.org/stable/j.ctt1bpm9z7>
- [104] M. Fecko, Differential Geometry and Lie Groups for Physicists, Cambridge University Press, 2006. [doi:10.1017/CB09780511755590](#).
- [105] D. A. Varshalovich, A. N. Moskalev, V. K. Khersonskii, Quantum theory of angular momentum, World Scientific Pub., 1988.
- [106] J. J. Sakurai, J. Napolitano, Modern Quantum Mechanics, 2nd Edition, Cambridge University Press, 2017. [doi:10.1017/9781108499996](#).
- [107] S. de Haro, S. N. Solodukhin, K. Skenderis, Holographic reconstruction of space-time and renormalization in the AdS / CFT correspondence, Commun. Math. Phys. 217 (2001) 595–622. [arXiv:hep-th/0002230](#), [doi:10.1007/s002200100381](#).
- [108] A. M. Awad, C. V. Johnson, Holographic stress tensors for Kerr - AdS black holes, Phys. Rev. D 61 (2000) 084025. [arXiv:hep-th/9910040](#), [doi:10.1103/PhysRevD.61.084025](#).
- [109] A. M. Awad, C. V. Johnson, Higher dimensional Kerr - AdS black holes and the AdS / CFT correspondence, Phys. Rev. D 63 (2001) 124023. [arXiv:hep-th/0008211](#), [doi:10.1103/PhysRevD.63.124023](#).
- [110] N. D. Birrell, P. C. W. Davies, Quantum Fields in Curved Space, Cambridge Monographs on Mathematical Physics, Cambridge Univ. Press, Cambridge, UK, 1984. [doi:10.1017/CB09780511622632](#).
- [111] V. Balasubramanian, P. Kraus, A Stress tensor for Anti-de Sitter gravity, Commun. Math. Phys. 208 (1999) 413–428. [arXiv:hep-th/9902121](#), [doi:10.1007/s002200050764](#).
- [112] R. Kallosh, A. Rajaraman, Vacua of M theory and string theory, Phys. Rev. D 58 (1998) 125003. [arXiv:hep-th/9805041](#), [doi:10.1103/PhysRevD.58.125003](#).
- [113] A. Ashtekar, A. Magnon, Asymptotically anti-de Sitter space-times, Class. Quant. Grav. 1 (1984) L39–L44. [doi:10.1088/0264-9381/1/4/002](#).
- [114] A. Ashtekar, S. Das, Asymptotically Anti-de Sitter space-times: Conserved quantities, Class. Quant. Grav. 17 (2000) L17–L30. [arXiv:hep-th/9911230](#), [doi:10.1088/0264-9381/17/2/101](#).



- [115] I. Papadimitriou, K. Skenderis, AdS / CFT correspondence and geometry, IRMA Lect. Math. Theor. Phys. 8 (2005) 73–101. [arXiv:hep-th/0404176](#), [doi:10.4171/013-1/4](#).
- [116] E. Berti, V. Cardoso, A. O. Starinets, Quasinormal modes of black holes and black branes, Class. Quant. Grav. 26 (2009) 163001. [arXiv:0905.2975](#), [doi:10.1088/0264-9381/26/16/163001](#).
- [117] S. Hawking, D. N. Page, Thermodynamics of Black Holes in anti-De Sitter Space, Commun. Math. Phys. 87 (1983) 577. [doi:10.1007/BF01208266](#).
- [118] G. Festuccia, H. Liu, A Bohr-Sommerfeld quantization formula for quasinormal frequencies of AdS black holes, Adv. Sci. Lett. 2 (2009) 221–235. [arXiv:0811.1033](#), [doi:10.1166/asl.2009.1029](#).
- [119] J. F. Fuini, C. F. Uhlemann, L. G. Yaffe, Damping of hard excitations in strongly coupled  $\mathcal{N} = 4$  plasma, JHEP 12 (2016) 042. [arXiv:1610.03491](#), [doi:10.1007/JHEP12\(2016\)042](#).
- [120] G. Policastro, D. T. Son, A. O. Starinets, From AdS / CFT correspondence to hydrodynamics, JHEP 09 (2002) 043. [arXiv:hep-th/0205052](#), [doi:10.1088/1126-6708/2002/09/043](#).
- [121] M. Natsuume, M. Ohta, The Shear viscosity of holographic superfluids, Prog. Theor. Phys. 124 (2010) 931–951. [arXiv:1008.4142](#), [doi:10.1143/PTP.124.931](#).
- [122] J. Erdmenger, P. Kerner, H. Zeller, Non-universal shear viscosity from Einstein gravity, Phys. Lett. B 699 (2011) 301–304. [arXiv:1011.5912](#), [doi:10.1016/j.physletb.2011.04.009](#).
- [123] A. Rebhan, D. Steineder, Violation of the Holographic Viscosity Bound in a Strongly Coupled Anisotropic Plasma, Phys. Rev. Lett. 108 (2012) 021601. [arXiv:1110.6825](#), [doi:10.1103/PhysRevLett.108.021601](#).
- [124] P. Kovtun, D. T. Son, A. O. Starinets, Viscosity in strongly interacting quantum field theories from black hole physics, Phys. Rev. Lett. 94 (2005) 111601. [arXiv:hep-th/0405231](#), [doi:10.1103/PhysRevLett.94.111601](#).
- [125] W. Florkowski, R. Ryblewski, Highly-anisotropic and strongly-dissipative hydrodynamics for early stages of relativistic heavy-ion collisions, Phys. Rev. C 83 (2011) 034907. [arXiv:1007.0130](#), [doi:10.1103/PhysRevC.83.034907](#).
- [126] M. Martinez, M. Strickland, Dissipative Dynamics of Highly Anisotropic Systems, Nucl. Phys. A 848 (2010) 183–197. [arXiv:1007.0889](#), [doi:10.1016/j.nuclphysa.2010.08.011](#).
- [127] W. Florkowski, M. Martinez, R. Ryblewski, M. Strickland, Anisotropic hydrodynamics - basic concepts, PoS ConfinementX (2012) 221. [arXiv:1301.7539](#), [doi:10.22323/1.171.0221](#).
- [128] S. Janiszewski, M. Kaminski, Quasinormal modes of magnetic and electric black branes versus far from equilibrium anisotropic fluids, Phys. Rev. D 93 (2) (2016) 025006. [arXiv:1508.06993](#), [doi:10.1103/PhysRevD.93.025006](#).

- [129] C. Bender, S. Orszag, *Advanced Mathematical Methods for Scientists and Engineers I: Asymptotic Methods and Perturbation Theory*, *Advanced Mathematical Methods for Scientists and Engineers*, Springer, 1999.
- [130] M. Edalati, J. I. Jottar, R. G. Leigh, Transport Coefficients at Zero Temperature from Extremal Black Holes, *JHEP* 01 (2010) 018. [arXiv:0910.0645](#), [doi:10.1007/JHEP01\(2010\)018](#).
- [131] M. Edalati, J. I. Jottar, R. G. Leigh, Shear Modes, Criticality and Extremal Black Holes, *JHEP* 04 (2010) 075. [arXiv:1001.0779](#), [doi:10.1007/JHEP04\(2010\)075](#).
- [132] N. Abbasi, Long-time tails in the SYK chain from the effective field theory with a large number of derivatives, *JHEP* 04 (2022) 181. [arXiv:2112.12751](#), [doi:10.1007/JHEP04\(2022\)181](#).
- [133] N. Abbasi, M. Kaminski, O. Tavakol, Theory of Nonlinear Diffusion with a Physical Gapped Mode, *Phys. Rev. Lett.* 132 (13) (2024) 131602. [arXiv:2212.11499](#), [doi:10.1103/PhysRevLett.132.131602](#).
- [134] T. Ishii, Superradiant instability and black resonators in AdS, *SciPost Phys. Proc.* 4 (2021) 008. [doi:10.21468/SciPostPhysProc.4.008](#).
- [135] T. Ishii, K. Murata, Black resonators and geons in AdS<sub>5</sub>, *Class. Quant. Grav.* 36 (12) (2019) 125011. [arXiv:1810.11089](#), [doi:10.1088/1361-6382/ab1d76](#).
- [136] O. J. C. Dias, J. E. Santos, AdS nonlinear instability: breaking spherical and axial symmetries, *Class. Quant. Grav.* 35 (18) (2018) 185006. [arXiv:1705.03065](#), [doi:10.1088/1361-6382/aad514](#).
- [137] O. J. C. Dias, J. E. Santos, B. Way, Black holes with a single Killing vector field: black resonators, *JHEP* 12 (2015) 171. [arXiv:1505.04793](#), [doi:10.1007/JHEP12\(2015\)171](#).
- [138] R. J. Walker, *Algebraic curves*, Vol. 58, Springer, 1950.
- [139] C. T. C. Wall, *Singular Points of Plane Curves*, London Mathematical Society Student Texts, Cambridge University Press, 2004. [doi:10.1017/CB09780511617560](#).
- [140] Y. Liu, A. Raju, Quantum chaos in topologically massive gravity, *JHEP* 12 (2020) 027. [arXiv:2005.08508](#), [doi:10.1007/JHEP12\(2020\)027](#).
- [141] M. Mezei, G. Sárosi, Chaos in the butterfly cone, *JHEP* 01 (2020) 186. [arXiv:1908.03574](#), [doi:10.1007/JHEP01\(2020\)186](#).
- [142] M. Blake, R. A. Davison, Chaos and pole-skipping in rotating black holes, *JHEP* 01 (2022) 013. [arXiv:2111.11093](#), [doi:10.1007/JHEP01\(2022\)013](#).
- [143] D. N. Kabat, M. Ortiz, Eikonal quantum gravity and Planckian scattering, *Nucl. Phys. B* 388 (1992) 570–592. [arXiv:hep-th/9203082](#), [doi:10.1016/0550-3213\(92\)90627-N](#).
- [144] J. V. Rocha, R. Santarelli, T. Delsate, Collapsing rotating shells in myers-perry-ads<sub>5</sub> spacetime: A perturbative approach, *Phys. Rev. D* 89 (10) (2014) 104006. [arXiv:1402.4161](#), [doi:10.1103/PhysRevD.89.104006](#).

- [145] J. Maldacena, S. H. Shenker, D. Stanford, A bound on chaos, *JHEP* 08 (2016) 106. [arXiv:1503.01409](#), [doi:10.1007/JHEP08\(2016\)106](#).
- [146] N. Abbasi, S. Tahery, Complexified quasinormal modes and the pole-skipping in a holographic system at finite chemical potential, *JHEP* 10 (2020) 076. [arXiv:2007.10024](#), [doi:10.1007/JHEP10\(2020\)076](#).
- [147] M. Alqahtani, M. Nopoush, M. Strickland, Relativistic anisotropic hydrodynamics, *Prog. Part. Nucl. Phys.* 101 (2018) 204–248. [arXiv:1712.03282](#), [doi:10.1016/j.ppnp.2018.05.004](#).
- [148] C. Cartwright, An example of the convergence of hydrodynamics in strong external fields (3 2024). [arXiv:2403.12638](#).
- [149] S. Grozdanov, P. K. Kovtun, A. O. Starinets, P. Tadić, Convergence of the Gradient Expansion in Hydrodynamics, *Phys. Rev. Lett.* 122 (25) (2019) 251601. [arXiv:1904.01018](#), [doi:10.1103/PhysRevLett.122.251601](#).
- [150] B. P. Abbott, et al., Observation of Gravitational Waves from a Binary Black Hole Merger, *Phys. Rev. Lett.* 116 (6) (2016) 061102. [arXiv:1602.03837](#), [doi:10.1103/PhysRevLett.116.061102](#).
- [151] M. Bailes, et al., Gravitational-wave physics and astronomy in the 2020s and 2030s, *Nature Rev. Phys.* 3 (5) (2021) 344–366. [doi:10.1038/s42254-021-00303-8](#).
- [152] L. W. Molenkamp, M. J. M. de Jong, Electron-electron-scattering-induced size effects in a two-dimensional wire, *Phys. Rev. B* 49 (1994) 5038–5041. [doi:10.1103/PhysRevB.49.5038](#).  
URL <https://link.aps.org/doi/10.1103/PhysRevB.49.5038>
- [153] P. J. W. Moll, P. Kushwaha, N. Nandi, B. Schmidt, A. P. Mackenzie, Evidence for hydrodynamic electron flow in PdCoO<sub>2</sub>, *Science* 351 (6277) (2016) 1061–1064. [arXiv:https://www.science.org/doi/pdf/10.1126/science.aac8385](#), [doi:10.1126/science.aac8385](#).  
URL <https://www.science.org/doi/abs/10.1126/science.aac8385>
- [154] I. Bloch, J. Dalibard, W. Zwerger, Many-body physics with ultracold gases, *Rev. Mod. Phys.* 80 (2008) 885–964. [doi:10.1103/RevModPhys.80.885](#).  
URL <https://link.aps.org/doi/10.1103/RevModPhys.80.885>
- [155] J. Sinova, S. O. Valenzuela, J. Wunderlich, C. H. Back, T. Jungwirth, Spin hall effects, *Rev. Mod. Phys.* 87 (2015) 1213–1260. [doi:10.1103/RevModPhys.87.1213](#).  
URL <https://link.aps.org/doi/10.1103/RevModPhys.87.1213>
- [156] M. Strickland, Anisotropic Hydrodynamics: Three lectures, *Acta Phys. Polon. B* 45 (12) (2014) 2355–2394. [arXiv:1410.5786](#), [doi:10.5506/APhysPolB.45.2355](#).
- [157] S. Waeber, L. G. Yaffe, Colliding localized, lumpy holographic shocks with a granular nuclear structure, *JHEP* 03 (2023) 208. [arXiv:2211.09190](#), [doi:10.1007/JHEP03\(2023\)208](#).
- [158] J. Schwinger, On angular momentum (1 1952). [doi:10.2172/4389568](#).  
URL <https://www.osti.gov/biblio/4389568>

- [159] N. Tajima, Analytical formula for numerical evaluations of the wigner rotation matrices at high spins, Phys. Rev. C 91 (1) (2015) 014320. [arXiv:1501.06347](#), [doi:10.1103/PhysRevC.91.014320](#).